**Università degli Studi di Firenze**

Facoltà di Scienze Matematiche Fisiche e Naturali
Dottorato di Ricerca in Fisica, **XVIII** Ciclo
Settore Disciplinare: Fisica Nucleare e Subnucleare (FIS04)

PhD Thesis

# Data analysis of cosmic rays at ground level with the PAMELA experiment

**Massimo Bongi**

Advisor:
Dr.
**Paolo Papini**

PhD Coordinator:
Prof.
**Alessandro Cuccoli**

Firenze, 31 Dicembre 2005

# Introduction

PAMELA (*Payload for Antimatter/Matter Exploration and Light-nuclei Astrophysics*) is a satellite-borne experiment which has been designed to study charged cosmic rays, in particular having been optimized to reveal the antiparticle component of the cosmic radiation.

As we know today, elementary particles such as free protons, electrons and atomic nuclei sweep continuously through the space around the Earth, coming from the Sun and from exploding supernovae, or from other even more exotic sources within our galaxy. Such kind of radiation has been discovered at the beginning of the $20^{th}$ century thanks to the studies done by several scientists (T. Wulf, A. Gockel, V. Hess and R. Millikan among them) on the variation with altitude of the discharge rate of electroscopes. While the discharge of the sealed electroscopes was at first believed to be due only to the natural radioactivity of rocks, it should have been decreasing steadily with altitude. Instead, experiments done on top of the Eiffel Tower and later on board of manned hot-air balloons showed that the discharge did not follow the predicted constant attenuation law, and that on the contrary it even increased when over about 1.5 km from the surface: the conclusion was that the effect was caused by some ionizing radiation entering the Earth's atmosphere from above [1, 2, 3].

The discovery of cosmic rays represented the beginning of the study of the physics of elementary particles, as many of them were first detected as decay products of this radiation or by its interaction with suitable targets or detectors. This was for example the case of the discovery of the positron by C. Anderson in 1933 [4] (which impressively confirmed P. Dirac's prediction of the existence of antiparticles done five years

before [5]), or the identification of the muon also by C. Anderson and S. Neddermeyer in 1937 [6], or again the detection of the pion by C. Lattes, H. Muirhead, G. Occhialini and C. Powell in 1947 [7], after it had been predicted by H. Yukawa in 1935 [8]. Until the early 1950s, cosmic rays were the only source of particles with a high enough energy in order to create new particles or to study the structure of the nucleus. Later, with the advent of more and more powerful accelerator machines, subnuclear physics increasingly employed artificial beams in substitution of the cosmic radiation, and the interest of cosmic-ray physicists turned towards understanding the processes involved in the origin and the propagation of these particles rather than on using them as a source for experiments, thus giving contributions to the fields of astrophysics and cosmology too.

In recent years the discipline of astroparticle physics has been continuously growing and spreading to study still new subjects, as witnessed by the several and different experimental techniques which have been developed to investigate the various kind of particles and the very wide range of energies they have. Thus while at the ground level we can reveal the particles which have been produced by the interaction of the cosmic rays with the atmosphere which surround the Earth, the standard equipment to study cosmic rays from some tens of MeV to energies of about some hundreds of GeV are balloon-borne particle detectors having sensitive surfaces of the order of 1 $m^2$. To be able to lower the impact of the corrections which are necessary to account for the presence of the atmospheric gas, efforts have been made to build lighter and smaller detectors and to mount them on satellites, in this way revealing the cosmic rays before they can interact. Such experiments have to overcome extreme technological challenges in order to conciliate the requests of a detector for high-energy physics (such complex as the huge ones used at the particle accelerator experiments) in terms of dimensions and needed power, with the limitations imposed by a space mission. On the contrary other kinds of experiments take advantage of the presence of the gas surrounding the Earth in order to study the higher-energy cosmic rays, which are too rare to be revealed by means of standard-sized detectors. Actually, our planet's atmosphere is used as a huge detector in which such energetic cosmic rays can interact generating extensive showers of particles,

and the secondary products are then revealed on ground by means of large arrays of sensors covering surfaces even several square kilometers wide. Events with energy up to about $10^{20}$ eV have been measured with such kind of techniques, far beyond the highest limit which present accelerator machines can reach: by investigating such processes, the physics of cosmic rays can again give a contribution to the study of fundamental particle physics, being able to deal with experimental conditions which cannot be by now reproduced artificially in a laboratory. Understanding how so high energies can be achieved, and discovering which astrophysical mechanisms can be the source of such energetic particles are among the most interesting topics of this research field. Intriguing questions are also those to which physicists try to find an answer by means of detectors placed underground, shielded from most of the cosmic rays by large amounts of rock: in such noise-protected environments the faint signals coming from weakly-interacting or rare particles can be recognized and the open problems connected to neutrino physics or to the existence of dark matter can be investigated. Finally, another topic which needs further study is the presence of antimatter in cosmic rays: its detection has important implications related to the propagation of cosmic rays and on the possible presence of primary sources of antiparticles, which have consequences on fundamental aspects of cosmology and subnuclear physics.

In this work I present the analysis of the first data gathered at ground level by the PAMELA detector in the its pre-launch testing phase in 2005. The experiment will be mounted on a satellite and will reveal cosmic rays on a wide energy range, in particular looking for antiparticles: during the tests which have been performed on ground the majority of incoming particles consists instead of positive and negative muons. In the first chapter an introduction to general aspects of cosmic-ray physics is reported, with some details about the antiparticle question and about the characteristics of the radiation at the Earth's surface. In the next chapter the PAMELA mission, its objectives, and the sub-systems which compose the apparatus are described, and a full account of the magnetic spectrometer, which is the detector mainly involved in this work, is given. The data reduction and calibration procedures which have been developed for the spectrometer are illustrated in Chapter 3, while Chapter 4 is

fully dedicated to the complex question of the alignment of the detector. This is a crucial matter since a correct treatment of the mechanical misalignments of the detector is fundamental in order to measure particle momentum without introducing systematic errors. Finally, Chapter 5 contains the discussion of data analysis, and results about cosmic muons at ground level are shown.

# Contents

# List of Figures

# List of Tables

# Chapter 1

# Cosmic rays

*In many years of research, lots of questions about cosmic rays have been answered to and ideas about their origin, acceleration and propagation mechanisms have been proposed and discussed: yet several aspects still remain to be clarified and need further investigation. In this chapter a brief account of some generally well established features of the spectrum and composition of cosmic rays is given, together with the factors related to the influences that the Sun and the Earth have on them. A section of the chapter is dedicated to an introduction to the question of the presence of antiparticles in cosmic rays, with the presentation of the current experimental situation and of the open issues to be yet resolved. Finally some of the characteristics that the radiation shows as it reaches the surface of the Earth are discussed.*

## 1.1 Spectrum and composition

The expression "*cosmic rays*" was introduced for the first time by R. Millikan in 1926 [10] to indicate the extraterrestrial ionizing radiation which had been discovered by V. Hess [1, 2, 3] few years before, and whose composition was still unknown. Now the term is usually applied to all the charged particles and nuclei entering the Earth's atmosphere from space, and often it is extended to include other components such as high-energy photons or neutrinos. Particles coming from space are conventionally

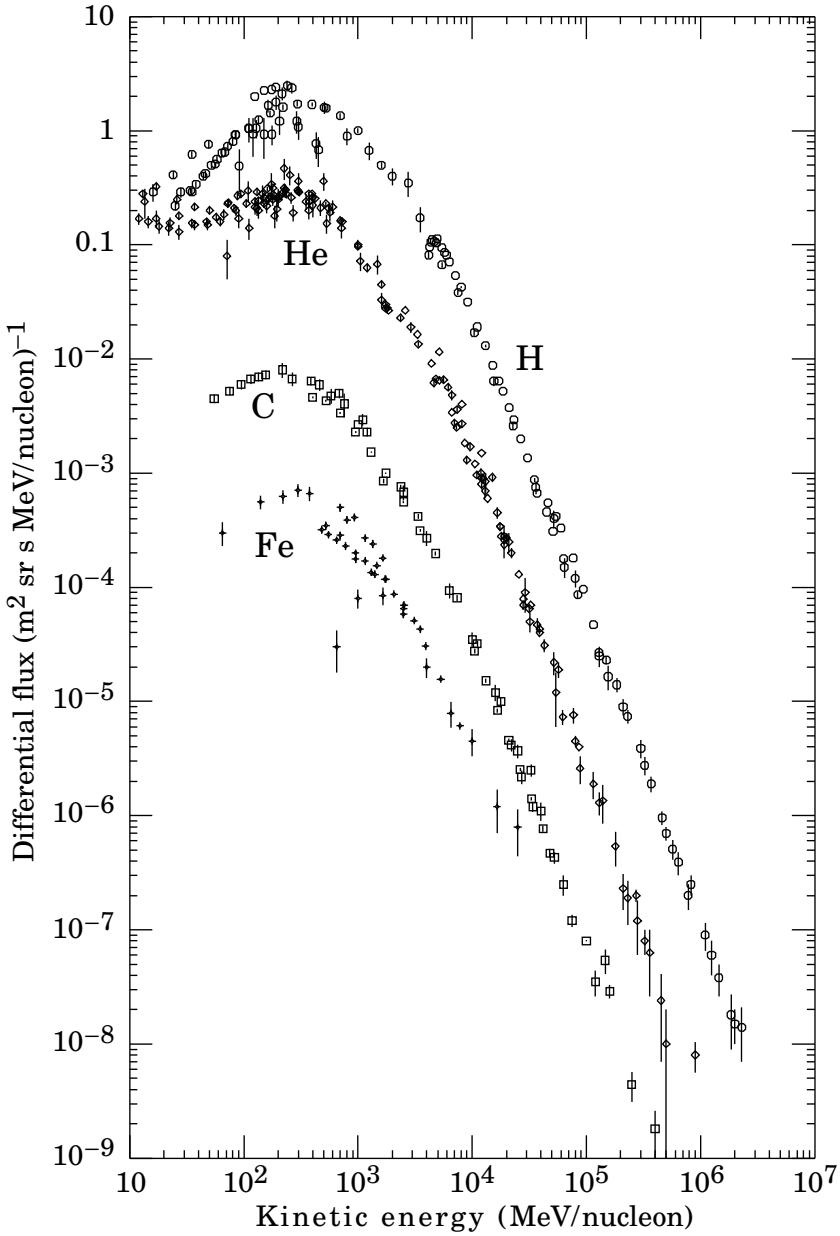


Figure 1.1: *Differential flux of the most abundant nuclear components of cosmic rays at the top of the atmosphere (from Ref. [9]).*

divided into two groups, called *primaries* and *secondaries*, according to their origin: *primary* cosmic rays are created and accelerated by some astrophysical sources and then they propagate through space and reach the Earth, while *secondaries* are particles and nuclei generated by the interaction of the primaries with the interstellar medium along their path. When dealing with cosmic-ray fluxes inside the atmosphere it is common to refer to the incident particles as the "primaries", and to those produced by its interaction with the molecules of the gas as the "secondaries": in order to avoid ambiguities in the terminology, in this work I will use the expression *atmospheric secondaries* to indicate this last group of particles.

Charged primaries and secondaries as revealed at the top of the atmosphere contain a little fraction of electrons (about 2% of the total) and an even smaller portion of antiprotons and positrons, while the major component is represented by ionized atomic nuclei (98%): among these, free protons are about 87%, helium nuclei about 12%, and heavier nuclei are only the remaining 1%. Their arrival rate integrated over all energies and added up for all the types of particles is about 1000 particles $\mathrm{m}^{-2}\ \mathrm{s}^{-1}$, while the way their number depends on their energy $E$ is usually expressed as the *differential flux* $I(E)$, defined as their number per unit area, time, solid angle and energy. Fig. 1.1 shows this quantity as measured at the top of the atmosphere for the most abundant nuclei in cosmic rays and for energies up to some units in $10^6$ MeV/nucleon. Instead in Fig. 1.2 the so-called "all-particle" spectrum (i.e. the spectra of the different components all added together) up to the highest measured energies is plotted. From the first picture we can see that all the spectra have as common feature the presence of a maximum around some hundreds MeV/nucleon and a regular decreasing behavior for higher energies.

Indeed in the region between about $10^9$ eV and $10^{15}$ eV the differential flux can be fairly well described by the power law:

$$I(E) \;\simeq\; 1.8\ E^{-\alpha}\ \frac{\text{nucleons}}{\text{cm}^2\ \text{s sr GeV}} \tag{1.1}$$

where $E$ here represents the energy-per-nucleon and $\alpha \simeq 2.7$ is the differential spectral index. The second plot shows that beyond about $10^{15}$ eV

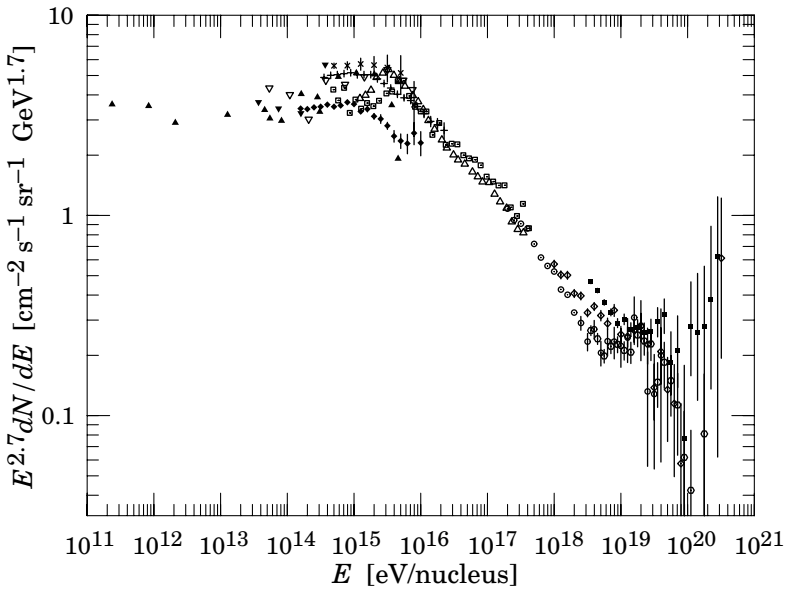


Figure 1.2: *Differential all-particle flux of the highest-energy cosmic rays. The flux has been multiplied by $E^{2.7}$ in order to enhance the visibility of the changes in the slope (from Ref. [9]).*

there is a steepening in the slope of the flux and the spectral index grows to about 3 for some energy decades, changing back to a lower value for $E > 10^{18}$ eV. This two features of the cosmic-radiation spectrum are called the *knee* and the *ankle*, respectively, and the reason of their existence is not well understood yet. Probably the changes in the power law have to be related to different mechanisms of particle acceleration and propagation. Standard theories on the origin of cosmic rays state that most of the non-solar component is produced by the shock waves existing in the regions around supernovae explosions inside our galaxy. Such regions, called *supernovae remnants*, are made of huge clouds of magnetized gas which expand even for hundreds of years after the explosion of the star: near the shock front, charged particles could gain energy till their speed is too high for the magnetic field to constrain them in the acceleration region, and they would eventually escape into the galaxy. In this way the source would be characterized by a maximum reachable

energy which depends on its size and on the intensity of its magnetic field. According to this scenario the lower-energy change in the spectral index could reflect the fact that some of the galactic accelerators of cosmic rays have reached the upper limit beyond which the process no longer provides particles in an efficient way, and indeed theoretical calculations show that shock-wave mechanisms could account for spectra displaying the *knee* feature. The region beyond the *knee* could represent a higher-energy population of particles overtaking the lower-energy one associated to supernovae remnants. The origin of the highest portion of the spectrum remains unclear but several possible explanations have been proposed, suggesting that the cosmic rays above the *ankle* could have origin from extragalactic sources or that they could be the decay products of exotic massive particles such as those predicted by extensions of the Standard Model of particle physics.

The wide extension of the cosmic-ray spectrum, spanning over thirteen orders of magnitude, and the associated large variation in the number of particles, require experiment to use several techniques in order to perform measures in the different energy regions. So, while below the *knee* direct measurements can be done by means of detectors on board of aerostatic balloons or satellites, thus allowing the identification of cosmic particles before they interact in the atmosphere, at higher energies the low flux limits the number of detectable events for the typical acceptances of this kind of experiments. On the other hand, in this region the high energy of the incoming particles can be exploited through indirect-measurement techniques: in fact the showers of atmospheric secondaries can be revealed on ground and the characteristics of the primary can be estimated if the interaction cross sections with air molecules and the details regarding the atmosphere, which acts as a target, are well known.

The presence of the maximum in the spectra in Fig. 1.1 is known to be due to an attenuation of the flux of low-energy galactic cosmic rays reaching the Earth, which is caused by the so-called *solar wind* and by the terrestrial magnetic field. The solar wind consists of a continuous flux of low-energy electrons and light ionized nuclei which the Sun emits with speed ranging from 300 km/s to 800 km/s, and which create in the

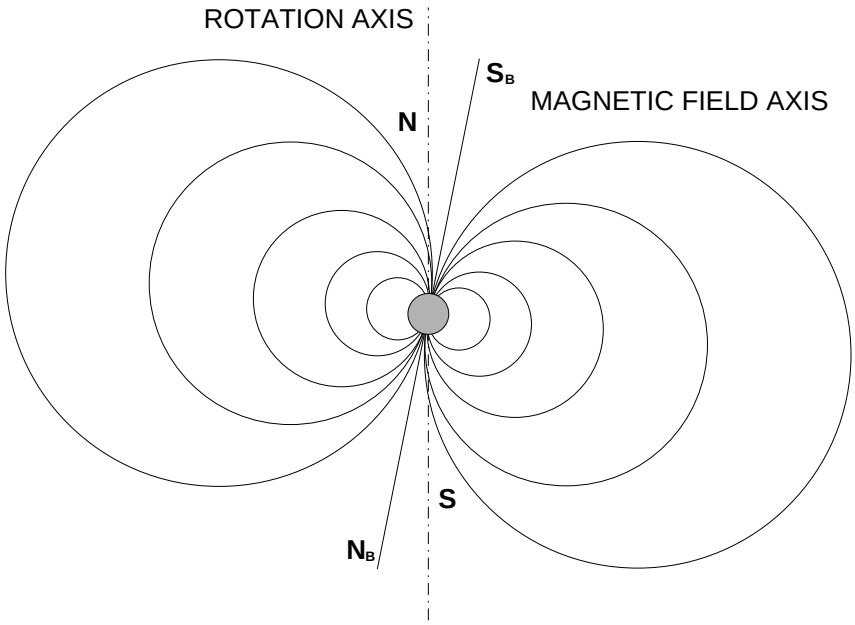


Figure 1.3: *Sketch of the magnetic field of the Earth, showing the inclination of the magnetic axis and the location of the magnetic poles* $N_{\mathrm{B}}$ *and* $S_{\mathrm{B}}$ *with respect to the geographic ones.*

space around the star a magnetic field extending in the solar system as far as about 100 AU[1]. The magnetic field deflects the low-energy part of the incoming cosmic radiation, which is somehow also slowed down in its interaction with the particles of the solar wind, and it is thus prevented from reaching us. The overall effect is a variation of the flux below some tens of GeV, which is known as *solar modulation*, strongly correlated to the activity of the Sun, which in turn is not constant but follows a cycle with a period of about 11 years: the higher is the production of solar particles, the lower is the number of galactic cosmic rays capable of reaching the Earth. A last effect due to the Sun occurs occasionally when bursts of energetic particles are emitted during *solar flares* or in

[1]The Astronomical Unit (AU) is the mean distance between the Sun and the Earth and it corresponds to about $149\ 598 \cdot 10^3$ km.

the course of *coronal mass ejections*: in such events, particles up to some tens of GeV are sent out into space and they add to the low-energy end of the cosmic-ray spectrum.

As previously stated, a contribution to the reduction of the amount of cosmic radiation comes from the Earth's influence too. Its magnetic field, probably sustained by the electric currents connected to the movements of the melted masses inside the planet, follows a nearly-dipolar behavior (see Fig. 1.3) having its axis inclined of about 11° with respect to the Earth's rotational one, and its magnetic north pole being located in the southern hemisphere. The intensity of $\boldsymbol{B}$, expressed in Gauss, is given approximately by:

$$B(r, \lambda) \simeq \frac{0.31 \text{ G}}{(r/r_E)^3} \sqrt{1 + 3 \sin^2 \lambda} \tag{1.2}$$

where $\lambda$ represents the geomagnetic latitude, which depends on both the geographical latitude and longitude (because of the inclination of the axis of the dipole), $r_E$ is the radius of the Earth, and $r$ is the distance between its center and the point of interest. The presence of $\lambda$ in the above expression for the field causes the cosmic-ray attenuation effect to depend on the geographical location on the surface: for this reason, a so-called *geomagnetic cut-off* effect is present, which is commonly expressed by giving the minimum rigidity that a perpendicularly moving particle needs in order to reach the Earth in spite of the magnetic field deflection. The *rigidity* $R$ of a particle is defined as the ratio:

$$R = \frac{p}{q} \tag{1.3}$$

between the magnitude of its momentum $p = |\boldsymbol{p}|$ and its charge $q$, and it is usually expressed in GV/$c$. Rigidity is a fundamental quantity when dealing with charged particles moving inside a magnetic field since particles with different momentum and charge but identical rigidity are bent in the same direction with the same curvature because of the Lorentz force (see also Sec. 2.4). The variation of the cut-off with geomagnetic latitude $\lambda$ can be approximated by the following expression [11]:

$$R_{\text{cut-off}} \simeq 14.9 \text{ GV}/c \cos^4 \lambda \,. \tag{1.4}$$

Not only the spectrum of cosmic rays is interesting, but also the detailed study of their nuclear composition can provide valuable information, in particular about their history and their propagation mechanisms. The primary nuclear species which we reveal in the cosmic radiation are all those with a lifetime of the order of $10^6$ years or longer, and since those particles should have been produced by primordial and/or stellar nucleosynthesis (independently of the nature of the sources which have accelerated them), it would be reasonable to expect that the elemental abundances we find in cosmic rays are similar to those found in the solar system. The experimental situation as reported in Fig. 1.4 actually exhibits a quite similar profile for both of them, showing the typical *odd-even* effect due to the difference in nuclear binding energies, and a predominance of hydrogen, helium, carbon, nitrogen, oxygen and iron over their nearest elements. Conversely, an evident disagreement between the two sets of data can be seen in the elements with a $Z$ just below the C-N-O group and below Fe. Those nuclei, which are almost absent in the solar system, are likely to be the secondary products of a process called *spallation* in which a primary high-$Z$ nucleus interacts with the interstellar medium and breaks into two or more lower-$Z$ elements: this mechanism, applied to the most abundant species, could be responsible for filling up the gaps in the composition profile. The knowledge of the spallation cross sections and of the secondary-primary ratios let us estimate the amount of matter traversed by cosmic rays along their path from the sources to the Earth [13]. Standard calculations for particles in the GeV-energy region give a value ranging from 5 to 10 g/cm$^2$ of hydrogen and this, being about 1000 times greater than the thickness of the galactic disk, implies that these charged particles are kept confined for a long time by the galactic magnetic field within a limited volume. The confinement region can consist of part or all of the disk, and possibly the less-dense spherical halo surrounding it, as suggested by the synchrotron emission observed in edge-on spiral galaxies and by the estimate of the

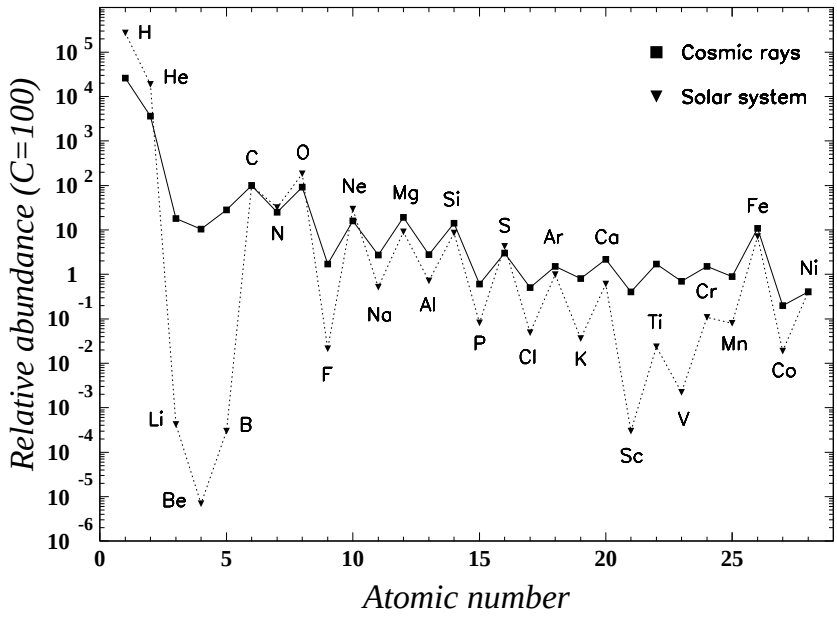


Figure 1.4: *Relative abundance of the nuclear components of cosmic rays with Z=1–28 as measured at 1 AU, compared to that of the elements in the solar system. The vertical scale is normalized to an abundance of carbon equal to 100 (adapted from Ref. [12]).*

density of matter found along the path, which can be obtained from the study of radioactive cosmic-ray nuclei. This is another important aspect arising from the study of the nuclear composition of cosmic rays: in fact, some of the secondaries generated through spallation are unstable radioactive elements and the abundance of them with respect to their progenitor nuclei can give significant information about the history of the particles, such as also the time spent traveling in space by the cosmic radiation. Typical estimates of this quantity give a time of the order of $10^7$ years, being in agreement with the high degree of isotropy which we observe.

### 1.1.1 Antiparticles in cosmic rays

As previously stated at the beginning of Sec. 1.1, the cosmic rays which we reveal at the top of the atmosphere contain a small fraction of antiparticles, namely antiprotons and positrons. Since their discovery in cosmic rays, and more thoroughly by means of accelerator experiments, antiparticles have always been observed to be created only in pair with their associated particles. Combined with the reasonable and widely held hypothesis of a initially symmetric universe as from the inflationary "Big Bang" model, this symmetry attribute in the laws regulating antimatter creation points out a still unsolved issue of astrophysics, cosmology and fundamental physics: that is, why what we have till now observed of the universe seems to be composed almost completely by matter, and why we do not reveal equivalent amounts of antimatter as well. The most satisfactory solutions one can picture to this question are either that the initial symmetry has been being actually preserved throughout the history of universe (at least to some extent), and regions of it composed of antiparticles do really exist, or that some mechanism worked toward unbalancing the ratio in favor of standard matter, so that antimatter already annihilated completely in the past and no more remains nowadays. Up to now, theory and experiments seem not to be able to account for the conditions which are needed for such a mechanism to exist [14]. On the other hand, if the correct explanation were that antimatter-dominated regions are present in the universe, then they should be separated from standard-matter regions at least at the level of clusters of galaxies, otherwise intense $\gamma$-ray emissions originating from the annihilation at the border areas should have been observed, while they are not. In this scenario, if the cosmic radiation could actually escape the galaxy in which it is produced, and it could move through the intergalactic space and reach us, we might be able to detect cosmic rays which include antiparticles originating from galaxies made of antimatter (through processes analogous to the ones taking place in ours). Such direct research for cosmic antiparticles is a especially challenging task, as the signal we are looking for is a very small fraction over a much larger background (e.g. there are about $10^4$ protons for every antiproton in cosmic rays). Besides this, the measure of $\overline{p}$ and $e^+$ fluxes is also interesting for the study of *dark*

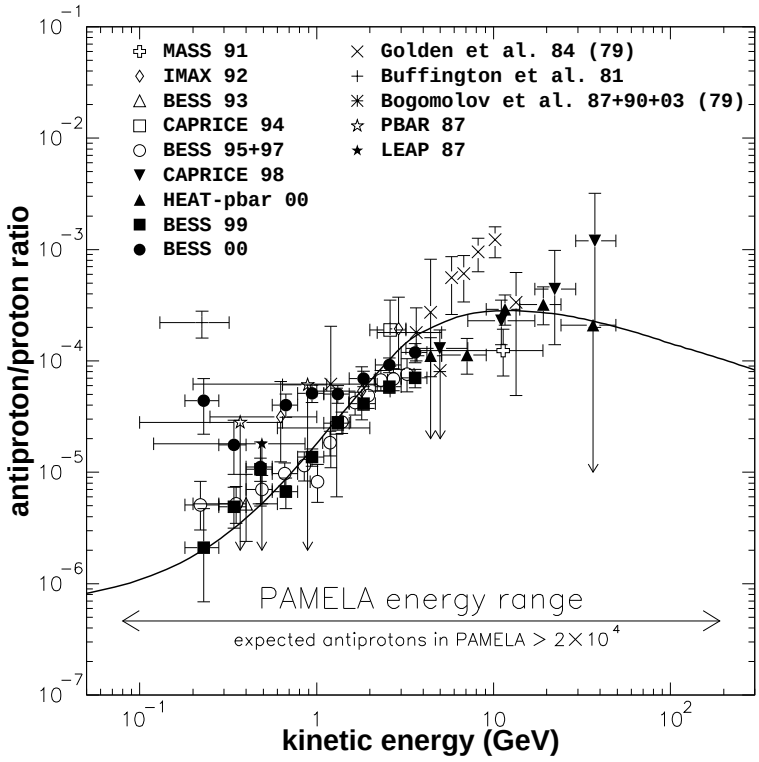


Figure 1.5: *Antiproton-proton ratio as a function of energy as measured at the top of the atmosphere, compared with the expected energy range covered by the PAMELA experiment. The line shows the result of a theoretical calculation based on a purely secondary production of $\overline{p}$ in the interstellar medium [15]. References for data are: Golden* et al. *[16, 17], Buffington* et al. *[18], Bogomolov* et al. *[19, 20, 21, 22], PBAR 87 [23], LEAP 87 [24], MASS 91 [25], IMAX 92 [26], BESS 93 [27], CAPRICE 94 [28], BESS 95+97 [29], CAPRICE 98 [30], HEAT-pbar 00 [31], BESS 99 and BESS 00 [32].*

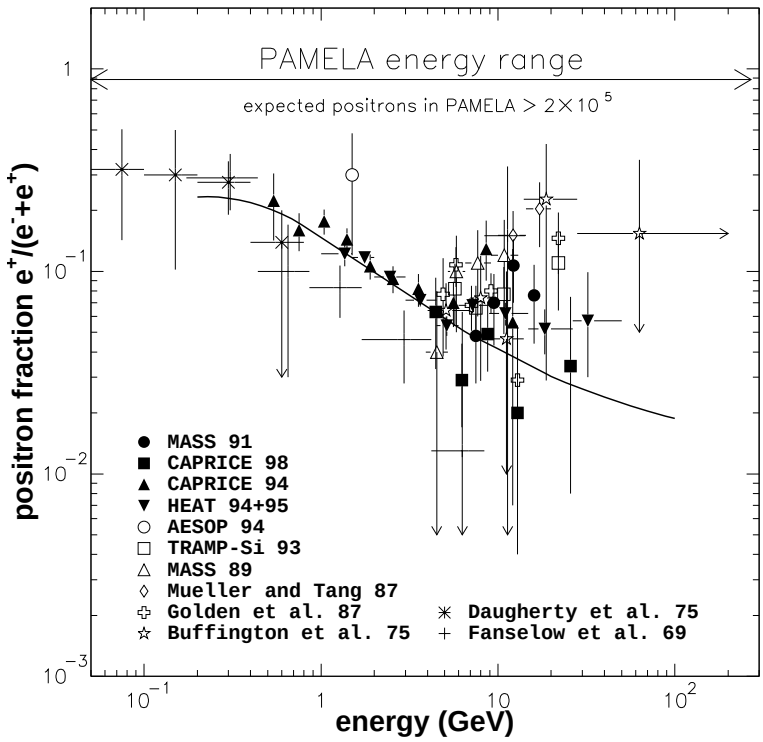


Figure 1.6: *Positron fraction as a function of energy as measured at the top of the atmosphere, compared with the expected energy range covered by the PAMELA experiment. The line shows the result of a theoretical calculation based on a purely secondary production of $e^+$ in the interstellar medium [33]. References for data are: Fanselow* et al. *[34], Daugherty* et al. *[35], Buffington* et al. *[36], Golden* et al. *[37], Müller and Tang [38], MASS 89 [39], TRAMP-Si 93 [40], AESOP 94 [41], HEAT 94+95 [42], CAPRICE 94 [43], CAPRICE 98 [44], MASS 91 [45].*

*matter*. In fact the detection of antiprotons and positrons generated by the annihilation of the lightest stable supersymmetric particles, neutralinos (which seem to represent the best candidate for being the bulk of the non-baryonic non-luminous matter needed to explain the dynamical behavior of galaxies), is considered as one of the most competitive approaches to this subject, when compared to other proposed methods such as the revelation of high-energy neutrinos coming from the decay of neutralinos or the direct detection of dark matter.

The current experimental situation concerning $\overline{p}$ and $e^+$ measurements is shown in Fig. 1.5 and in Fig. 1.6, while as regards the detection of antinuclei, none has ever been found up to now and only upper limits on their existence has been set (e.g. the present limit in the rigidity range 1–14 GV/$c$ is $6.8 \cdot 10^{-6}$ for the antihelium-helium ratio [46]). All the reported spectra have been obtained by balloon-borne detectors, and the dominant experimental errors are due to the short data-taking time and to the correction to the measured number of events which is necessary to account for the presence of a residual layer of atmospheric gas at the height that a balloon can reach. As it can be seen from the theoretical computations drawn in the plots, both the antiproton and the positron components of cosmic rays could agree with a purely secondary origin of these antiparticles, namely from the $pp \rightarrow ppp\overline{p}$ reaction (as confirmed by the attenuation below about 10 GeV, which is a signature of the kinematic suppression due to the threshold of the reaction), and from the decay of $\mu^+$ coming in turn from the decay of $\pi^+$ produced by the interaction of high-energy primaries in the interstellar medium, respectively. Nonetheless, considering the experimental errors and the uncertainties (not reported in the pictures) included in the various theoretical models, probably a definitive conclusion cannot be stated on this matter yet. In order to unambiguously demonstrate the presence of antigalaxies as a source of antiparticles, either antinuclei should be detected (as they have a negligible production cross section except for their hypothetical creation by nucleosynthesis in antimatter stars), or more precise measurements of the higher part of the $\overline{p}$ spectrum should be made, since that is the region where the largest differences between the secondary production models and a possible primary flux due to antimatter regions

are expected to be found.

The PAMELA experiment has as its primary objectives the measurement the spectrum of $\overline{p}$ and $e^+$, on an energy range wider than the one explored till now by analogous experiments and with much higher statistics (as reported in Fig. 1.5 and 1.6), and also the research for the possible presence of antinuclei in cosmic rays. Detailed characteristics of the physics which this detector aims to study will be discussed in Sec. 2.2.

## 1.2 Cosmic rays at the Earth's surface

The atmosphere which surrounds the Earth is essentially composed of nitrogen and oxygen, and it extends for hundreds of kilometers from the surface of the planet. Actually, even if about half of its mass is located within 5 km from the ground, there is no abrupt boundary between the atmosphere and the outer space: on the contrary its depth, starting from an initial value of about 1000 g/cm$^2$ at the sea level, gets lower and lower as it vanishes outwards. When cosmic rays coming from space cross the atmosphere they are subject to interactions with the electrons and the nuclei of the atoms which constitute the air, and also to energy losses due to ionization and radiative processes. Consequently, the composition of the cosmic-ray beam changes as it gets lower in altitude, in such a way that while on top of the atmosphere protons and electrons form the main fraction, at the sea level most of the particles are neutrinos and muons. Since the nuclear interaction length (which represents the interaction mean free path of a particle and accounts for its probability to undergo a strong interaction) for an ordinary primary proton is small (about 90 g/cm$^2$), as compared to the atmospheric depth, nearly all the cosmic rays interact. Some of the typical processes arising in the interaction are sketched in Fig. 1.7. Atmospheric secondaries generated by the incoming particle and by subsequent reactions and decays can be divided into three categories: a *nucleonic component* containing nucleons or light nuclei created by the fragmentation of the incoming particle or of the target nucleus, a *hard component* generated by the decay of mesons into muons, and a *soft component* which includes electromagnetically interacting photons and electrons. Neutrinos (not displayed in the picture)

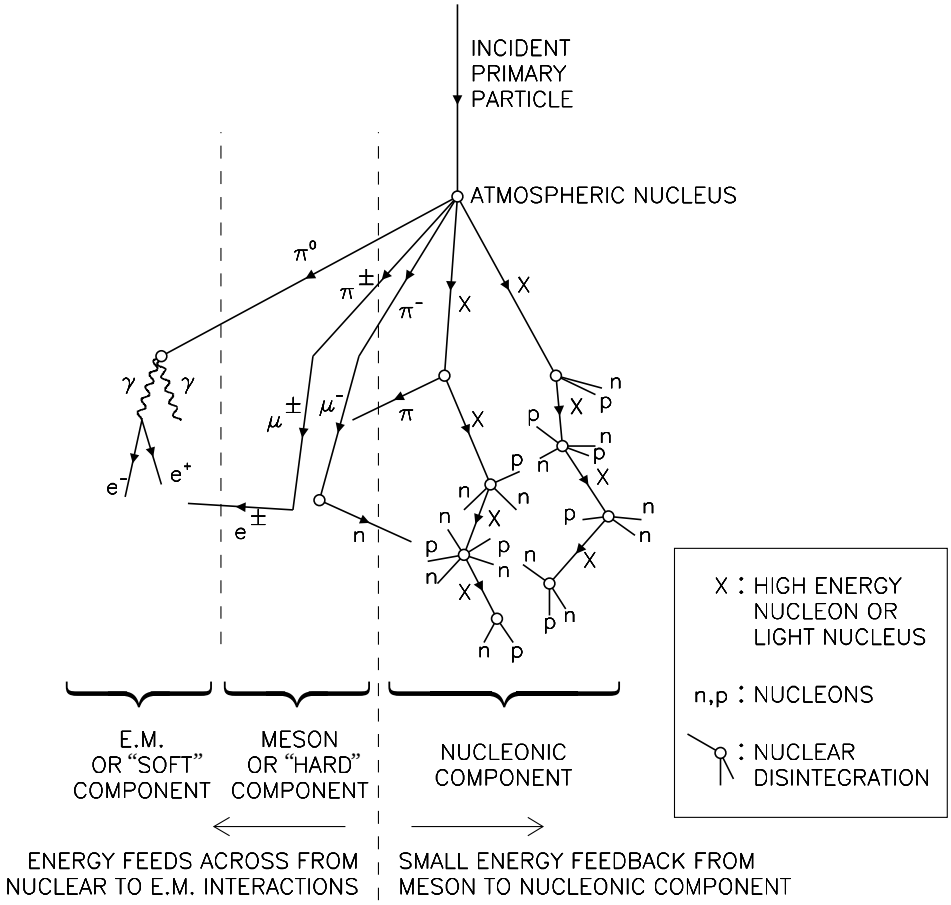


Figure 1.7: *Schematic diagram of particle interactions in the atmosphere, displaying the* nucleonic component *due to the fragmentation either of the incoming particle or of the target nucleus, the so-called* hard component *due to mesons decaying into muons, and the* soft component *due to particles which interact electromagnetically. For simplicity, neutrinos resulting from decays are not shown.*

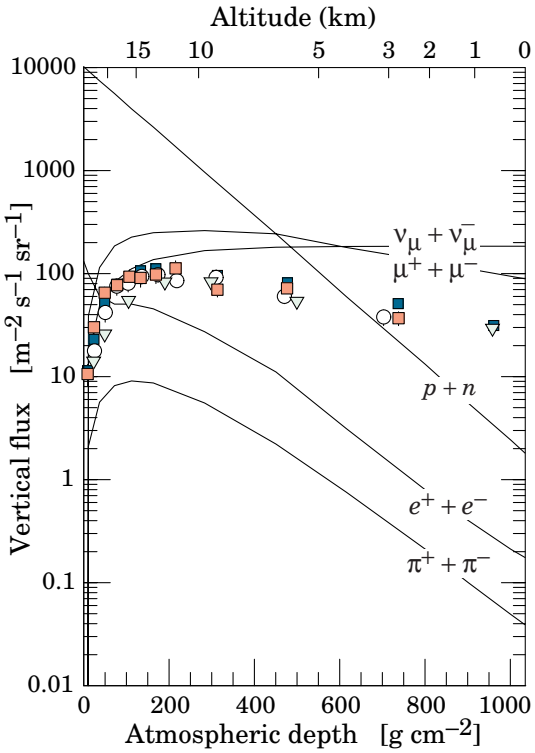


Figure 1.8: *Vertical fluxes of cosmic rays with $E > 1$ GeV in the atmosphere as a function of altitude. The lines refer to the theoretical behavior of the various components as expected on the basis of the primary flux at the top of the atmosphere, while the points are experimental measurements of $\mu^-$ (from Ref. [9]).*

are also created in the decay of mesons and muons. Particles belonging to the nucleonic component can in turn interact as long as they are energetic enough; then they lose energy by ionization in the gas. Pions and kaons, which are the most abundantly produced mesons, are usually present only in the first layers of the atmosphere, because even if their interaction length is greater than that of protons, they are short-lived unstable particles ($\tau_{\pi^\pm} = 2.603 \cdot 10^{-8}$ s, $\tau_{K^\pm} = 1.238 \cdot 10^{-8}$ s). The electromagnetic component originates essentially from decaying $\pi^0$, and it propagates by pair creation and bremsstrahlung till $e^\pm$ fall below their critical energy.

The relatively long lifetime of muons ($\tau_\mu = 2.197 \cdot 10^{-6}$ s), combined with the relativistic effect of time dilation, make a large fraction of them able to survive and hit the ground. As a result, commonly only muons and neutrinos can reach the Earth's surface: yet, if the incoming particle has enough energy, its interaction can create a cascade of reactions resulting in a shower which can be detected even on ground. These events usually develop around a core of hadronic particles acting as a source of several electromagnetic subshowers: electrons and positrons produced in such air showers are about one order of magnitude more abundant than muons.

Figure 1.8 shows the vertical fluxes of cosmic rays above 1 GeV in the atmosphere as estimated by theoretical models, compared with some experimental data of negative muons. The behavior which is expected on the basis of the processes outlined above is confirmed: the number of nucleons and electrons, which are the main components at high altitude, falls quickly as they interact with air, but the profile of $e^\pm$ is soon enhanced by the atmospheric secondaries; the peak in the intensity curve of pions around 15 km accounts for their production in the first interactions and for their subsequent decay; muons, being produced by decaying mesons but having a longer lifetime, show a similar shape but with the maximum shifted towards lower altitudes; the number of neutrinos just increases due to their negligible interaction cross section. In summary, the most abundant charged particles which can be detected at the sea level with energy greater than 1 GeV are muons, plus a small fraction of protons (about 1/100), and an even smaller one of electrons and positrons (about 1/1000).

The study of the muon component on ground is interesting because of its importance in calibrating the parameters of the models which describe the interactions of cosmic rays in the atmosphere. In particular, since $\mu^+$ ($\mu^-$) are produced in association with $\nu_\mu$ ($\overline{\nu}_\mu$) and they can be revealed more easily than neutrinos, they represent a useful tool for understanding the so-called "atmospheric neutrino anomaly", that is to say the lower number of measured muon neutrinos in the atmosphere with respect to the predicted one, which is among the proofs supporting the existence of neutrino oscillations. A world survey of the present experimental situation of muon flux measurements at the sea level as a function

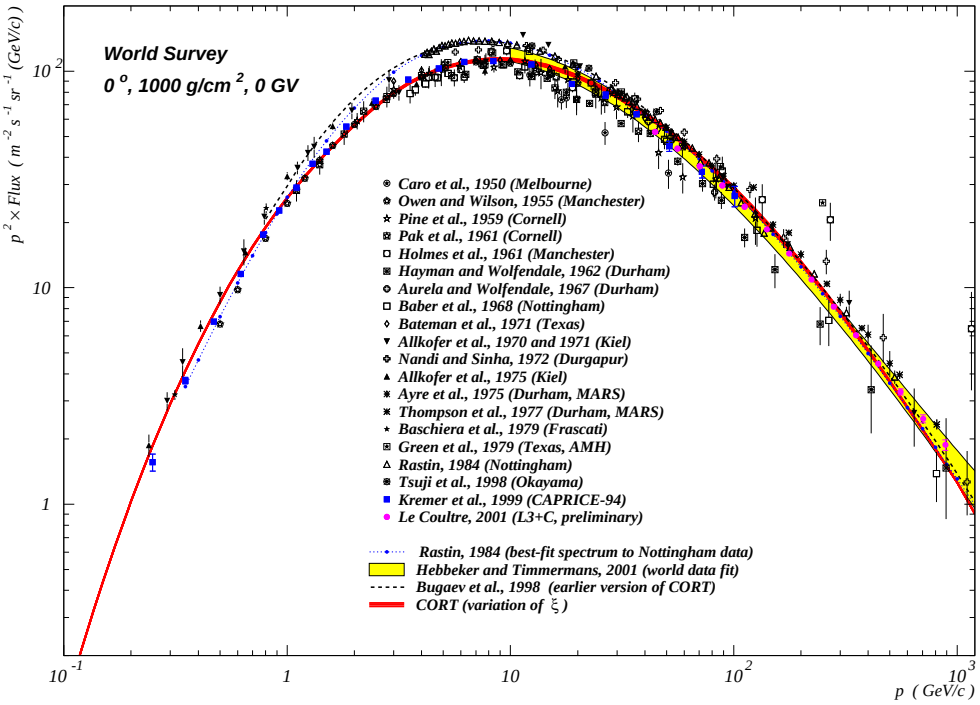


Figure 1.9: *World survey of muon differential flux measurements on ground in the vertical direction at low geomagnetic cut-off as a function of momentum. Fits of data and theoretical calculations are shown too. The flux has been multiplied by $p^2$ for the sake of visibility (from Ref. [47], which contains the references to data and models).*

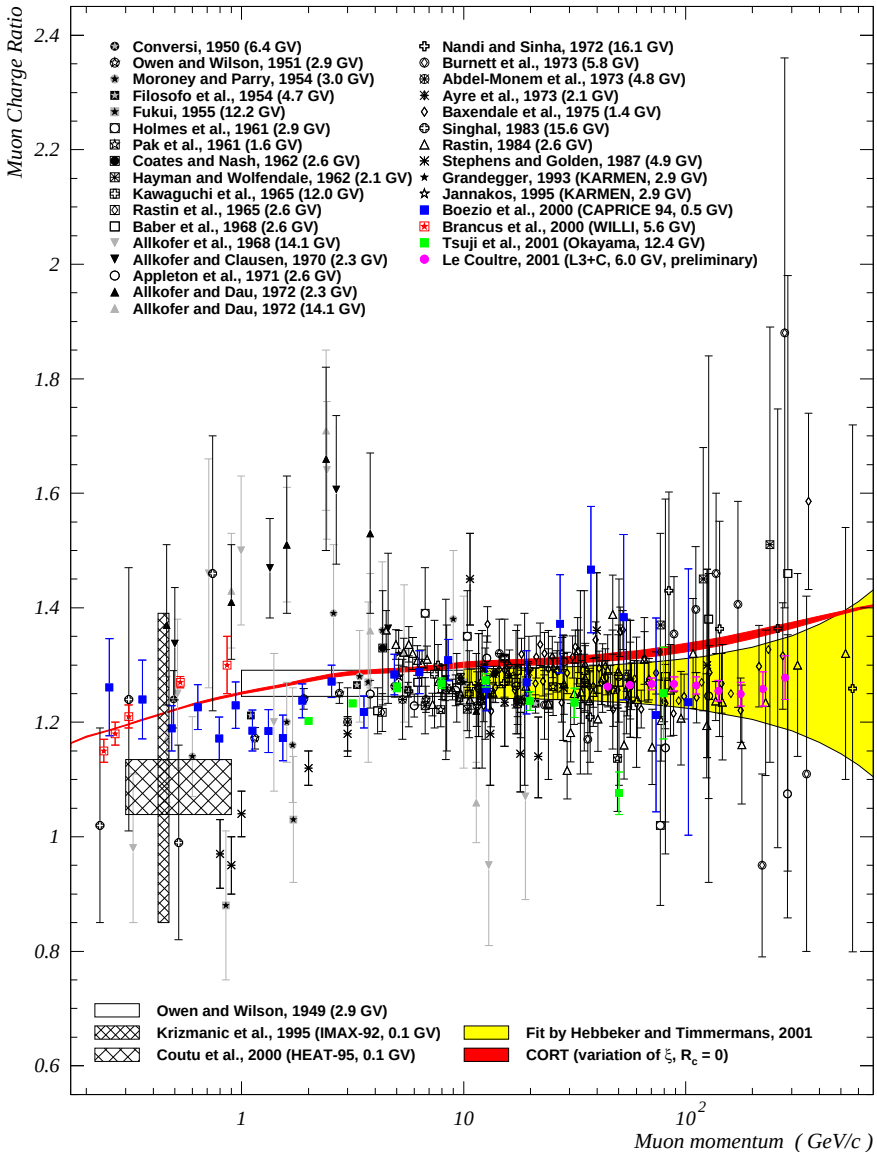


Figure 1.10: *World survey of muon charge-ratio ($\mu^+/\mu^-$) measurements on ground as a function of momentum. The cut-off rigidity associated to each experiment is indicated. Fits of data and theoretical calculations are shown too (from Ref. [47], which contains the references to data and models).*

of momentum is displayed in Fig. 1.9 (the flux has been multiplied by $p^2$ for the sake of visibility). Below 1 GeV/$c$ the flux is almost flat, it steepens gradually to reflect the shape of the spectrum of primaries till about 100 GeV/$c$, and then it steepens further because of the decrease in the number of muons produced by decaying pions, which tend to interact rather than to decay at such high energies. Figure 1.10 shows instead the muon charge ratio $\mu^+/\mu^-$ at the sea level as a function of momentum. The ratio appears to be nearly constant but large uncertainties are evident from the wide scattering of the data, in particular below some GeV where there is a systematic dependence on location, due to geomagnetic effects, and at high energies where statistics is poor. The excess of positively charged particles is due to the greater number of protons as compared to neutrons in primary cosmic rays, and of $\pi^+$ with respect to $\pi^-$ being produced in proton initiated interactions.

# Chapter 2

# The PAMELA experiment

*The PAMELA experiment is the most recent result of the work started several years ago in cosmic-ray research within the WiZard group. WiZard is a collaboration which was originally formed around R. Golden, who first observed antiprotons in the cosmic radiation in 1979 [16] (in the same year as the Russian team lead by E. Bogomolov [19]). During the last fifteen years the group ran several balloon flights (MASS 89 [39], MASS 91 [25, 45], TRAMP-Si 93 [40], CAPRICE 94 [28] and CAPRICE 98 [30]) using a combination of highly sophisticated and new for space detector systems, such as a spectrometer with a superconducting magnet, imaging streamer tubes and silicon-tungsten calorimeters, a transition radiation detector, solid and gas ring-imaging Cherenkov detectors.*

*Currently, fifteen institutions from six countries are involved in the PAMELA experiment: INFN (National Institute of Nuclear Physics) groups in Bari, Florence, Naples, Rome "Tor Vergata" and Trieste, INFN National Laboratories in Frascati and IFAC-CNR in Florence, from Italy; Moscow Engineering and Physics Institute, Lebedev Institute in Moscow and Ioffe Institute in St. Petersburg, from Russia; the Physics Department of the Royal Institute of Technology in Stockholm, from Sweden; the Physics Department of Siegen University, from Germany; and groups from New Mexico State University in Las Cruces and NASA Goddard Spaceflight Center from USA, and from Tata Institute of Fundamental Research in Mumbai, India. Unlike the previous high-energy cosmic-rays*

*experiments of the WiZard group, the PAMELA detector will fly on board a satellite. The opportunity of the flight is given by a collaboration called RIM* (Russian-Italian Mission) *which since 1995 has been allowing Italian cosmic-ray instruments to go into orbit around the Earth on the Mir Space Station (SilEye experiments [48, 49], silicon sensor telescopes which have been used to study the radiation environment inside the Mir) and on Resurs series satellites (NINA experiment [50], a silicon detector system used to investigate nuclear and isotopic composition of low-energy ($E < 1$ GeV) cosmic rays).*

## 2.1 Mission overview

The PAMELA experiment is the main component of the scientific equipment carried by the Resurs DK1, a satellite for monitoring the surface of Earth, produced by the *Central Specialized Design Bureau - Progress* (TsSKB-Progress) in Samara, Russia. The instrument (see Fig. 2.1) is going to be put into orbit by a Soyuz rocket, whose launch from the Baykonur cosmodrome, in Kazakhstan, is scheduled for the beginning of 2006. The Resurs DK1 will fly on an elliptical quasi-polar orbit, at a variable altitude between 350 km and 600 km, with an inclination of 70.4° with respect to the Equator and a period of about 90 minutes, in this way crossing regions with various geomagnetic cut-offs along its travel around the planet. In this configuration the expected mission duration, being limited by the residual atmospheric drag, is longer than three years.

Direct detection of cosmic rays on satellite has several advantages compared to balloon-borne experiments, particularly when looking for the rarest components of the cosmic radiation: as stated in Sec. 1.1.1 the main sources of uncertainties in the measured flux of antiparticles are the corrections which have to be made to account for the presence of the atmospheric layers over the instrument (the typical altitude for balloons is about 40 km) and the limited exposure time of the detector (usually balloons can fly for periods ranging from one day to few days, even if long-duration flights lasting about 100 days have been proposed). On the other hand, building a detector for high-energy physics with the characteristics needed to be put on board a satellite is not an easy task. Besides

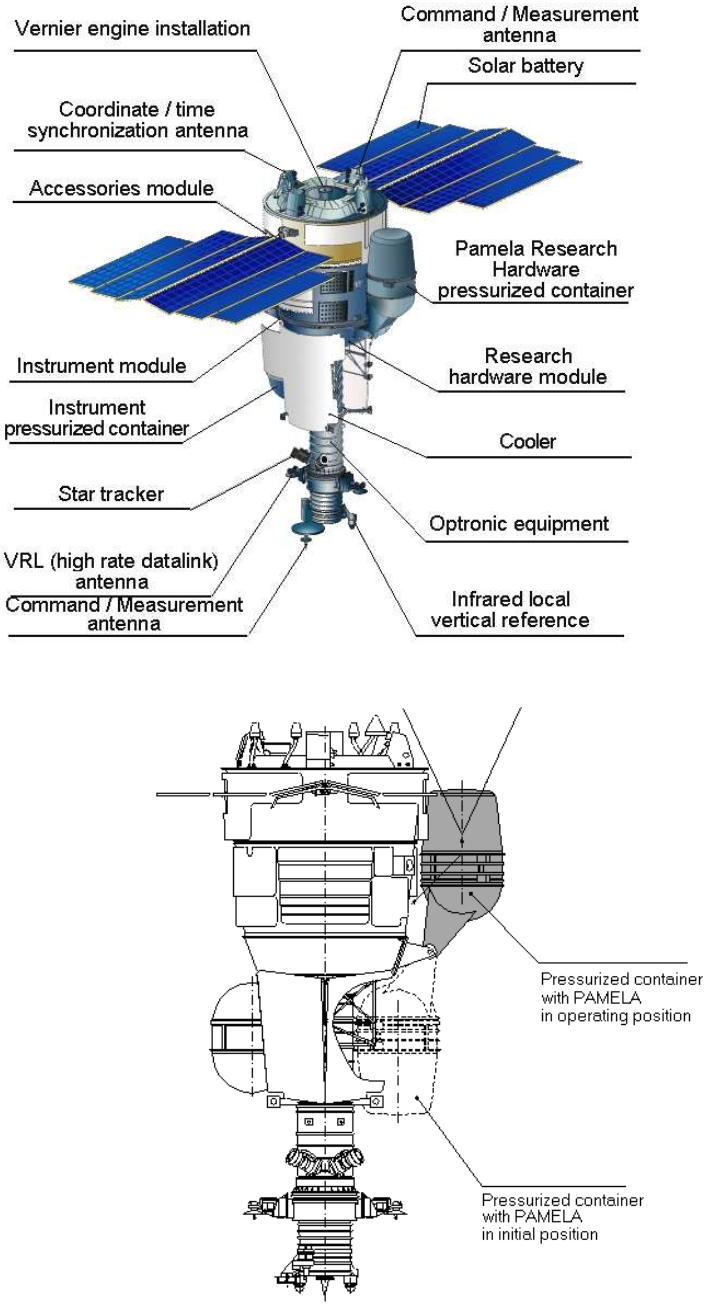


Figure 2.1: *The Resurs DK1 satellite. In the upper part of the figure, the different satellite devices are indicated; in the lower part, the positions of the container of the PAMELA detector during initial and operating phases are shown.*

the high costs of such kind of space missions, the main issues are the restrictions to the maximum weight and size of the scientific and auxiliary equipment, and the very limited power available for the instruments (see Sec. 2.3 for details on PAMELA specifications). Moreover a remarkable difference between a space and a standard particle-physics experiment is that in the first case the detector must fulfil strict requirements in terms of mechanical resistance to withstand the stresses of the take-off phase, and that its systems have to be designed including space-qualified electronics and a high degree of redundancy, since once the satellite has been launched it must survive and work for several years in the presence of ionizing radiations and challenging environmental conditions without any maintenance. Additionally, all the functioning procedures of the device, such as acquisition modes and automatic emergency operations, have to be foreseen and planned before departure, since for most of its lifetime only minimal interventions from ground will be possible.

The PAMELA detector will be housed in a pressurized container filled with nitrogen kept at a pressure of 1 atm and at a temperature between 0° C and 45° C. The container is connected to the satellite body with a mechanical arm which allows to move the detector from the safety position in which it is kept during the launch, and to point it towards the open space in order to give it the maximum field of view while taking data (as shown in Fig. 2.1). Furthermore the instrument will be put back to its initial place for the periodic adjustments to the satellite trajectory which are necessary to keep it on the planned orbit.

## 2.2 Scientific objectives

The enhancement of the measure of antiproton and positron spectra and the extension of their energy range beyond the present limits are the primary scientific objectives of the experiment. Such improvements will be achievable thanks to the possibility to detect cosmic rays outside the atmosphere using an instrument endowed with high precision and with a wide detection range, able to measure the momentum of antiparticles and to identify them in a much larger particle background. While being optimized for the measurement of these rare components of cosmic

rays, PAMELA will anyway reveal at the same time the more abundant particles too, that is to say protons, nuclei and electrons. According to the design of the experiment, the expected detection capabilities of the instrument are the following (see also Fig. 1.5 and Fig. 1.6):

- measure of the spectrum of antiprotons from 80 MeV to 190 GeV (current limits 200 MeV $\div$ 40 GeV);
- measure of the spectrum of positrons from 50 MeV to 270 GeV (current limits 70 MeV $\div$ 40 GeV);
- research of antinuclei with a sensitivity better then $10^{-7}$ in the antihelium-helium ratio, from 100 MeV/nucleon to 70 GeV/nucleon (current limit $6.8 \cdot 10^{-7}$);
- measure of the spectrum of protons from 80 MeV to 1 TeV;
- measure of the spectrum of electrons from 50 MeV to 800 GeV;
- measure of the combined spectrum of electrons and positrons up to 2 TeV;
- measure of the spectrum of nuclei up to about $Z = 6$ from 100 MeV/nucleon to 500 GeV/nucleon.

During three years of data taking about $2 \cdot 10^4$ $\overline{p}$ and $2 \cdot 10^5$ $e^+$ are expected, this being a noticeable improvement in the current state of measurement of their spectra, since for instance about only 500 antiprotons have been detected up to now by balloon-borne experiments.

The long exposure time and the characteristics of the orbit will also allow to study the effect of the solar modulation on the low-energy end of the cosmic-ray spectrum and to register solar-flare events occurring in such a period, measuring the energy distribution and the time profile of particles emitted by the Sun.

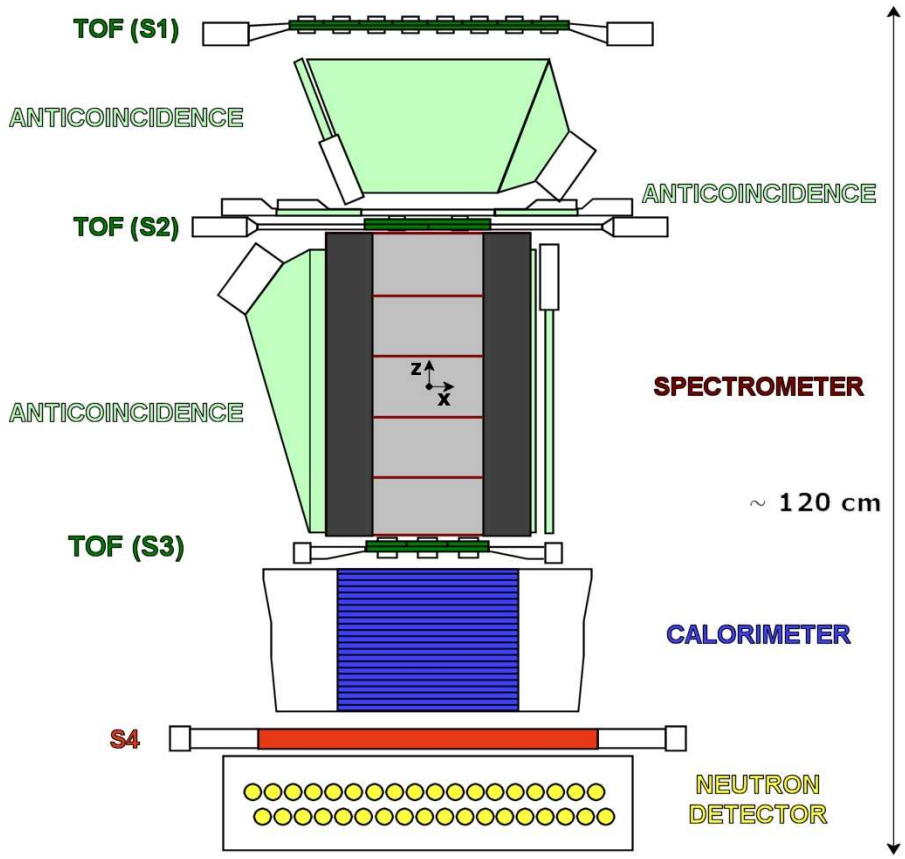


Figure 2.2: *Schematic drawing of the PAMELA detector, showing the sensitive areas of the various sub-systems to scale, in a longitudinal section. The right-handed coordinate system used in the experiment is also represented.*

## 2.3 Description of the detector

The technique employed to measure the momentum of charged particles and to discriminate them, consists in the reconstruction of the trajectory of the particle inside a magnetic field by means of a tracking system, and in its identification by calorimetric methods and by "time-of-flight" measurements.

A drawing of the longitudinal section of the PAMELA detector is shown in Fig. 2.2. The central component of the instrument is a hollow permanent magnet which, together with a tracking system composed of six planes of silicon sensors, forms a magnetic spectrometer used to determine the rigidity (see Eq. (1.3)) and the charge of particles crossing the magnetic cavity ("*Spectrometer*" in Fig. 2.2). The measure is done through the reconstruction of the trajectory based on the impact points on the tracking planes and the resulting determination of the curvature due to the Lorentz force: the direction of bending of the particle (i.e. the discrimination of the charge sign) is the key method chosen to separate matter from antimatter.

A first set of scintillators ("*Anticoincidence*") composed of four lateral panels surrounding the magnet and one on top of it, which has a hole with a cross section a bit larger than that of the magnetic cavity, forms a device whose signal is used in anticoincidence mode to tag particles entering sideways or somehow outside the acceptance of the tracker. Another group of four scintillator panels are arranged above the spectrometer as shown in Fig. 2.2 and their role is to help in defining the entrance window of the instrument[1]. Each panel is made of a plastic scintillator whose light output is revealed by compact photomultipliers.

[1] A transition-radiation detector (TRD) to be placed above the spectrometer was included in the original design of the experiment: in the course of the detector construction however, it became clear that the time required to build such a complex gas device able to operate in a space environment had proved to be incompatible with the constraining launch schedule of the satellite. After having evaluated the gains and the drawbacks which a further delay of the mission would have implied for the planned scientific program of the experiment, the decision was taken to renounce to the discrimination capabilities which a TRD could have provided (even taking into account the better-than-expected identification performances shown by the calorimeter in beam tests).

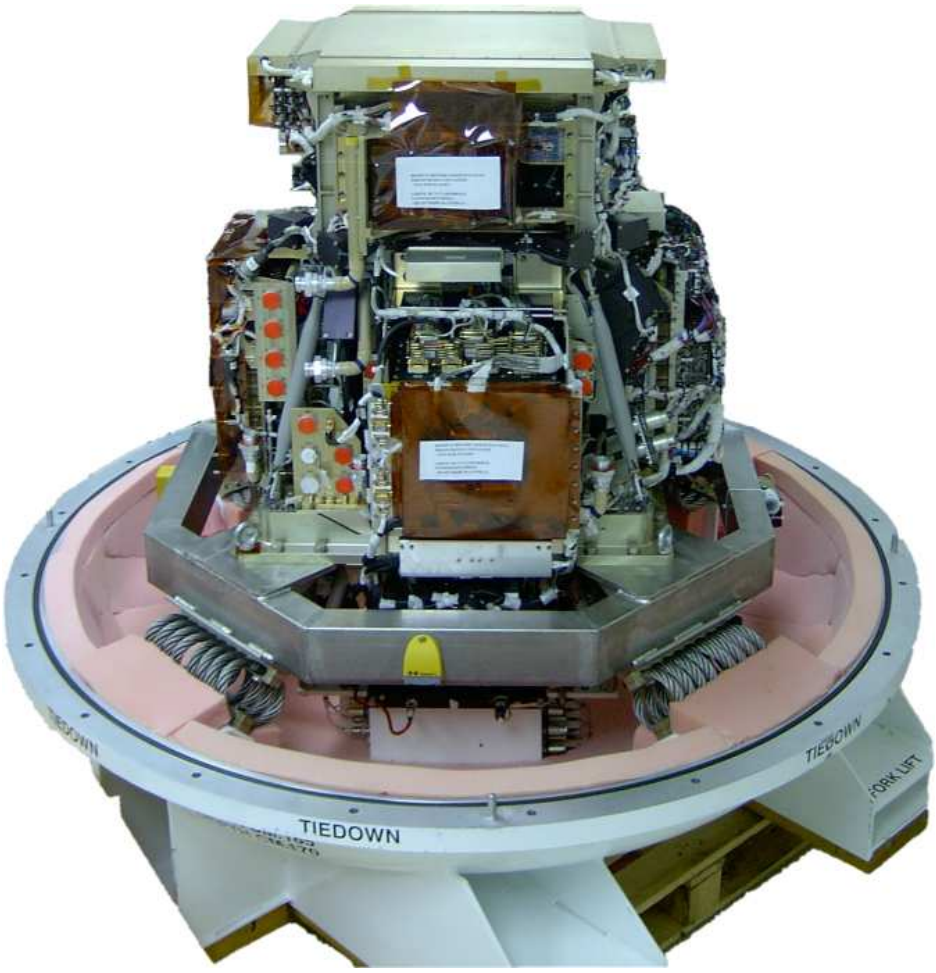


Figure 2.3: *A picture of the PAMELA detector laid on the bottom part of the container which has been used to transport it from Italy to Russia, for the assembling on the satellite. The cabled boxes around the body of the detector contain the electronic boards of the various sub-systems.*

An electromagnetic imaging calorimeter placed under the spectrometer ("*Calorimeter*" in Fig. 2.2) measures the energy of electrons and positrons interacting in its volume, and it is used to identify particles through the analysis of the shape of the shower they produce. The device is composed of alternate layers of silicon strip detectors and tungsten absorbers, and its both longitudinal and transversal fine segmentation allows to distinguish electromagnetically-interacting particles from non-interacting ones and hadrons.

To help the calorimeter in its identification task at low energy, the "*time of flight*" of particles crossing PAMELA can be measured by another system of fast plastic scintillators arranged in three planes ("*TOF*" *S1*, *S2* and *S3* in Fig. 2.2), which can discriminate between positrons (electrons) and protons (antiprotons) for momenta up to about 1 GeV/$c$ by measuring their velocity. The signal provided by this device is also used to produce the main trigger for the experiment, and to determine the arrival direction of particles (downward or upward going). An additional plastic scintillator ("*S4*") is placed under the calorimeter and it is used to reveal charged particles in case a shower is not completely contained in it.

Finally a $^3$He neutron detector ("*Neutron detector*" in Fig. 2.2), located at the bottom of the instrument, gives useful information for the discrimination of electromagnetic and hadronic showers in the calorimeter, being sensitive to neutrons produced in hadronic interactions.

As stated previously in Sec. 2.1, among the main challenges in the construction of the detector there were the mass, size and power limitations imposed by being housed on a satellite. The whole apparatus just described, plus all the additional auxiliary systems and the required electronic boards, has an overall height of about 120 cm, a weight of almost 470 kg and the nominal average required power is 316 W. A picture of the complete instrument is shown in Fig. 2.3.

## 2.4 The magnetic spectrometer

The main information which is used to determine the spectrum of the charged component of cosmic rays is the particle momentum: to obtain

this information in the PAMELA experiment a magnetic spectrometer is employed [51]. This kind of detector measures the *magnetic deflection* of charged particles as they pass through a region where a magnetic field is present. The magnetic deflection (or simply the *deflection*) is defined as the inverse of the particle rigidity $R$ (see Eq. (1.3)):

$$\eta \;=\; \frac{1}{R} \;=\; \frac{q}{p} \tag{2.1}$$

and thus combines the information on the magnitude of the momentum $p$ of the particle and on its charge $q$.

The Lorentz force $\boldsymbol{F}_L$, which is responsible for the curvature of the trajectories of charged particles moving with velocity $\boldsymbol{v}$ in a magnetic field $\boldsymbol{B}$, can be expressed in the International System of Units (SI) as:

$$\boldsymbol{F}_L \;=\; q\,\boldsymbol{v}\times\boldsymbol{B}\;. \tag{2.2}$$

Correspondingly, the relativistic equation of motion for a particle with mass $m$ when it is under the effect of this force is:

$$m\gamma\,\frac{\mathrm{d}^2\boldsymbol{r}}{\mathrm{d}t^2} \;=\; q\left(\frac{\mathrm{d}\boldsymbol{r}}{\mathrm{d}t}\times\boldsymbol{B}\right)\;. \tag{2.3}$$

Introducing the path length $l=\beta ct$ and using $p=m\gamma\beta c$, from Eq. (2.1) it follows that, since $\beta=\frac{v}{c}$ is a constant[2], this equation can be rewritten as:

$$\frac{\mathrm{d}^2\boldsymbol{r}}{\mathrm{d}l^2} \;=\; \frac{q}{m\gamma\beta c}\left(\frac{\mathrm{d}\boldsymbol{r}}{\mathrm{d}l}\times\boldsymbol{B}\right) \;=\; \eta\left(\frac{\mathrm{d}\boldsymbol{r}}{\mathrm{d}l}\times\boldsymbol{B}\right)\;. \tag{2.4}$$

Generally, Eq. (2.4) can be solved by numerical methods for a certain set

[2]Strictly speaking this is true only in vacuum: in the presence of matter, charged particles lose energy (by ionization and possibly by other effects) and consequently $\beta$ is no more constant. Conversely, the Lorentz force does not modify the energy of the particle since it does not do any work, being always perpendicular to the direction of motion.

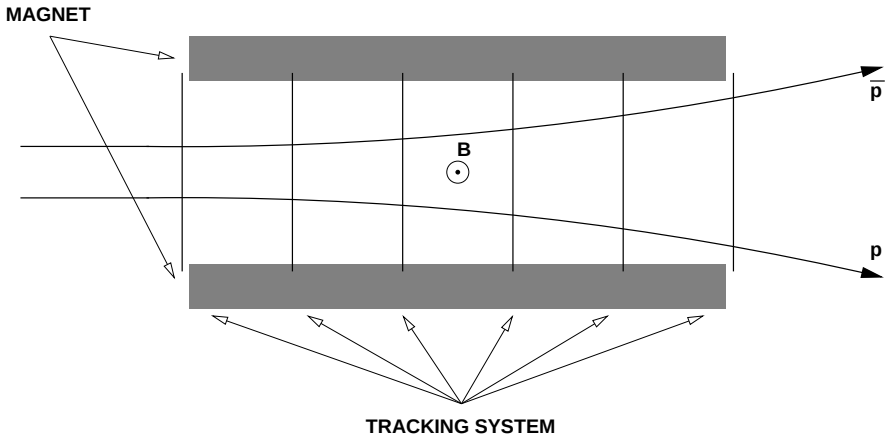


Figure 2.4: *Schematic drawing of a magnetic spectrometer, represented in a longitudinal section. Trajectories of particles with different electric charge sign are bent in opposite ways because of the Lorentz force, as they pass inside a cavity where a nearly uniform magnetic field is present. A tracking system measures the passage of particles while crossing a set of detecting planes.*

of initial conditions, provided that the magnetic field along the trajectory of the particle is known. The deflection $\eta$ of the particle is calculated by looking for the set of initial conditions which results in the curve that best reproduces the track. Once the direction of motion is fixed, the sign of the deflection corresponds to the electric charge sign of the particle, and if its absolute value is also determined the momentum can be calculated.

In the case of a magnetic spectrometer, the reconstruction of the trajectory is obtained starting from the knowledge of the impact points of the particle as it crosses a set of detecting planes which form the tracking system, as depicted in Fig. 2.4. Also the measure of the absolute value of the charge can be done by means of the same tracking system, since the energy deposited by ionization in the sensitive areas of its planes is proportional to the square of the charge of the particle[3].

[3]Also the TOF scintillator system of PAMELA can perform this measurement, as well as provide the needed information on the arrival direction too. This detector will

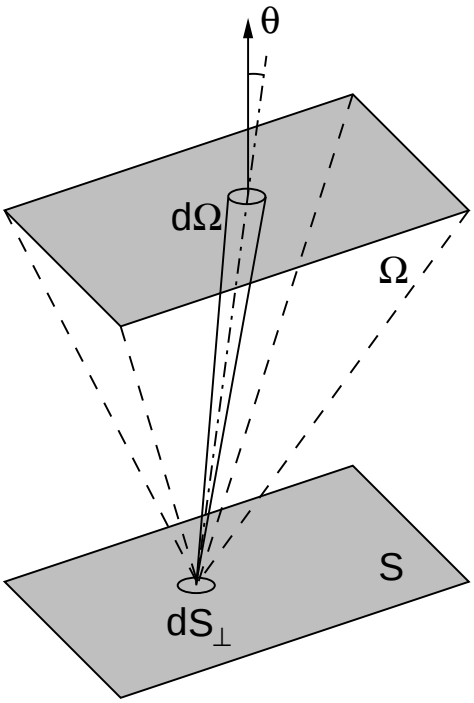


Figure 2.5: *Sketch of the geometry involved in calculating the geometrical factor. Once a detecting surface $S$ is chosen, the solid angle $\Omega$ seen by each of the surface elements $\mathrm{d}S_\perp$ perpendicular to a track with a incidence angle $\theta$ is integrated.*

The position measurement in the spectrometer of PAMELA is performed by six planes of high-resolution silicon microstrip sensors, while the magnetic field needed to bend the particle track is provided by a permanent magnet with a longitudinal cavity. The characteristics of both these components of the detector will be discussed in detail in the next sections. Their dimensions and geometry has been designed in order to get the best compromise in maximizing two conflicting features: the spectrometer bending power, expressed by the so-called *Maximum Detectable Rigidity* ($MDR$), and its acceptance, represented by the *Geometrical fac-*

be described later in Sec. 2.5.2.

*tor* ($G$). The former quantity is defined as the value of the rigidity which corresponds to a 100% uncertainty on its measurement, and thus it is connected to the upper limit of the energy range which the instrument can span. The latter is instead related to the number of particles with a given momentum that can be detected in a certain time interval. $G$ is defined as the factor of proportionality between the detector counting rate and the intensity of an isotropic radiation, and it can be expressed in case of straight tracks of particles as (see Fig. 2.5):

$$G = \int_S \int_\Omega \cos\theta \, \mathrm{d}S \, \mathrm{d}\Omega \, . \tag{2.5}$$

In the above formula $\cos\theta \, \mathrm{d}S = \mathrm{d}S_\perp$ is the element of surface area perpendicular to the direction of motion of the particle (which is defined by the polar coordinates $(\theta, \varphi)$), $\mathrm{d}\Omega = \sin\theta \, \mathrm{d}\theta \, \mathrm{d}\varphi$ is the element of solid angle, and the integration is done on the surface of any of the detecting planes and on the corresponding solid angle which it subtends. While the acceptance grows with the cross section of the cavity, the bending power gets larger as its length and the magnitude of the $\boldsymbol{B}$ field in its volume increase. It is thus clear that these two requirements are in competition in defining the optimal geometry of the instrument: a longer magnetic cavity enhances the $MDR$ while lowering $G$, as on the contrary a wider detecting area makes the acceptance larger but worsens the upper momentum limit because it is more difficult to maintain a high field on a larger area. In the PAMELA experiment, the extension of the measured energy range of the antiproton and positron spectra is a main objective, so the $MDR$ is the feature which has been preferred in designing the spectrometer. With a magnetic cavity which measures $436 \times 132 \times 162$ mm$^3$, a distance of 445 mm between the farthest couple of detecting planes, an average intensity of the $\boldsymbol{B}$ field of 0.43 T and a spatial resolution in the determination of the particle impact point on the tracker planes better than 4 $\mu$m (see Sec. 2.4.1 and 2.4.2 for details), the expected maximum detectable rigidity is about 1 TV/$c$ [52], while the computed geometrical factor for high-energy particles is about 21.5 cm$^2$ sr.

While the upper edge of the measure of the spectrum for particles

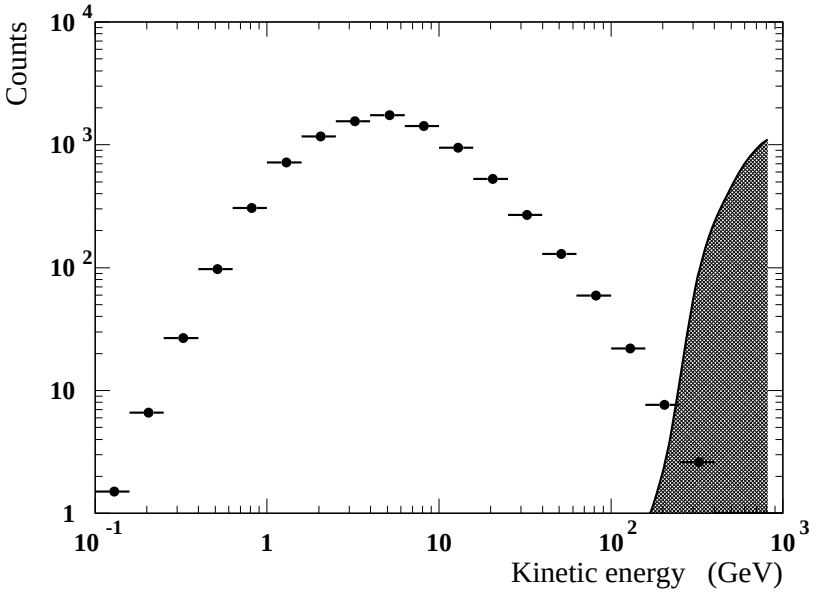


Figure 2.6: *Simulated effect of the proton spillover in the antiproton flux measurement. The points represent the expected number of antiprotons in three years as measured by PAMELA as a function of kinetic energy, in a case of purely secondary production in the interstellar medium according to the* Modified Leaky Box Model. *The shaded area shows the simulated proton spillover in the* $\overline{p}$ *sample.*

like protons or nuclei is directly connected to the $MDR$, for antiprotons, antinuclei and positrons the situation is complicated by their rarity in the cosmic radiation. Indeed, as the energy raises and tracks get closer and closer to a straight line, it becomes increasingly difficult to determine the charge sign, because of the finite resolution of the tracking detector in measuring the impact points: this means that a high-momentum $p$, whose $\eta$ value is therefore positive but very close to zero (see Eq. (2.1)), is statistically subject to be assigned a negative deflection and to be identified as a $\overline{p}$. Since the sign of the electric charge is the primary distinctive element for discriminating between a particle and its antiparticle, and keeping in mind that the number of protons in cosmic rays is far

larger than that of antiprotons (see Fig. 1.5), this misidentification has as a consequence that it is much more likely for protons to be mistaken for their antiparticles than vice versa. This effect, which causes a more abundant population of particles to become a non-negligible background when measuring rarer antiparticles at high energies, is called *spillover*. A simulation of the effect of the $p$ spillover over a sample of secondary $\overline{p}$ is depicted in Fig. 2.6, which shows how, in spite of a much higher maximum detectable rigidity, the detection of antiprotons is limited to about 190 GeV in a likely scenario (the reported $\overline{p}$ flux is obtained in a case of purely secondary production in the interstellar medium according to the *Modified Leaky Box Model*), since above this energy the number of misinterpreted protons becomes comparable with the antiproton signal. Similar considerations can be done for the measurement of the spectrum of positrons and antinuclei, whose upper end is restricted by the background due to the more abundant electrons and nuclei respectively (the limits have been reported in Sec. 2.2).

In case of a uniform magnetic field, from Eq. (2.2) it can be seen that for a particle with charge $q = Ze$, the projection of the track on the plane perpendicular to $\boldsymbol{B}$ (which is usually called the *bending plane*) is a circle whose radius $r$ is approximately related to the momentum intensity $p$ (expressed in GeV/$c$) by:

$$p \, \cos\lambda \, \simeq \, 0.3 \, Z \, B \, r \, , \tag{2.6}$$

where $\lambda$ is the angle between $\boldsymbol{p}$ and the plane. For a magnetic spectrometer the measurement error on $p$ depends substantially on two contribution, whose relative weight changes with the momentum itself. At high energies the main uncertainty comes from the finite spatial resolution $\sigma$ of the tracking detector in measuring the particle impact points on the detecting planes. Defining $k = 1/r$ as the *curvature*, the contribution of this effect to the error on $k$ is approximately constant with $p$ and it varies linearly with the spatial resolution $\sigma$ (see Ref. [9]):

$$\Delta k_{res} \propto \frac{\sigma}{L'^2} \, , \tag{2.7}$$

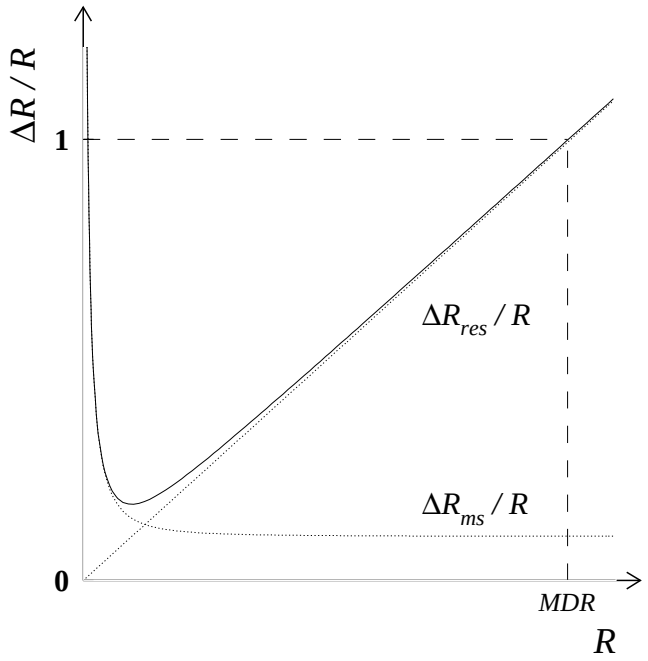


Figure 2.7: *Spectrometer resolution as a function of rigidity. The dotted lines show the rigidity relative error due to the finite spatial resolution $\Delta R_{res}/R$ and the error due to the multiple scattering $\Delta R_{ms}/R$, while the continuous line represents their quadratic sum. The rigidity value corresponding to a 100% uncertainty defines the maximum detectable rigidity.*

where $L'$ is the length of the track when projected on the bending plane. Thus, since from Eq. (2.6):

$$\frac{\Delta p}{p} \;=\; \frac{\Delta k}{k} \;=\; \Delta k \, \frac{p \, \cos\lambda}{0.3 \; Z \; B} \; , \tag{2.8}$$

it follows that:

$$\frac{\Delta p_{res}}{p} \;\propto\; \frac{\sigma}{B \; L'^2} \; p \; . \tag{2.9}$$

This equation not only shows that, as suggested previously in this section, larger values of the intensity $B$ of the field and of the length of the track (i.e. of the magnetic cavity, where the track points are measured) allow a lower $\Delta p/p$ at high energies, which results in a greater $MDR$, but also that a good spatial resolution is needed in order to keep low this error which grows with the momentum. On the contrary for small values of $p$ this contribution approaches zero and the main uncertainty is due to the multiple Coulomb scattering of the particle as it crosses the matter along its path inside the spectrometer. This effect, which is smaller for substances having a larger radiation length $X_0$, can be expressed as [9]:

$$\Delta k_{ms} \simeq \frac{0.016 \text{ GeV}/c}{L\, p\, \beta\, \cos^2\lambda}\, Z \sqrt{\frac{L}{X_0}}\,, \tag{2.10}$$

where $L$ is the track length. Using again Eq. (2.8), this implies that:

$$\frac{\Delta p_{ms}}{p} \propto \frac{1}{\beta} = \sqrt{1 + \left(\frac{m\, c^2}{p\, c}\right)^2}\,, \tag{2.11}$$

which approaches a constant value as $p$ increases. In Fig. 2.7 the relative error on rigidity $\Delta R/R = \Delta p/p$ (see Eq. (2.1)) as a function of $R$ is shown, and the two contributions coming from the finite spatial resolution and from the multiple scattering are indicated, as well as the value of the $MDR$. To summarize the consequences of Eq. (2.9) and (2.11), the approach which needs to be adopted in order to enhance the momentum resolution and stretch the measurement range as far as possible, consists in using a spectrometer with a long magnetic cavity in which a high field is present, and whose tracking system provides a good spatial resolution while having a minimal amount of material along the path of the particles. The next sections 2.4.1 and 2.4.2 describe how these requirements have been complied with in designing and building the magnetic spectrometer of the PAMELA experiment.

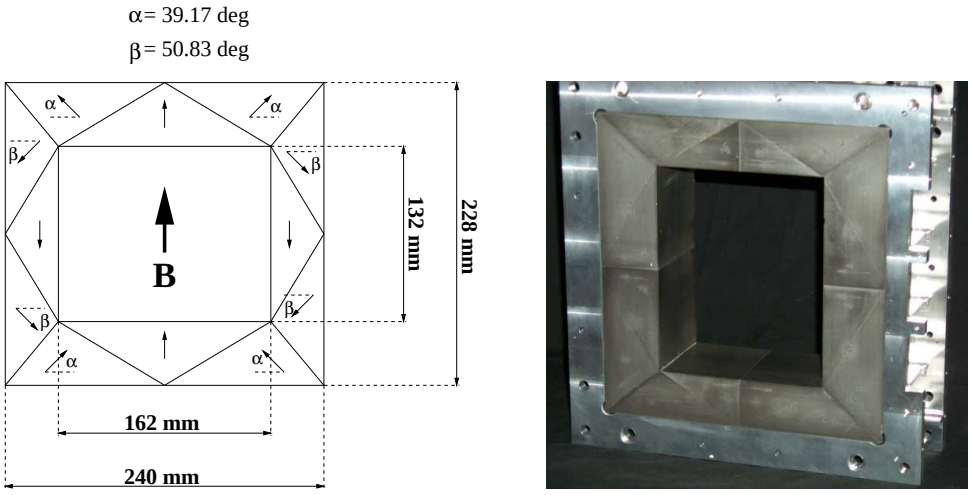


Figure 2.8: *One of the magnetic modules of the spectrometer: on the left, a drawing of the yokeless configuration, which shows the direction of the residual induction and the resulting* $\boldsymbol{B}$ *field vector in the cavity; on the right, a picture of a prototype of the magnetic modules surrounded by its aluminium frame.*

### 2.4.1 The magnet

The magnetic field of the spectrometer of PAMELA is generated by a permanent magnet composed of five identical modules put one on top of another to form a tower, which is 436 mm high. The detecting planes of the tracking system are housed in slits, measuring 9 mm, located between each couple of modules, as well as at the top and at the bottom of the structure (as represented in the sketch of Fig. 2.4). The magnetic substance that the five elements are made of is a Nd-Fe-B alloy, which provides a high residual induction of 1.32 T $\pm$ 0.03 T. Small blocks of this sintered alloy, in the shape of triangular prisms, are glued together according to a suitable geometry to form a module whose dimensions are $228 \times 240 \times 80$ mm$^3$ and which has a cavity that measures $132 \times 162$ mm$^2$, and then they are enclosed in a nonmagnetic aluminium case, as shown in Fig. 2.8. This *yokeless* magnetic configuration, which allows the field lines

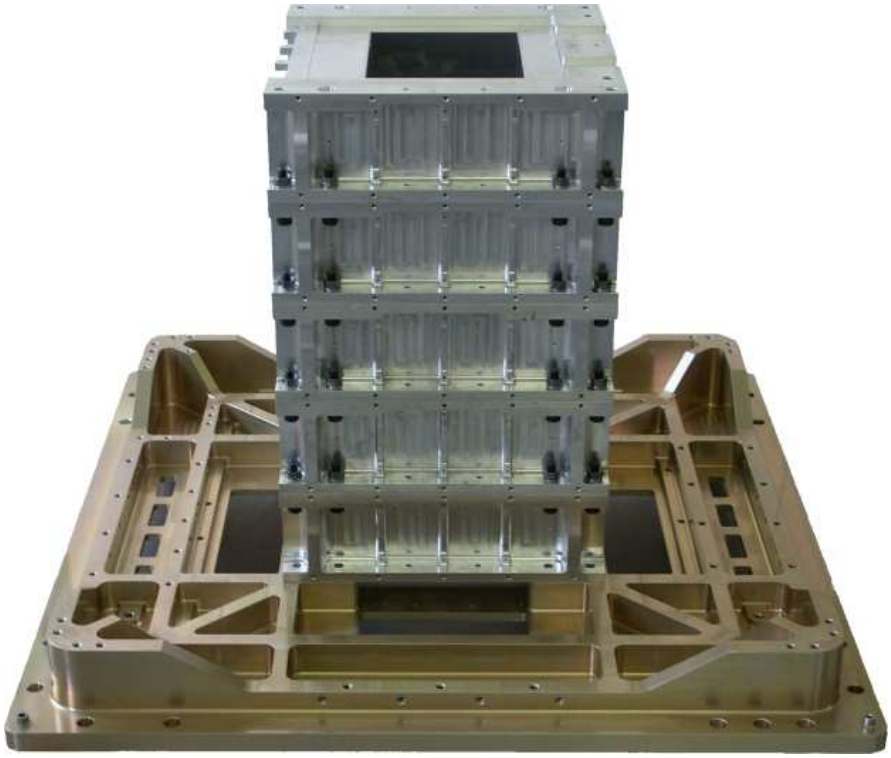

Figure 2.9: *The permanent magnet of the spectrometer, composed of five modules encased in their aluminium frame. The tower is mounted over the base plate which connects PAMELA to the satellite structure. On top of it the upper opening of the magnetic cavity can be seen.*

to close inside the magnet without using any additional iron structure, has been studied in order to optimize the uniformity and the intensity of $\boldsymbol{B}$ inside the cavity (as suggested in Ref. [53]). A picture of the whole structure is shown in Fig. 2.9. Ferromagnetic screens (not shown in the figure), with a thickness of 2 mm, are placed around the tower at a distance of 8 mm, and they ensure that the external stray field is lower than the limit required for the safe working of the satellite, and for the correct functioning of the other parts of the PAMELA instrument (in particular of the photomultipliers used to detect the light output of the scintillators).

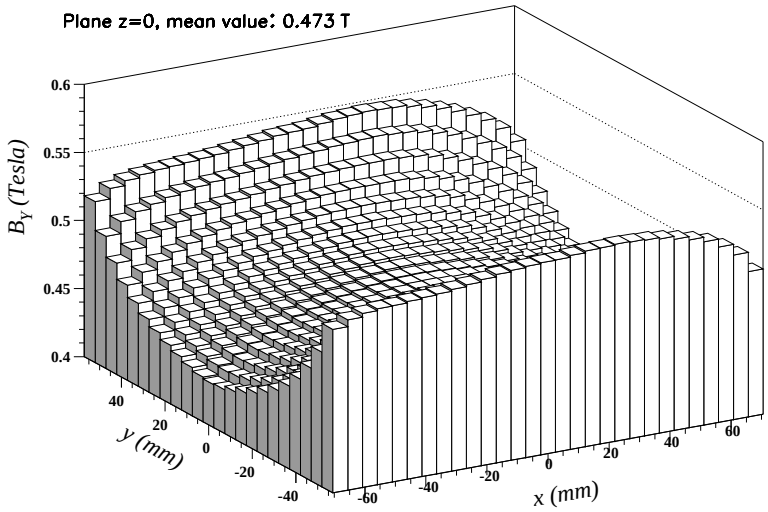


Figure 2.10: *Measured values of the main component of the magnetic field over the cross section going through the center of the cavity (plane $z = 0$).*

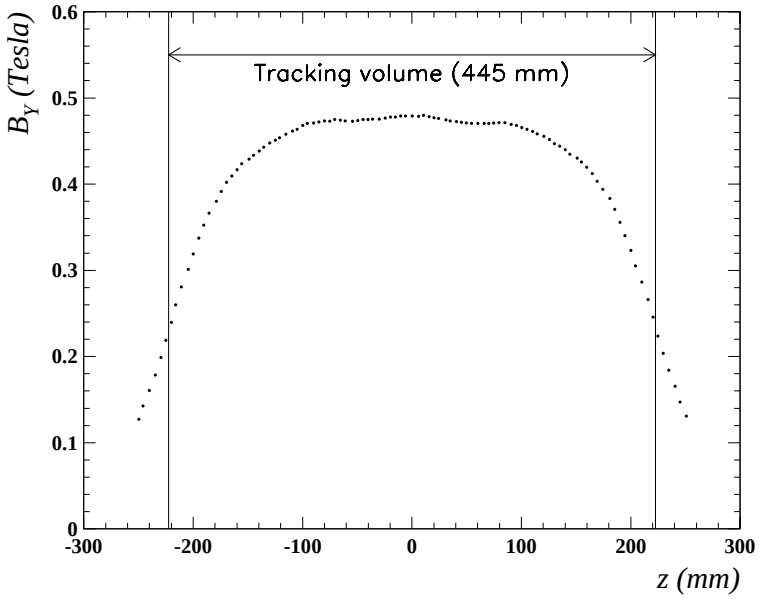


Figure 2.11: *Measured values of the main component of the magnetic field along the longitudinal axis going through the center of the cavity (axis $x = y = 0$).*

The resulting $\boldsymbol{B}$ field in the spectrometer is almost uniform, and it mainly points opposite to the direction chosen as the Y axis of the reference frame of PAMELA (see Fig. 2.2), while the Z axis is directed along the cavity and points to the S1 plane of the TOF system, and the X axis is obtained as a consequence in order to get a set of right-handed coordinates. The origin of the coordinate system is located at the geometrical center of the magnet. Since the prevalent direction of motion of cosmic-ray particles is along Z, the Lorentz force causes their trajectory to curve mostly in the X direction, so that the bending plane is identified by the X and Z axes. The magnetic field has been measured by sampling its $B_{\mathrm{X}}$, $B_{\mathrm{Y}}$ and $B_{\mathrm{Z}}$ components on a three-dimensional grid consisting of 67 367 points, 5 mm apart along the three axes, by means of a Hall probe mounted on the moving mechanical arm of an automated precision positioning system. Some of the results which have been obtained are displayed in Fig. 2.10 and 2.11: they show the shape of the $B_{\mathrm{Y}}$ component of the field, which is the main one, on the plane $z = 0$ and along the axis $x = y = 0$, respectively. The average value of the field over the whole volume of the cavity is about 0.43 T.

Nine Hall probes are placed on the external sides of the magnetic tower in order to monitor the magnetic field during the course of the mission, and be aware of possible alterations of its configuration.

### 2.4.2 The silicon tracking system

The detecting areas of the tracking system of PAMELA consist of six planes of silicon sensors, evenly spaced along the cavity of the magnet, as shown in Fig. 2.2 and Fig. 2.4. Each plane contains three independent elementary parts, called *ladders*, glued together side by side and fastened within an aluminium frame (see Fig. 2.12). The frames are then inserted in the slits between the magnetic modules and at both the ends of the spectrometer, in such a way that the distance between them is 89 mm and the length of the tracking volume is 445 mm. The *ladder* is the basic detecting unit of PAMELA's tracker, and it is composed by a couple of silicon sensors joined together and by an $Al_2O_3$ *hybrid circuit* which contains the front-end electronics. Each sensor has a surface of

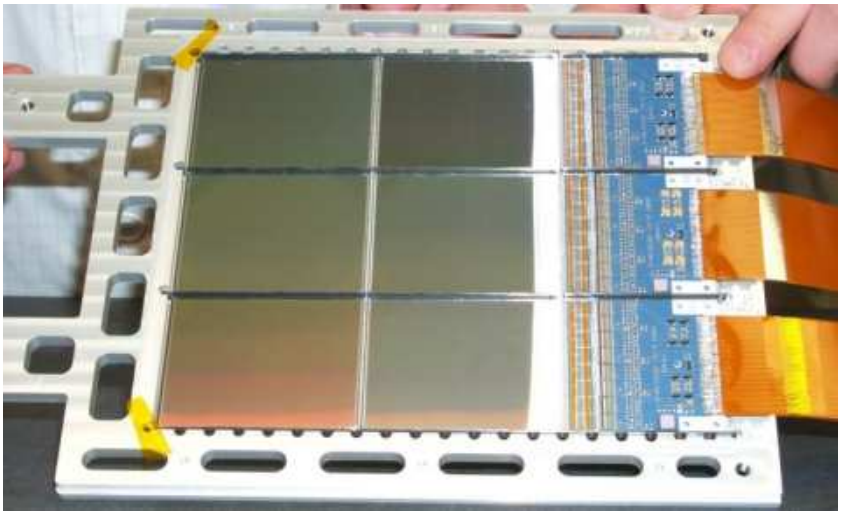

Figure 2.12: *A plane of the tracking system, composed of six silicon sensors and their front-end electronics, fixed to an aluminium frame to be inserted in the magnetic structure.*

$53.33 \times 70.00\ \mathrm{mm}^2$ and is 300 $\mu$m thick. Four thin carbon-fiber bars, glued at the sides of the *ladders*, help in strengthening the mechanical structure of the plane, and they also provide the binding points of the sensors to the frame. This detector set-up is remarkable since it allows to place the detecting planes inside the magnetic field of the spectrometer without any additional structure to support them. Indeed the *ladders* are attached to the magnet just by their edges and they stay hanging inside the cavity, thus minimizing the amount of matter which particles have to cross on their path. In this way the ionization energy loss of particles is kept low, and the multiple scattering, which is the main cause of the momentum resolution worsening at low energies (as explained in Sec. 2.4), is reduced too.

### 2.4.3 The silicon microstrip detectors

The detectors which have been employed in PAMELA's spectrometer are silicon microstrip sensors. The basic working principle of this kind of

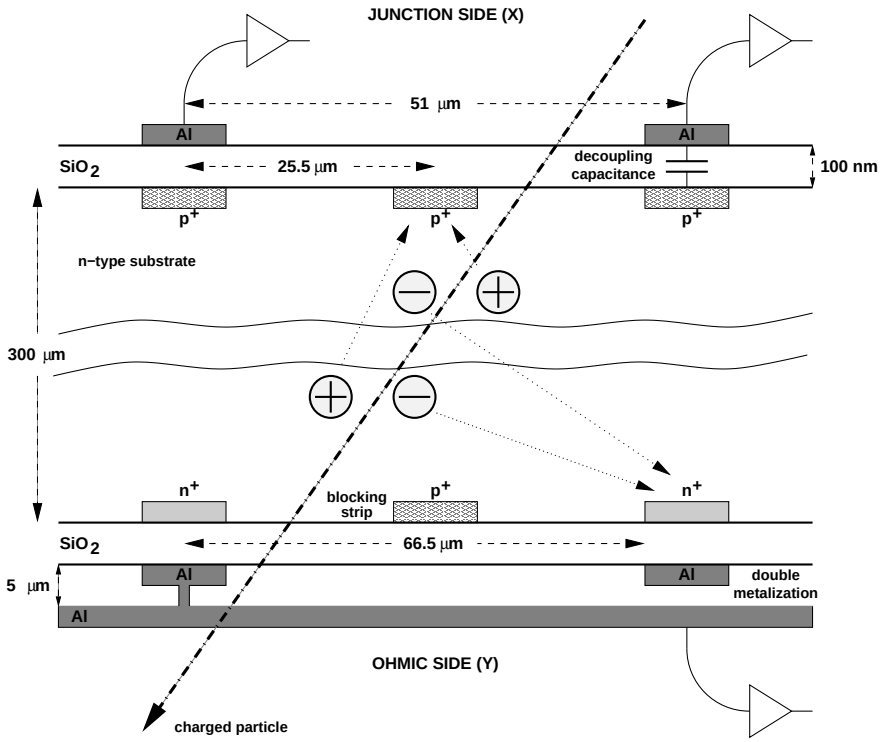


Figure 2.13: *Schematic representation of a silicon sensor of the tracking system. The upper half shows a cross section of the junction side ($p^+$-$n$) while the lower half represents the ohmic side (rotated by 90° for the sake of clarity). When a charged particle passes through the sensitive volume electrons and holes produced by ionization and collected by the strips induce a signal on the aluminium electrodes.*

detectors exploits the properties of the junction between a couple of semiconductors. If the two metals are doped oppositely (in such a way that electrons and holes are the main free charge carriers, respectively) and a reverse bias voltage is applied to them, a region in which no free charges are present is created around the junction (*reverse-biased p-n junction*). The electric field generated in that zone causes any free charge being present there (in particular the charge released by ionizing radiations crossing it) to migrate towards the electrodes applied to the two semi-

conductors and to be collected by them. From the amount of ionization which is produced a measure of the charge $Z$ of the incident particle can be obtained. By the choice of a suitable geometry it is possible to extract from such type of detector the spatial information about the impact point of incident particles. In fact, if the junction is built implanting thin segments of $p^+$-type semiconductor, in shape of narrow strips, upon a planar n-type substrate, a measure of the coordinate of the impact point on the plane in the direction perpendicular to the strips can be done looking at which of them has collected the charge produced in the sensitive substrate. If the implantation pitch $P$ is small enough (microstrip sensors) a very good spatial resolution can be achieved ($\sigma \sim P/n$, where $n = 3 \div 7$, for typical devices), and this is the reason why this kind of detectors have been chosen for the spectrometer of PAMELA.

The sensors which have been built for the tracking system are able to measure both the coordinates of the impact point on their surface, since they have two sets of silicon strips implanted, perpendicularly to each other, on both the sides of the n-type substrate (*double-sided* detector). In this way the full spatial information can be obtained from a single detecting layer, thus reducing the quantity of matter on the trajectory of particles. With reference to Fig. 2.13, on one of the sides of the n-type substrate, which is 300 $\mu$m thick, 2035 $p^+$ strips are implanted with a pitch of 25.5 $\mu$m (*junction side*), while on the other one (*ohmic side*) they are $n^+$ doped, 1024 in number and 66.5 $\mu$m apart. On the ohmic side, an additional $p^+$ blocking strip is placed in between every two strips in order to increase the interstrip resistance [54]. The spatial orientation of the sensors inside the spectrometer is such that the strips belonging to the junction side run parallel to the Y axis, thus being used to measure the X coordinate, which is the main bending direction in the magnetic field. On the contrary the ohmic-side strips determine the Y coordinate of the particle impact point. A 100 nm thick silicon-dioxide layer covers both the faces of the sensor and keeps the implanted strips separated from the aluminium electrodes that is used to read out the collected charge. This insulation acts as an integrated decoupling capacitor, thus preventing the dark current from being integrated. Indeed not all the strips which are implanted on the junction side are connected to the read-out

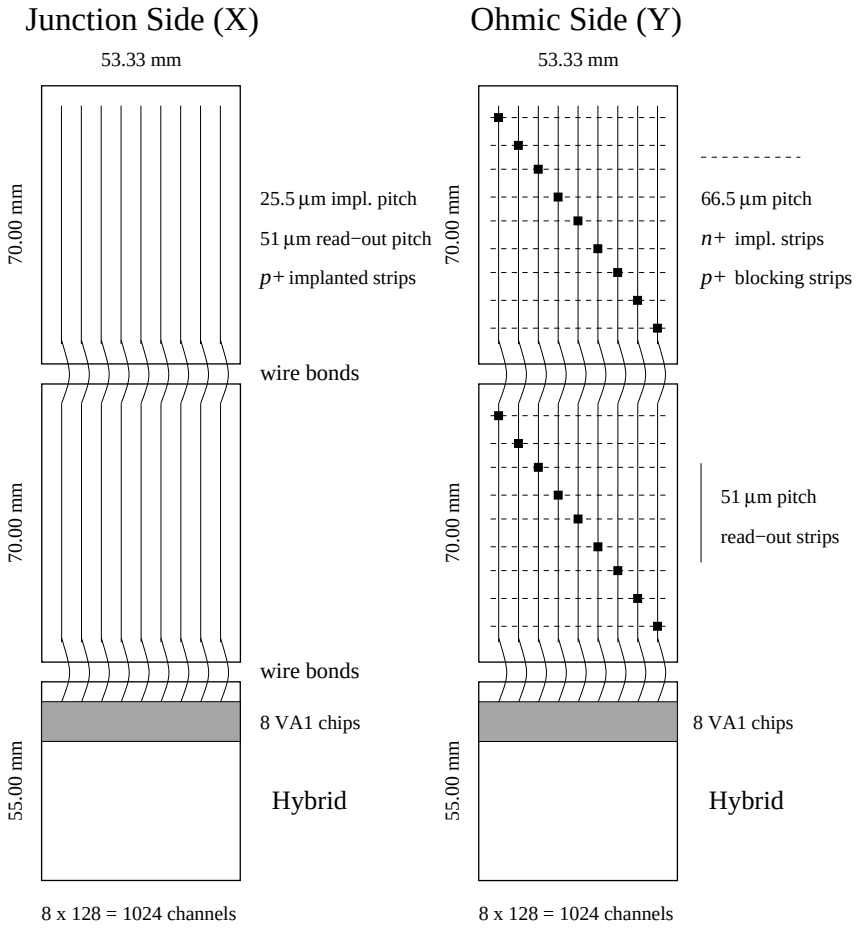


Figure 2.14: *Sketch of the strip layout on the two sides of a* ladder *of the tracking system. On the ohmic side the second layer of read-out electrodes perpendicular to the $n^+$ strips, and their connections on the diagonal of the sensor are both shown.*

channels, but one out of two is not (the unconnected implantations are called "*floating*" strips), so that the actual reading pitch is 51 $\mu$m. On the ohmic side an additional 5 $\mu$m thick $SiO_2$ layer covers the aluminium depositions: a second set of metallic electrodes is created on top of it, perpendicularly to the first one (*double metallization*), and the strips of the two sets are electrically connected one-to-one by means of small holes etched in the silicon-dioxide layer along the diagonal of each sensor, as shown schematically in Fig. 2.14. This technical solution makes the actual read-out strips run parallel on both the junction and the ohmic side, and it allows their front-end electronics to be placed on the same edge of the sensor (on the two faces of a single hybrid), thus simplifying the geometry and the mechanical structure of the device. The read-out strips of the two of sensors forming a *ladder* are connected together by means of wire bonds and they are handled by the same front-end circuitry: a drawback of this configuration is that on the Y side the couple of corresponding strips, which are implanted 7 cm apart on the two sensors, are read by the same electronic channel. This introduces an ambiguity in the determination of the Y coordinate (a signal appearing on a certain Y channel could have been generated by a particle hitting any of the two corresponding strips on the two sensors), which however can be solved during the data analysis procedure by comparing the position measured on a certain plane with that found on the other planes of the tracking system, or even using the spatial information coming from other detectors, such as the TOF or the calorimeter (see Sec. 3.5.1 for details).

For the front-end electronics, the VA1 chip is used [55], which consists of 128 parallel sections, each one composed of an amplifier, a shaper and a sample-and-hold stage, in series with a multiplexer controlled by a shift register. On each *ladder* side 8 VA1 chips are present, so that the number of electronic channels is 128 (channels) $\times$ 8 (chips) $\times$ 3 (*ladders*) = 3072 for each side of a plane, and 3072 (channels) $\times$ 2 (sides) $\times$ 6 (planes) = 36 864 for the whole tracker. The analog output of the front-end electronics of each *ladder* side is sent to an external board by means of a kapton cable (such cables can be seen in Fig. 2.12, on the right side), and there a 12-bit Analog-to-Digital Converter (ADC) digitizes it. Subsequently, a Digital Signal Processor (DSP) for each side of the tracker planes per-

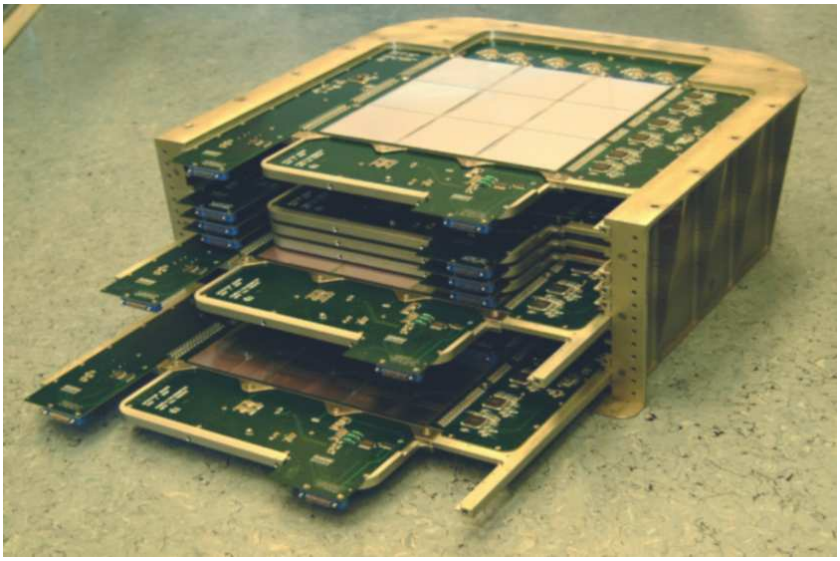

Figure 2.15: *The electromagnetic imaging calorimeter, with some of the detecting modules partially inserted.*

forms data compression and calibration, and manages the sending of the data stream to the main CPU (Central Processing Unit) of the experiment for temporary storing. Finally, spectrometer data are delivered, together with those of the other detectors, to the satellite communication system, which transmits them to the receiving station on Earth by a radio link. Some details about the acquisition process and the structure of spectrometer data are reported in Sec. 3.1.

## 2.5 The other detectors in PAMELA

### 2.5.1 The calorimeter

Once the particle charge separation has been performed by the spectrometer, the main background in the identification of antiprotons and positrons in cosmic rays consists of electrons and protons, respectively. In order to cope with this discrimination task, the electromagnetic imaging calorimeter of PAMELA is used. The detector [56], which is shown in

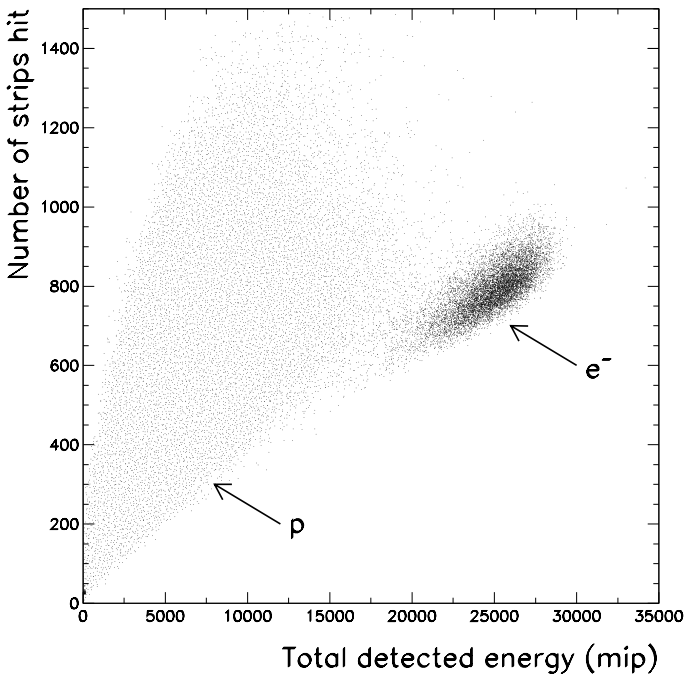


Figure 2.16: *Discrimination capability of the calorimeter between protons and electrons, on the basis of the number of strips involved in the shower and of the total energy released. Data refer to particles with a momentum of 200 GeV/c acquired on a beam test at the CERN SPS facility in 2002.*

Fig. 2.15, is composed of 22 detecting modules inserted in an aluminium frame which is 180 mm high. Each module consists of two layers of silicon sensors which have a 2.6 mm thick tungsten absorber in between. The sensors measure $80 \times 80$ mm$^2$ and are 380 $\mu$m thick: nine of them form a detecting layer, which has an area of $240 \times 240$ mm$^2$. Their working principle is similar to that described above in Sec. 2.4.3 for the detectors of the tracking system but, since these are single-sided devices, two sections are needed in each module in order to measure both the coordinates of the particle impact point. The spatial information is obtained thanks to the implantation of 32 strips, 2.4 mm apart, on the surface of sensors.

When entering the calorimeter, high-energy electrons and positrons

interact with the thick W absorber producing bremsstrahlung photons, which in turn create $e^+e^-$ pairs with lower energy, and so on: the shower which is in this way generated can be studied by measuring the energy released at different depths inside the calorimeter and by reconstructing its shape on the basis of the spatial information on the hit strips. As a whole, the high-$Z$ material used as absorber corresponds to about 16.3 radiation lengths and 0.6 interaction lengths: this assures that most of electrons and positrons produce a shower in the first layers, while the interaction probability remains low for hadrons. Thus in the case of $e^+$ and $e^-$ the destructive interaction allows a measurement of the energy of the incoming particle. Results of the analysis of data taken during test sessions on particle beams at CERN show that a resolution of about 5.5% in the energy range $20 \div 200$ GeV can be obtained. In spite of the compactness of the device, from the topological study of the energy distribution of the shower, which is allowed by the fine granularity in both the longitudinal and transversal directions, particle identification can be performed. Combining all the information on the shape and on the energy release of the shower, a rejection factor better than $10^4$ for protons and electrons at 95% selection efficiency in positron and antiproton measurements, respectively, can be achieved in the energy range of PAMELA. As an example of the variables which can be used to discriminate among different particles, the number of hit strips versus the total energy release of the event are plotted in Fig. 2.16 for test beam data. Another characteristic of the PAMELA calorimeter is its possibility to operate in a self-trigger mode, that is to say to perform a stand-alone detection of electrons and positrons. Not being limited anymore by the geometric constraints on the particle track due to the TOF and the spectrometer, the acceptance of the detector while using this hardware feature increases to 470 cm$^2$ sr, and this allows to measure the spectrum of electrons and positrons up to 2 TeV with an estimated energy resolution of about 12% up to 800 GeV.

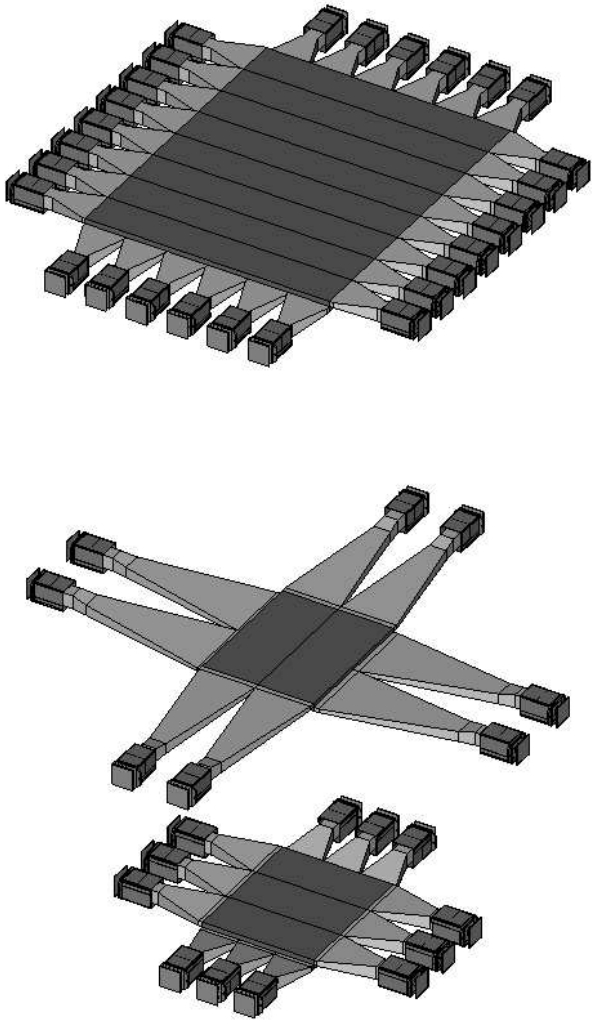

Figure 2.17: *Drawing of the time-of-flight system: from top to bottom, the S1, S2 and S3 scintillator planes with their light guides and photomultipliers.*

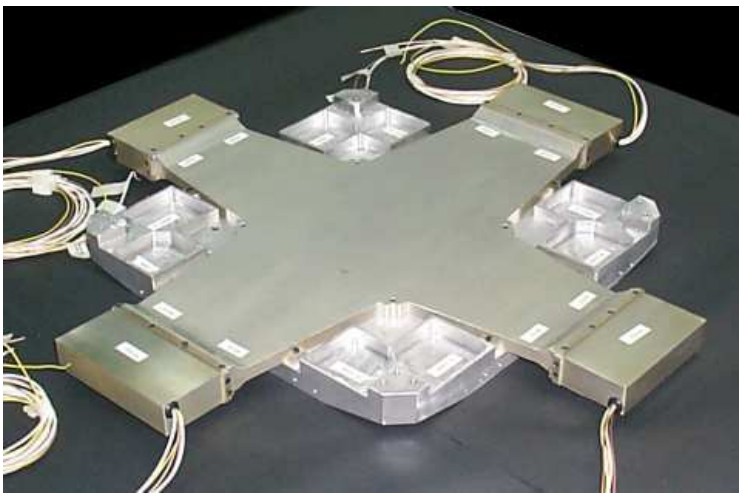

Figure 2.18: *The S2 plane of the time-of-flight system in its aluminium box.*

### 2.5.2 The time-of-flight system and the S4 scintillator

Not all the particles gathered by the PAMELA instrument can be used to obtain useful physical information. In particular, particles other than electrons and positrons (for which the calorimeter self-trigger mode can be exploited, as explained at the end of Sec. 2.5.1) have to pass through the spectrometer detecting planes to be able to determine their momentum. The decision whether the signals coming from the various detectors in PAMELA have to be recorded or not for a certain event is taken on the basis of the information provided by a set of scintillators which form the time-of-flight system of the experiment: in this way most of the particles not entering the acceptance of the spectrometer are discarded. The device [57] is composed of three detecting planes named S1, S2 and S3 which are placed on top of the instrument, above the spectrometer and just below it, respectively (see Fig. 2.2 and Fig. 2.17): their sensitive areas are $330 \times 408$ mm$^2$ for S1 and $150 \times 180$ mm$^2$ for S2 and S3. Two distinct layers of Bicron BC-404 scintillator are put together to form a plane: each of them is segmented into strips (8 and 6 for the layers of

the first plane, 2 for those of the second plane, and 3 for the third one) which are oriented perpendicularly inside the pair of layers, in order to provide a rough estimate of the coordinates of the impact point, and which are read by a couple of photomultipliers at their opposite ends. The thickness of each layer is 7 mm for S1 and S3, and 5 mm for S2. A picture of the S2 plane can be seen in Fig. 2.18.

The fast pulses arising from these plastic scintillators when they are crossed by a cosmic ray are used to generate the signal which triggers the starting of the acquisition procedure of the other detectors in PAMELA. The main trigger configuration for the experiment consists in requiring the presence of a signal in at least one of the two layers of each of the three TOF planes (i.e. the logical AND of the results of the OR between the layers of each plane). Moreover, this system is able to establish what direction the particle is coming from, by looking at the order in which the scintillator have been hit. This is of fundamental importance when trying to identify antiparticles in cosmic rays, since a particle entering the spectrometer from below (the so-called *albedo* particles) could in principle reproduce the same behavior in the magnetic field of its own antiparticle coming from above: as stated in Sec. 2.4, the sign of the magnetic deflection determines the charge only if the direction of motion is known, since the energy loss is negligible and the curvature is consequently constant. Other tasks of this device consist in measuring the charge absolute value and the velocity of incoming particles: the former is accomplished in the same fashion as for the tracking system, by detecting the amount of ionization in the six scintillator layers, while the latter is calculated from the time which is needed by the cosmic ray to cover the distance between S1 and S3. A time resolution of about 300 ps has been measured for the TOF system using cosmic-ray data acquired on ground. Fig. 2.19 shows the results of such $\beta$ measurements on 24 000 events, combined with the rigidity information coming from the spectrometer. On the $\beta$-$p$ plane, particles follow the law:

$$\beta = \frac{1}{\sqrt{1 + \left(\frac{m\,c^2}{p\,c}\right)^2}}\,, \tag{2.12}$$

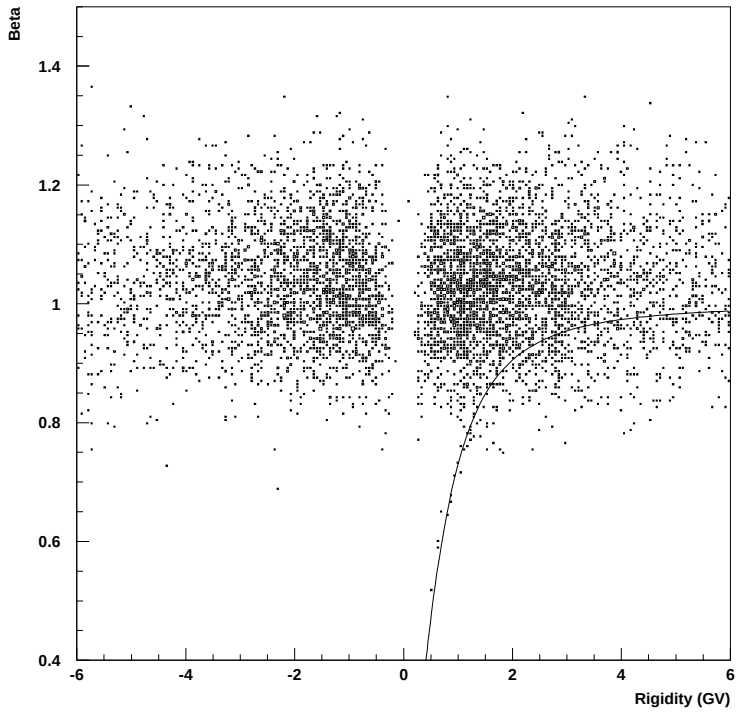


Figure 2.19: *Discrimination capability of the time-of-flight system. The measured velocity $\beta = L/c \cdot 1/t$ (where $L$ is the distance between the TOF planes employed in the measurement, and $t$ is the flight time) is plotted against the particle rigidity $R$ as measured by the spectrometer for a sample of cosmic rays at ground level. While most of the detected particles are muons, few protons can be identified as the point lying near the plotted curve, which shows their expected $\beta(R)$ relation.*

which is superimposed on the scatter plot for the case $m = 0.938$ GeV/$c^2$. The sample contains mostly positive and negative muons, and few protons which can be identified as the points lying near the curve: in flight it will be possible to mass resolve in a similar way protons (antiprotons) from positrons (electrons) for momenta up to about 1 GeV/$c$.

Another separate plastic scintillator, which is not included in the

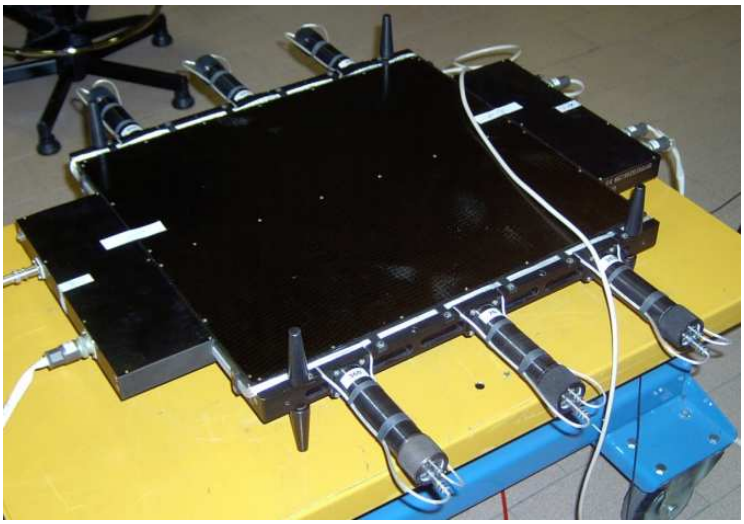

Figure 2.20: *The S4 scintillator in the black wrapping which protects it from external light. The six photomultipliers reading the light output can be seen on two opposite edges, while the boxes attached to the other two edges house the electronic read-out boards.*

time-of-flight measurement system, is placed below the calorimeter (see Fig. 2.20). It measures $482 \times 482 \times 10$ mm$^3$ and is made of a single piece of polystyrene. Its light output is read by six photomultipliers and it is used to detect the charged component of the shower which can possibly escape the calorimeter in case of very high-energy incident particles.

### 2.5.3 The anticoincidence system

Even when the TOF system states that an event has given a signal which fulfills the trigger conditions, this does not necessarily mean that it corresponds to a good particle event. In fact, particle interactions with the material around the instrument or with the instrument itself can occur, reproducing in the TOF the signal which a single down-going cosmic ray could give (as explained in Fig. 2.21). Indeed, simulations [58] have shown that in space about 75% of triggers are actually expected to be "false", that is to say due to coincidental energy releases in the TOF

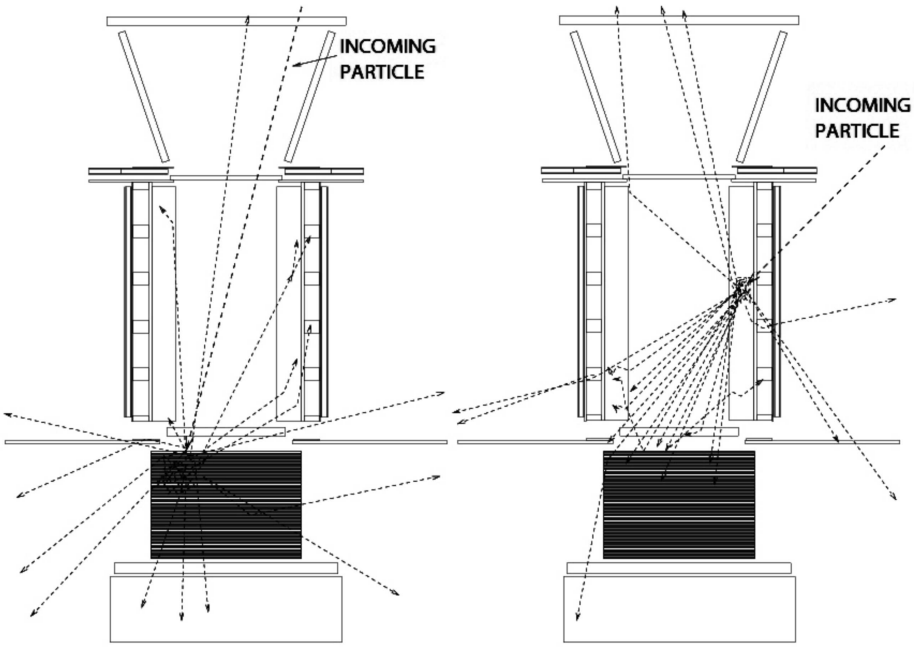


Figure 2.21: *Simulation of proton interactions in the detectors. On the left, the incoming particle enters cleanly the acceptance of the instrument and crosses the three TOF planes generating a good trigger without activity in the anticoincidence scintillators; on the right, a cosmic ray enters the magnetic cavity from one side and gives rise to a shower of secondary particles that induce a false trigger: the signal in the side anticoincidence detector allows to reject this event.*

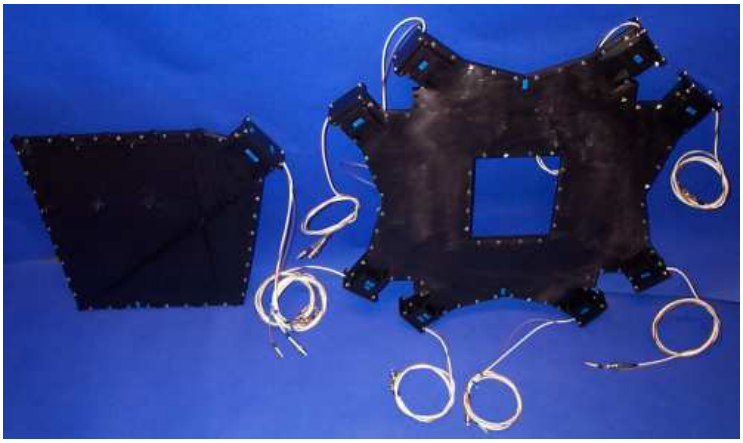

Figure 2.22: *The anticoincidence system: one of the panels which surround the spectrometer is shown on the left, while the panel on top of it is shown on the right. The scintillators are enveloped in an opaque wrapping to prevent outside light from reaching them.*

scintillators by secondary particles generated by cosmic-ray interactions in the mechanical structure of the experiment. In order to recognize this kind of events and to exclude them during the *offline* data analysis (i.e. not at acquisition time), PAMELA is equipped with an anticoincidence system [59]. The spectrometer is shielded from side-entering particles by four scintillator panels surrounding it, which have an almost rectangular shape and an area of about $400 \times 388$ mm$^2$, while a star-shaped panel with a rectangular opening of about $216 \times 180$ mm$^2$ is placed on top of the magnet and is used to tag cosmic rays which enter from above but outside the cavity: in Fig. 2.22 one of the side anticoincidence shields and the top one are shown. Another set of four panels covers the sides of the particle entrance window between the S1 and S2 planes, as shown in Fig. 2.2. The material which has been used for these detectors is Bicron BC-448M, and all of them are 8 mm thick. A Light-Emitting Diode (LED) system is used to calibrate and monitor the scintillator performances during flight. The information about whether a section of the anticoincidence detector is hit is recorded in a time window, 1.28 $\mu$s long, centered on the moment in which the trigger signal has been generated.

Figure 2.23: *The neutron detector during the test and assembly phase. Some of the $^3$He tubes, the polyethylene moderator and the electronic boards are visible.*

The hit time can be located within this interval with an accuracy of about 80 ns.

### 2.5.4 The neutron detector

At the bottom of the whole PAMELA instrument a neutron detector is present, which is used to measure the neutron yield in case of hadron-initiated showers in the calorimeter, thus increasing its particle discrimination capabilities. The device is composed of 36 gas proportional tubes filled with $^3$He and surrounded by a polyethylene moderator and by a cadmium foil (see Fig. 2.23). They are stacked in two planes and cover an area of about $600 \times 550$ mm$^2$. The working principle of this detector exploits the properties of the hydrogen-rich polyethylene moderator to slow down neutrons till their energy is low enough for them to have a non-negligible capture cross section when interacting with the gaseous $^3$He in the counters. In the nuclear reaction a proton and a $^3$H nucleus are produced, and they can be detected as charged particles

through their ionization in the gas. By measuring the neutron yield in the shower, the expected proton rejection factor at 50 GeV is about 10, and its value increases with energy.

## 2.6 Status of the experiment

In order to build such a complex detector for high-energy physics as PAMELA and install it on a satellite, many technical requirements had to be fulfilled. Besides the acquisition tests on particle beams which in the last years have been performed on the detectors in order to fully understand and optimize their physical capabilities, the various devices had to go also through several space qualification tests before the final instrument was ready. The resistance of the structure of the instrument has been investigated, having a mechanical mock-up of PAMELA undergo vibration and shock acceleration tests. In this way the different dynamic conditions that the real detector is going to encounter have been simulated, such as the transportation to the launch site, the take-off of the rocket, the flight of the satellite and the orbital procedures. Moreover, this reproduction of the structure has been used to check the thermal environment which the instrument will endure, and its heat dissipation capabilities. The faultless functioning of the electric components and their correct interaction with the systems of the Resurs DK1 satellite have been instead checked thanks to another mock-up of the instrument, which represents the real flight model as regards all the electric boards, the wirings, the connectors and the interfaces with the spacecraft.

All the detectors which actually form PAMELA were brought to Rome in 2004 for the flight model integration. There, in the first months of 2005, data acquisition, transmission, and all the other software procedures were tested by gathering cosmic rays for the first time with the complete instrument. In March 2005, PAMELA was sent to TsSKB-Progress in Samara, where it underwent the final compatibility checks and was integrated with the satellite at the end of 2005. At the beginning of 2006 it will be carried to the Baykonur cosmodrome for the integration on the rocket and its launch.

# Chapter 3

# Spectrometer data-reduction procedures

*In this chapter the procedures for the data reduction of PAMELA's spectrometer are presented. The software that has been developed consists in a series of routines, which allow to elaborate data coming from the silicon detectors and extract from them first the spatial information about the particle impact points, then the value of the magnetic deflection of particles. Most of the algorithms have been coded in FORTRAN but also C and C++ languages have been used; several external routines from the CERN software libraries such as HBOOK data structures or PAW tools have been employed [60], and also the ROOT package [61].*

*In Sec. 3.1 a brief introduction to some of the aspects of the acquisition procedure can be found, and the characteristics of the spectrometer data and their compression algorithm are described, as well as the calibrations performed during data taking. The offline data reduction is then presented in the following Sec. 3.2 ÷ 3.5.3, which contain the detailed discussion of the steps needed to read data, identify for each event the correct impact points on the detecting planes, and determine the particle deflection.*

*Different portions of the software had been developed to analyze data of tests on particle beams performed during last years on prototypes of the detector: all this code has been in part or completely reorganized and optimized in order to obtain the final version that will be used in a data*

*processing framework common to all the detectors of PAMELA for the analysis of flight data.*

## 3.1 Data acquisition and calibration

The final information provided as output by the electronic chain of the tracking system, as indicated in Sec. 2.4.3, is the digitized value of the voltage level, which results from the integration of the charge collected by each of the 36 864 strips of the silicon sensors when an event fulfills the trigger conditions. Each DSP of the acquisition system of the spectrometer takes care of encoding the ADC values of one side of a plane of the tracking system and of packing them. Cyclic Redundancy Checks (CRC) are added by the control logic to be able to identify during the offline data handling possible errors introduced by single-event effects due to ionizing radiations on the electronic devices [62]. Data coming from the tracking system are then stored in the mass memory of the main CPU of PAMELA together with data generated by the other detectors, to form a complete event packet. The content of the mass memory is periodically transferred into the spacecraft non-volatile storage system (*download*) and merged with data coming from the other instruments of the satellite (from the Earth observation devices, from telemetry, etc.). When the satellite transits the transmission window over the receiving station located near Moscow, blocks of data can be sent by a radio link to the ground facility (*downlink*), where they are stored and where the analysis process begins.

As a first step, the data blocks are extracted from the satellite downlink encoding and validated against transmission errors: their quality is verified and they are rearranged in files which reproduce their original sequence in the CPU mass memory. A fast data reduction and visualization procedure based on ROOT [61] scripts ("PAMELA *Quicklook*") is then executed, which checks some selected critical values regarding the acquisition and the status of the single detectors, and also a set of engineering parameters such as temperature of different parts of the apparatus or voltage levels, to ensure they fall in their nominal acceptable range (see Fig. 3.1). In case of validation failures because of some incon-

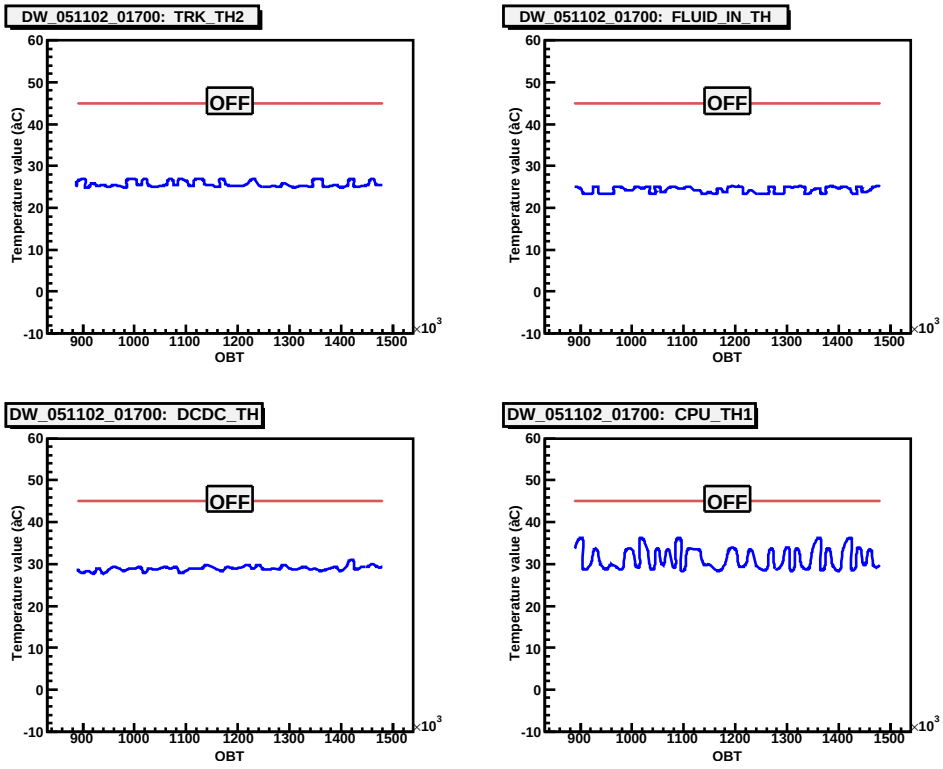


Figure 3.1: *Some of the plots generated by* Quicklook *scripts to monitor the temperature of different parts of the instrument. The values are reported in Celsius degrees as a function of the On-Board Time (OBT), which is the time elapsed since the CPU booted up, expressed in milliseconds. The line in the upper part of each plot shows the chosen safety value of the temperature which causes the system to power-off.*

sistency, after each downlink a time interval of about six hours is available to ask the mission control to repeat the transmission before data being overwritten in the satellite storage system. If instead some of the parameters controlled by means of the *Quicklook* do indicate some detector anomaly, radio commands can be sent from ground to the spacecraft in order to modify PAMELA settings, such as for instance the high voltage values of the TOF photomultipliers or the acquisition parameters; even the acquisition software can be updated in case some major bug is found.

### 3.1.1 The spectrometer compression algorithm

Since the amount of information which can be sent to the ground receiving station is limited to about 10 GB/day, a data compression procedure has been adopted for the calorimeter and for the spectrometer. While for the former a standard "zero-suppression" technique is employed, the latter, which with its 36 864 electronic channels is the detector producing the largest output, needs a more elaborate approach. In this case the compression is performed using a software [63] based on a ZOP (Zero-Order Predictor) algorithm and modified for including a peak-identification method, which ensures that the information carried by strips that have been hit by a particle is not lost in the compression. By exploiting the known characteristics of the data flow which has to be processed, it has been shown during tests on particle beams that this technique allows to obtain a compression ratio of about 95% without any worsening in spatial and momentum resolution of the detector.

The ADC value of each strip is due to different sources, and it can be expressed schematically as the result of the sum of three distinct contributions:

$$ADC^i_{j,k} \;=\; PED_{j,k} \;+\; CN^i_k \;+\; S^i_{j,k}\,. \tag{3.1}$$

When no signal coming from the passage of a particle is present, this voltage value for a certain $j$-th strip belonging to the $k$-th VA1 chip fluctuates according to a Gaussian function whose mean is represented by $PED_{j,k}$, which is called the *pedestal*, and whose standard deviation is

indicated as $\sigma_{j,k}$. The pedestal is a base level which is determined by the detector structure and electronics and it is different for each channel: its value is constant in time and thus it is the same for every event[1]. The standard deviation $\sigma_{j,k}$ represents the *intrinsic noise* of that channel, and it is uncorrelated to the fluctuations of the others. In addition, another noise source is present, which is mainly induced by the power supply of the detector electronics, by the reverse bias voltage of the silicon sensors, and by the possible external electromagnetic noise collected by the device. This contribution is equal for all the strips connected to a single VA1 chip, and for this reason it is referred to as *common-mode noise*, or simply *common noise*: $CN_k^i$ represents the value that it has at the $i$-th event, for all the 128 strips of the $k$-th VA1. Finally, the variation of $ADC_{j,k}^i$ for the $j$-th strip of the $k$-th chip when it collects a fraction of the charge produced by a cosmic ray crossing the silicon sensor (the true meaningful *signal*) is indicated as $S_{j,k}^i$ for the $i$-th event. Therefore the expected outline of the ADC output for each event is a nearly flat profile for all the strips due to the pedestal (which but shows a fine structure), on which common-noise fluctuations that are the same for groups of 128 adjacent strips are superimposed, and isolated peaks due to particle ionization are present.

When data are acquired in compressed mode, not all the ADC values are stored: instead, for each one of the 12 sides of the tracking system planes the value of the first strip is always transmitted, and the decision on whether a following one has to be kept or not is taken on the basis of the variable $C_j = ADC_j - PED_j$, which is computed *online* (i.e. at acquisition time) by the DSP software[2]. If $ADC_{j-l}$ represents the last channel value which has been stored, the difference $\Delta_j = |C_j - C_{j-l}|$ is considered, and the $j$-th strip is transmitted if:

$$\Delta_j \; > \; t_{ZOP} \cdot \sigma_j \,, \tag{3.2}$$

[1]This is strictly true only in principle: in practice pedestals can slightly vary in time. This is the reason why their values are estimated periodically, as explained later in Sec. 3.1.2.

[2]In order to make equations clearer, the event and the VA1-chip indexes will not be written explicitly in the following.

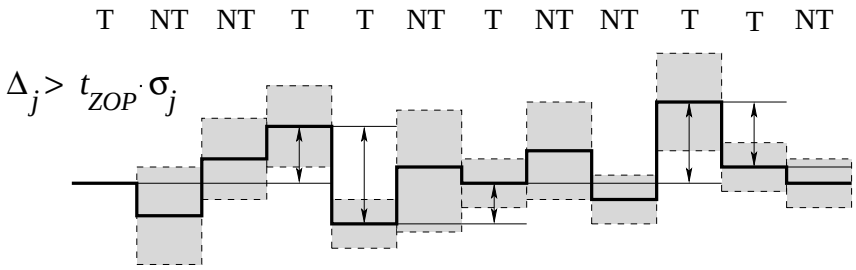


Figure 3.2: *The zero-order predictor algorithm: the value of the first strip is stored, the other ones only in case* $\Delta_j > t_{ZOP} \cdot \sigma_j$*. The thick line represents* $ADC - PED$ *for the various channels, the shaded area around the line shows their intrinsic noise (different for each strip) multiplied by the threshold* $t_{ZOP}$*. The labels T and NT indicate transmitted and non-transmitted values, respectively.*

that is only if its $ADC_j - PED_j$ value is far enough from that of the previous one. Since higher-noise strips would often exceed a constant cut because of their wider fluctuation range, the threshold $t_{ZOP}$ is multiplied by the intrinsic noise $\sigma_j$ of the channel. In Fig. 3.2 an example of how the ZOP algorithm works is displayed. The peak-identification method which complements the compression software forces the ADC values of the couple of strips which precedes and of the couple which follows a stored channel $j$ to be included as well, if $\Delta_j$ exceeds the transmission condition (3.2) with a higher threshold $t_{peak}$. In this way the information provided by channels with a large signal due to a particle charge release is not likely to be discarded. The values which have been chosen as ZOP and peak thresholds are:

$$\begin{aligned} t_{ZOP} &= 4 \\ t_{peak} &= 7 \end{aligned} \tag{3.3}$$

and represent a compromise between the need of a high compression level and the requirement of preserving the detector performances. In order to know which strips have fulfilled the previous conditions, the number

that identifies the position of the strip on the silicon sensor surface is transmitted as well together with the ADC value, unless that of the previous one has already been. Although this compression algorithm is not reversible (i.e. it does not allow to recover the original values of all the strips, but some part of the information is unavoidably lost), the procedure has been optimized so that it does not worsen the spatial resolution and the detection efficiency of the silicon sensors.

### 3.1.2 Online calibration procedures

The information that is necessary in the compression process (namely pedestal and intrinsic noise for each strip) is calculated by the DSP software during *calibration runs* which are carried out from time to time in the course of the mission. In fact $PED$ and $\sigma$ for a strip are not strictly constant in time, and periodic calculations of these quantities ensure that suitable values are employed in the compression algorithm.

If a set of $N_{ev}$ events which do not contain particles is acquired (an artificial trigger signal generated by a command coming from the CPU of PAMELA is used for this purpose), the requested quantities can be estimated online. Indeed in case $S^i_{j,k} = 0$, the pedestal of the generic $j$-th strip of the $k$-th VA1 chip can be computed from Eq. (3.1) as its average ADC value, after the common-noise contribution has been subtracted:

$$PED_{j,k} \;=\; \sum_{i=1}^{N_{ev}} \frac{ADC^i_{j,k} - CN^i_k}{N_{ev}} \,. \tag{3.4}$$

Likewise, once the pedestals are known, the common noise of each of the VA1 can be obtained for the $i$-th event as:

$$CN^i_k \;=\; \sum_{j=1}^{128} \frac{ADC^i_{j,k} \;-\; PED_{j,k}}{128} \,, \tag{3.5}$$

where the sum extends to the 128 strips connected to the $k$-th chip. Finally the strip intrinsic noise is given by:

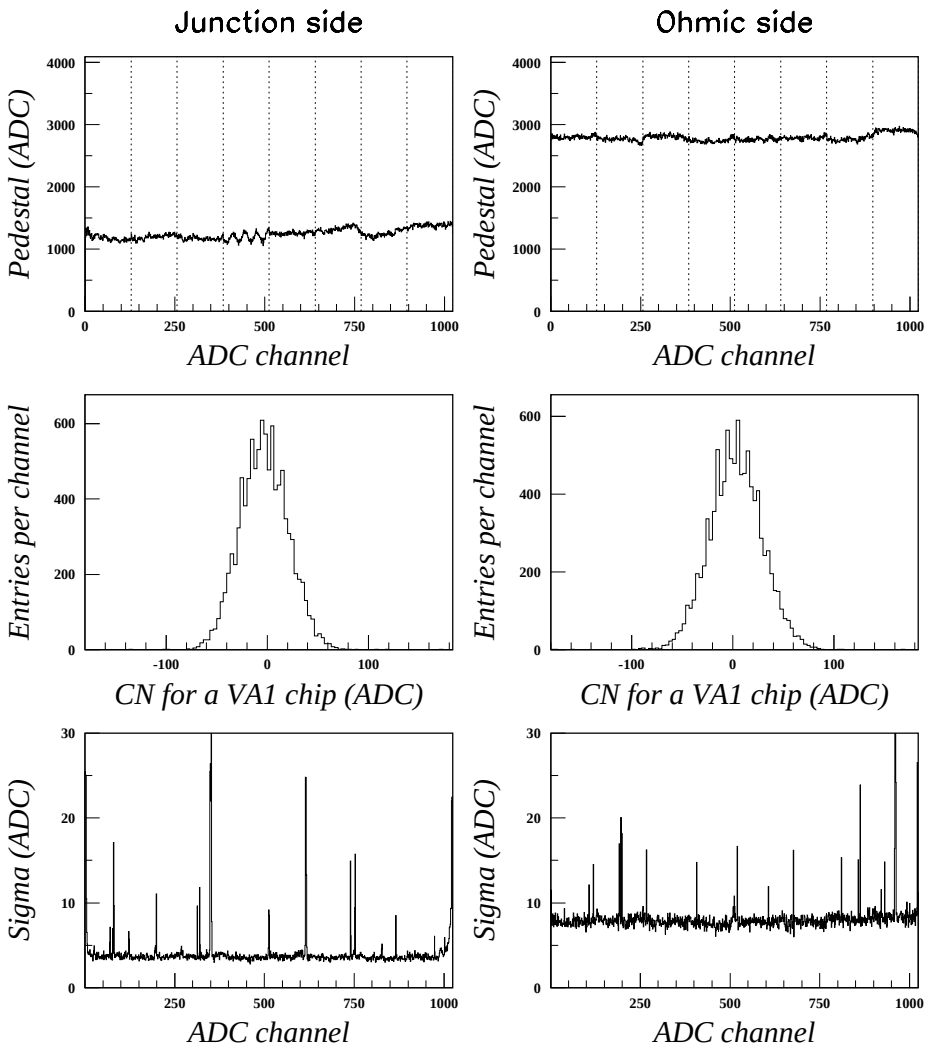


Figure 3.3: *Calibration parameters of a* ladder *of the tracking system. From top to bottom: pedestals, common-noise distribution for one of the VA1 chips, and intrinsic noise $\sigma$ of the strips. Left and right columns refer to the junction and ohmic sides, respectively, which are used to measure the X and Y coordinates of the particle impact point.*

$$\sigma_{j,k} = \sqrt{\frac{1}{N_{ev}-1}\sum_{i=1}^{N_{ev}}\Big(ADC^i_{j,k} - CN^i_k - PED_{j,k}\Big)^2}, \qquad (3.6)$$

since it represents the standard deviation of the signal of each channel around its base level. These quantities are calculated iteratively, first evaluating pedestals from Eq. (3.4) under the initial assumption $CN^i_k = 0$, then using Eq. (3.5) to determine the common noise for each event, and repeating the procedure to get better estimates for $PED$ corresponding to new values of $CN$. At each step $\sigma_{j,k}$ is also computed from Eq. (3.6), and strips are classified according to their intrinsic noise: those having a noise more than 5 standard deviations away from the average calculated for each VA1 chip are not used when evaluating the common noise. Actually, defects in the construction of such microstrip detectors can be the cause of short circuits between adjacent strips and of the presence of pinholes in the insulating silicon-dioxide layer between the implantations and the read-out electrodes. Moreover, some strip can be interrupted or not properly connected due to problems in the bondings between the sensor and the hybrid circuit, or between the two sensors of a *ladder*. These two categories of possible faults result in channels showing a noise level higher or lower than the standard one, respectively. Those strips which do not survive the cut on $\sigma$ are labeled "*bad*" and they are not considered during $CN$ computation, since they would bias it: as the iterative procedure advances, better estimates for the calibration parameters are found, and further strips are marked for exclusion. The final values of pedestals and intrinsic noise, as well as the complete map of *bad* strips (which typically amount to less than 5% of the total in each *ladder*) are obtained after repeating the process eight times on a set of $N_{ev} = 128$ events: an example of the results of the calibration is reported in Fig. 3.3 for the two sides of a *ladder* of one of the spectrometer planes. Among the 1024 strips, those characterized by a high intrinsic noise can be noted, while the typical value of $\sigma$ is about 4 ADC channels for the X side and lower than 9 for the Y one, the difference being mainly caused by the unequal biasing resistances for the two sides and by the increased capacitance on the ohmic one, also due to the double metallization.

At the end of each calibration run these values are stored in the DSP and used for compressing data for the acquisition runs which follow. In this way each data set is uniquely associated with a calibration, whose parameters are downlinked to ground in dedicated calibration packets, since they are required for decompressing and for extracting particle signals, as it will be explained in Sec. 3.3 (actually only pedestals, $\sigma$ values and *bad* strips are downlinked, not the common noise which will be calculated again offline for each event). If for some reason the calibration procedure fails[3] a standard set of calibration parameters which have been stored in dedicated non-volatile solid-state memories are loaded into the DSP and used instead, in order to be able to compress and transmit data in any case.

## 3.2 Data unpacking and reading

The files that result from the decoding of the blocks downlinked from the satellite, act as an input for the first step of the main data reduction, which takes place in parallel to the fast analysis procedure of the PAMELA *Quicklook* that is used to control the status of the detectors. A C++ software called YODA ("Your Own Data Analysis") takes care of identifying the different packets in the data stream and of supplying them to the various subroutines which extract the output information of each detector. The reading subroutine of the spectrometer recognizes the format of the initial part of the data structure (the so-called *header*) by means of its distinctive pattern of bits, and checks for the presence of possibly corrupted events by verifying the CRC code of the data packets. The header allows to distinguish between calibration and particle runs and contains the information about the acquisition parameters which have been used for that particular run. As regards calibration packets, the maps of pedestals, intrinsic noise values and *bad* strips are extracted and stored to be used later to identify clusters. A list of calibrations is

[3]Several consistency checks are performed at the end of the calibration, such as controlling that the obtained values fall in their expected range or that the correct number of events has been actually employed. In case some problem is found, the calibration is attempted three times before considering it as failed.

also created, in order to be able to assign to each run the correct parameters for the decompression and the analysis of the signal. The contents of the acquisition runs are instead unpacked and transferred from the original binary file to the HBOOK data structure which is the common framework of the following reduction steps.

## 3.3 Signal analysis and cluster identification

The next stage of the reduction process deals with the decompression of data. It is performed by associating to each run of data the right set of downlinked calibration parameters (or the standard set), and rebuilding for each event the ADC profile of all the twelve detector sides of the tracking system. The ADC value of the groups of strips which have been cut out in the compression because of the condition expressed by Eq. (3.2) are inferred on the basis of the last transmitted one (whose index is $j-l$), as:

$$ADC^i_{j,k} \;=\; PED_{j,k} \;+\; (ADC^i_{j-l,k} - PED_{j-l,k})\;. \tag{3.7}$$

As stated before, this technique does not spoil the spatial resolution of the detector, since the peak-identification part of the algorithm ensures that the information on hit strips is preserved [63].

Once all the channels have been reconstructed, the signal analysis can start, in order to isolate the contribution due to the passage of ionizing particles across the sensors. The signal can be obtained from Eq. (3.1), as:

$$S^i_{j,k} \;=\; |\; ADC^i_{j,k} \;-\; PED_{j,k} \;-\; CN^i_k \;|\;, \tag{3.8}$$

where the absolute value is used because on the X (junction) and Y (ohmic) sides of the silicon sensor it has opposite sign, since electrons and holes are collected, respectively. The common noise for each event has to be computed again as it had been done during the online calibration

phase, but special care has to be taken now since in this case the data set contains channels bearing particle signals, which have to be excluded. Hence, a first rough cut is done by removing both the strips which have been labeled as *bad* during the calibration, since their altered intrinsic noise values make them less reliable, and those whose $ADC - PED$ is more than 3 standard deviations away from the average. Then a finer selection is performed, by combining a recursive procedure similar to the one described in Sec. 3.1.2 with the peak identification strategy followed during the compression (Sec. 3.1.1). At each iteration, common noise is evaluated according to Eq. (3.5) using the known values of $PED$ and $ADC$ for all the channels which have survived until that step, and their signal is then calculated from Eq. (3.8); a strip is considered hit by a particle and consequently removed from the $CN$ computation if it carries a signal greater than 7 times its intrinsic noise, and in that case all the adjacent ones which pass a lower, 2-$\sigma$ cut are excluded as well; a new estimate for the common noise is thus obtained, and the process iterated till no more strips are excluded.

When the final value of $CN^i_k$ has been determined, the signal can be computed definitely and the search for "*clusters*" (i.e. groups of contiguous strips on the two sides of the six planes which have collected particle signals for a given event) can start. Again the identification is done on the basis of the signal-noise ratio of each channel, by looking for those whose signal, expressed by Eq. (3.8), is appreciably larger than the fluctuations due to intrinsic noise. If a strip satisfies the condition:

$$S^i_{j,k} \; > \; C_{seed} \; \cdot \; \sigma_{j,k} \tag{3.9}$$

with $C_{seed} = 7$, it is classified as the "*seed*" of a cluster, this being closely related to the cosmic-ray impact point. Adjacent strips on both sides of the *seed* are scanned to check if they pass a similar cut:

$$S^i_{j,k} \; > \; C_{incl} \; \cdot \; \sigma_{j,k} \; , \tag{3.10}$$

but with a lower threshold $C_{incl} = 4$, and, if so, they are included as

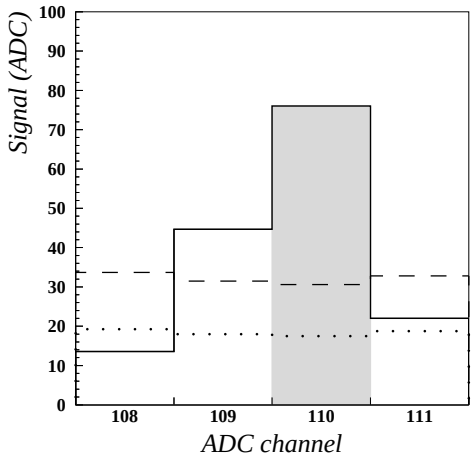


Figure 3.4: *The signal profile of a portion of a sensor side in which a cluster has been identified. The continuous line histogram represents the signal in ADC counts, the dashed line is the* seed *identification threshold (Eq. (3.9)), while the dotted line the strip inclusion threshold (Eq. (3.10)): the shaded channel is recognized as the cluster* seed*; strips 109 and 111 are included as part of the cluster.*

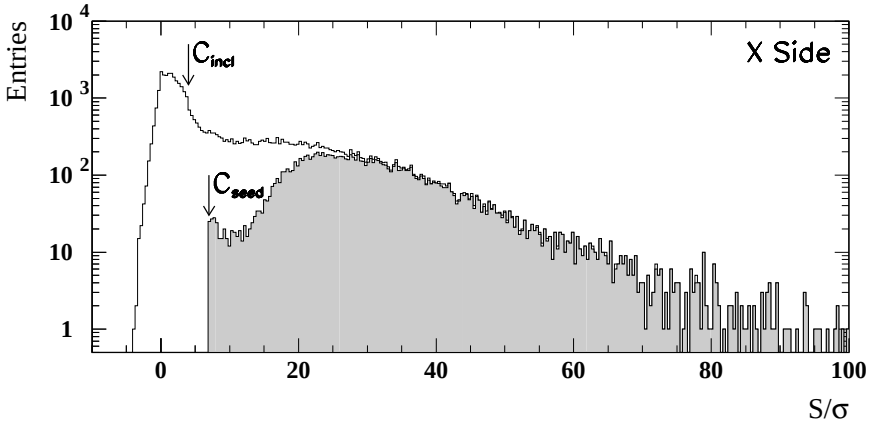


Figure 3.5: *Signal-noise ratio of strips, for the X side of the silicon detectors. Arrows show the thresholds* $C_{seed} = 7$ *and* $C_{incl} = 4$ *which are used respectively to identify* seeds *and to include strips in a cluster. The shaded area represents the same ratio for the* seed *strips: the low* $S/\sigma$ *end of the distribution contains a contamination of noisy strips, whose clusters are excluded during the following track recognition and fitting phase.*

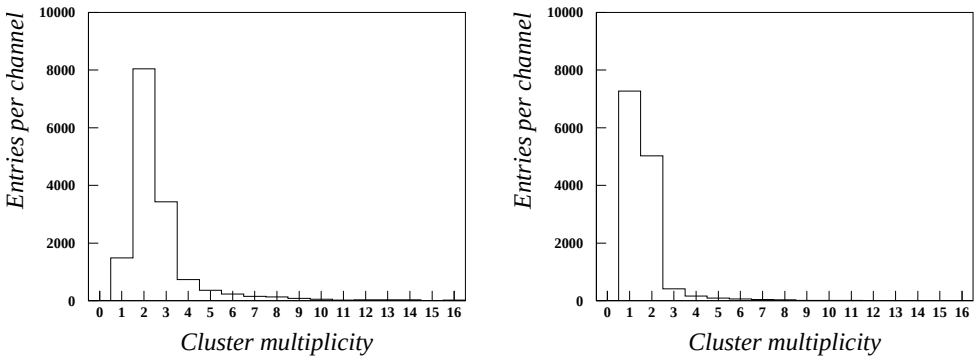


Figure 3.6: *Multiplicity of clusters for the X (left) and Y (right) sides of the tracking planes. Data consist in cosmic rays detected at ground level with a maximum incidence angle on the silicon sensors of about* 20°.

well in the cluster. If several consecutive strips pass the *seed* condition, the one with the maximum $S/\sigma$ is chosen: with reference to Fig. 3.4, where an histogram which represents the signals of a group of consecutive channels is shown, both strips labeled 109 and 110 carry a signal greater than the 7-$\sigma$ cut, and the second one is taken as the *seed*. The values of the cuts have been calibrated through the several tests on particle beams which have performed in the course of last years, in order to optimize the detection of minimum ionizing particles according to the characteristics of the detector. A plot which shows the cluster thresholds $C_{seed}$ and $C_{incl}$ with respect to the distribution of the signal-noise ratio of the strips is reported in Fig. 3.5.

The number of strips which pass the inclusion cut given by Eq. (3.10) (together with the cluster *seed*) defines the *multiplicity* of the cluster, a quantity related to the way the ionization charge is shared among the different strips involved in the process, and which depends on the implantation pitch and on the thickness of the sensor with respect to the incidence angle of particles. For most of the events in PAMELA the multiplicity is 2 for the clusters belonging to the X side and 1 for those of the Y side, due to the larger pitch (see Fig. 3.6 for an example of the distribution of cluster multiplicity). In spite of this typical low

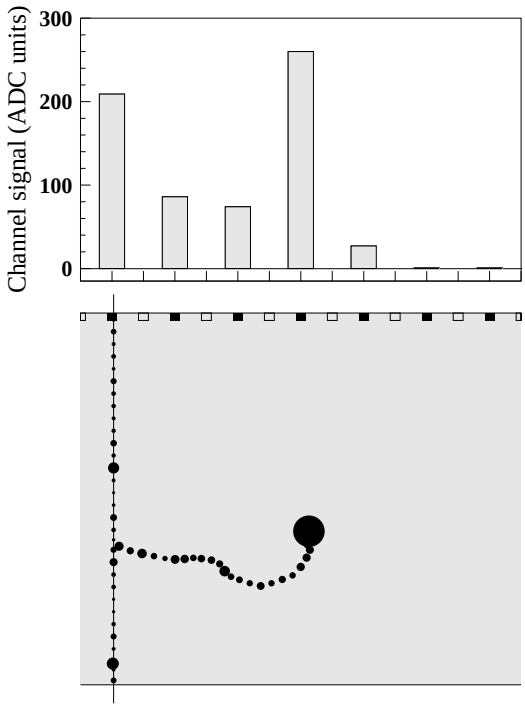


Figure 3.7: *Effect of high-energy* $\delta$-rays *on the reconstruction of the impact point. In the lower part of the picture, a section of a silicon sensor crossed by a cosmic ray is shown: the simulated ionization is represented by the black dots, whose radius is proportional to the charge released. A high-energy* $\delta$-ray *is present, which generates additional ionization along its path. In the upper part of the picture the corresponding signals on the detector strips are shown (from Ref. [64]).*

multiplicity, events can be found having clusters with a higher number of hit strips on some planes, even for low incidence angles. A careful simulation and study about the silicon sensors and their impact-point reconstruction capabilities [64] has shown that such cases can occur when high-energy *$\delta$-rays* are produced during the ionization process. A $\delta$-ray is obtained when the ionization effect due to the cosmic ray releases an electron with an energy greater than the binding energy of atomic electrons, so that this secondary particle is able to ionize in turn along

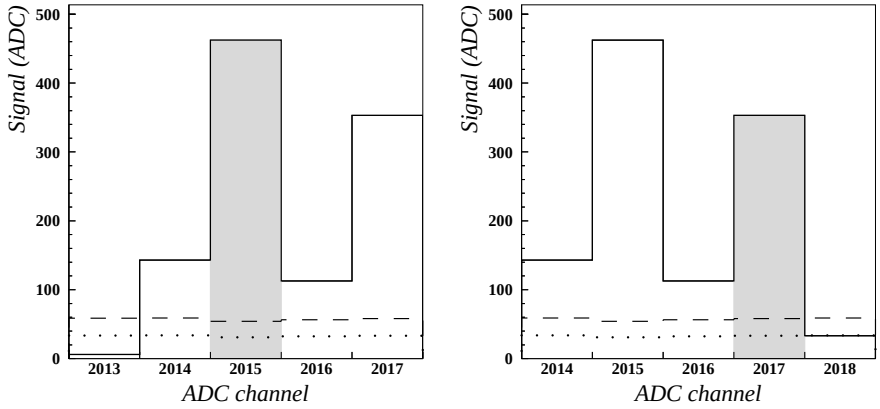


Figure 3.8: *A double-peak cluster, which is included twice with two different cluster* seeds *in the set of clusters of the event (see Fig. 3.4 for explanation of graphical details).*

its path. The additionally generated charge (in particular the Bragg's peak at the end of the path of the $\delta$-ray) can deform the shape of the cluster, or even make an additional high-signal strip appear other than the cluster *seed* which should be associated with the particle true impact point (see Fig. 3.7). When $\delta$-rays have an energy comparable to that which an incident particle loses on average because of primary ionization (about 84 keV in a 300 $\mu$m silicon layer, if the large fluctuations due to energetic secondaries are ignored) their range in silicon is of some tens of $\mu$m. For this reason their presence can significantly affect the determination of the true impact point of the cosmic ray, and so the measurement of its deflection. In order to minimize such problems, the inclusion of strips according to Eq. (3.10) is done in such a way that clusters can be asymmetric respect to the *seed*. Those which have more than one maximum above the *seed* threshold shown in Eq. (3.9) are called *double-peak* clusters and are included twice: they are considered as two different potential impact points on that plane and the true one will be afterwards recognized during the track reconstruction phase, as the one which makes the trajectory fitting the best (see Sec. 3.5.1 for details on

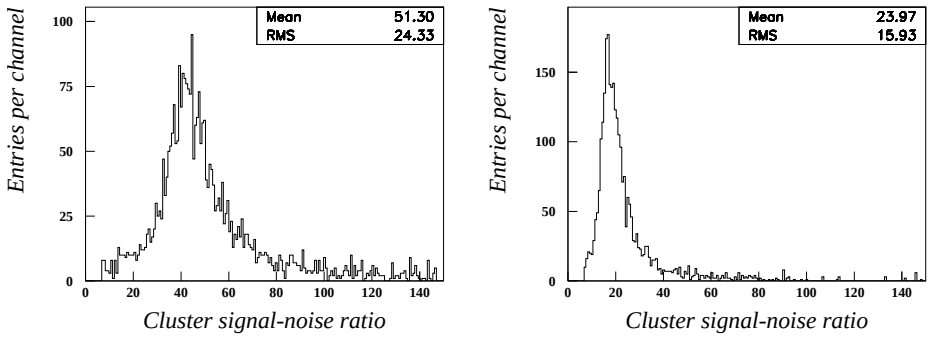


Figure 3.9: *Distribution of the signal-noise ratio of clusters, for the X (left) and Y (right) sides of one of the silicon detectors.*

how impact points are associated to tracks). An example of a *double-peak* cluster is reported in Fig. 3.8.

After a cluster has been identified and its multiplicity has been determined, the sum of the signal of all the included strips is calculated: the total signal is a quantity which is proportional to the ionization release, and thus to the energy lost by the cosmic ray and to its charge squared $Z^2$. The signal-noise ratio of a cluster is also evaluated, as the ratio between the total signal and the average noise of the cluster $\langle\sigma\rangle_{cl}$:

$$(S/N)_{cl} \;=\; \frac{\sum_{i=1}^{m} S_i}{\langle\sigma\rangle_{cl}} \;, \tag{3.11}$$

where $m$ is the multiplicity and $S_i$ are the signals. If, in order to take into account the intrinsic performance of each strip, a weighted average with the signal-noise ratios of each of them as weights is used to compute $\langle\sigma\rangle_{cl}$, the above relation becomes:

$$(S/N)_{cl} \;=\; \sum_{i=1}^{m} \frac{S_i}{\sigma_i} \;, \tag{3.12}$$

that is to say the signal-noise ratio of the cluster is the sum of the signal-noise ratios of its strips (see also Ref. [65]). This parameter is

important since higher values correspond to a better spatial resolution. The distributions of the signal-noise ratio on the two sides of the silicon tracker sensors of PAMELA are shown in Fig. 3.9: the mean of the distribution is about 51 for the junction side and about 24 for the ohmic one, showing that a very good resolution can be achieved.

At the end of this reduction stage, all the quantities related to clusters are stored in data structures which will be used as the starting point for the calculation of the coordinates to be associated to the particle impact points on the tracking system planes. In this way only the information about the channels involved in the passage of particles is retained, while that of the other ones is discarded. Actually, since the techniques used to reconstruct the coordinates of the impact point can possibly need the knowledge of signals of several strips around the incidence position, as it will be shown in detail in the following Sec. 3.4, the number of strips which are stored for a cluster is not always simply its multiplicity, but can even be greater. In particular, to be able to employ at best the information for any possible particle incidence angle in PAMELA, a minimum of four channels around the *seed* are always recorded.

## 3.4 Impact-point reconstruction

Before being able to reconstruct tracks from the knowledge of the points of the particle trajectory on the detecting planes, each cluster has to be associated to a measure of the coordinate of the impact point on the side of the sensor it belongs to. A quite intuitive approach to such problem consists in associating to the impact point the *center of gravity* of the cluster. In this way, the estimate of the coordinate on the sensor[4] is obtained as the mean of the coordinates $x_i$ of the strips of the cluster, weighted by their respective signals $S_i$:

$$x_{cog} = \frac{\sum_{i=1}^{m} S_i \, x_i}{\sum_{i=1}^{m} S_i} , \tag{3.13}$$

[4]The following discussion applies both to the X and Y coordinates: the symbol $x$ will be used to indicate either of them.

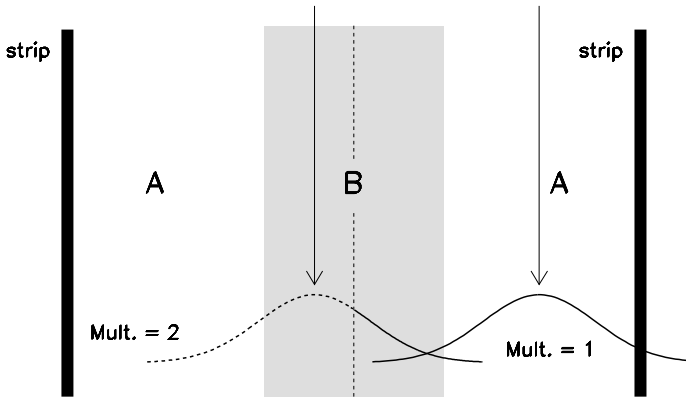


Figure 3.10: *Sketch of the interstrip charge division mechanism. The impact point of a orthogonally incident particle is represented as an arrow: if it lies in the region A near a strip the multiplicity of the resulting cluster will be 1, if in region B multiplicity will be 2 (from Ref. [66]).*

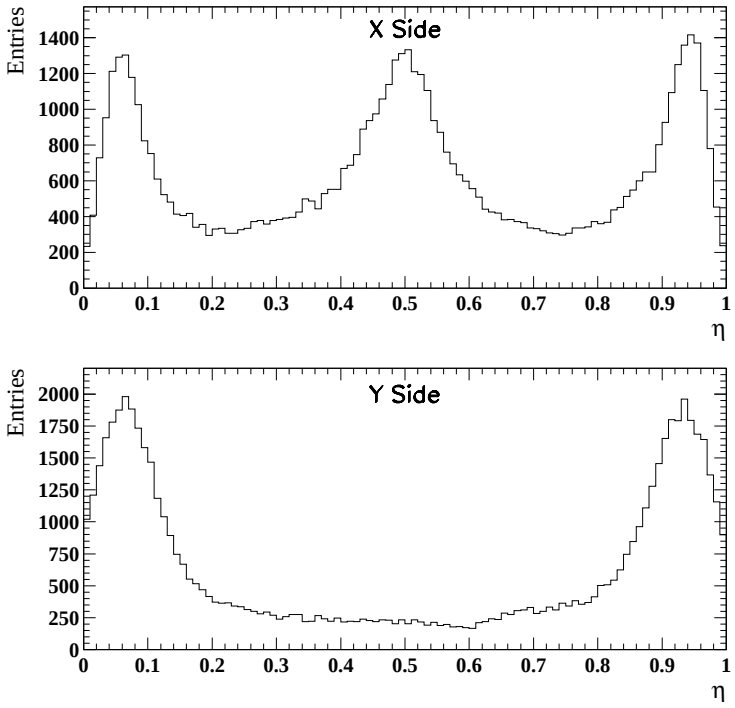


Figure 3.11: *Distribution of the η variable for the two sides of a sensor. The peaks near 0 and 1 show that in the majority of the cases one strip collects nearly all the ionization charge. The peak near 0.5 on the X side is due to the* floating *strip which favors the charge sharing between the adjacent pair of read strips.*

where $m$ is the cluster multiplicity. Actually, since as it has been shown before, in the case of PAMELA the multiplicity is often 1 or 2 (Fig. 3.6), generally it is convenient to restrict the above sum to the couple of strips bearing the majority of the cluster signal. The reason for this choice can be better clarified if the way the charge is shared among strips is closely examined. With reference to Fig. 3.10 and following Ref. [66], the portion of sensor between two adjacent strips can be schematically divided into two areas, which differ in the way the packet of free charge generated by a perpendicularly incoming particle is shared. While the packet drifts towards the electrodes it assumes a Gaussian-like shape with a width (of about 15–20 $\mu$m) which is smaller than the detector pitch. Consequently, if the cosmic ray passes next to the strips (region A) almost all its ionization will be collected by the nearest strip only, thus giving rise to a cluster with $m = 1$, while if it hits the intermediate region B the charge will be shared in a nearly linear way and multiplicity will be 2. A useful quantity which can be defined when dealing with the two strips on the left and on the right of the incidence point, is the fraction of the total signal which the channel on the right receives:

$$\eta = \frac{S_R}{S_L + S_R} \,, \tag{3.14}$$

in which $S_L$ and $S_R$ are the values of the signals of left and right strips, respectively. The $\eta$ variable[5] lies by definition in the interval $[0, 1]$ and, in the case of particles hitting orthogonally and uniformly the surface of the sensor, its expected distribution should have peaks near the borders of the interval, because of the behavior of the charge collection mechanism in the outmost region A of the interstrip space. Apart from distortions and spreading due to losses of signal and to capacitive couplings among the strips, this is actually what it is found experimentally: typical $\eta$ distributions are reported in Fig 3.11 for the two sides of a sensor. On the

[5]Following the usual custom found in literature, the symbol $\eta$ will be used to indicate both the magnetic deflection of particles and the charge fraction of cluster strips. The correct meaning will be explicitly indicated, when not self-evident from the context.

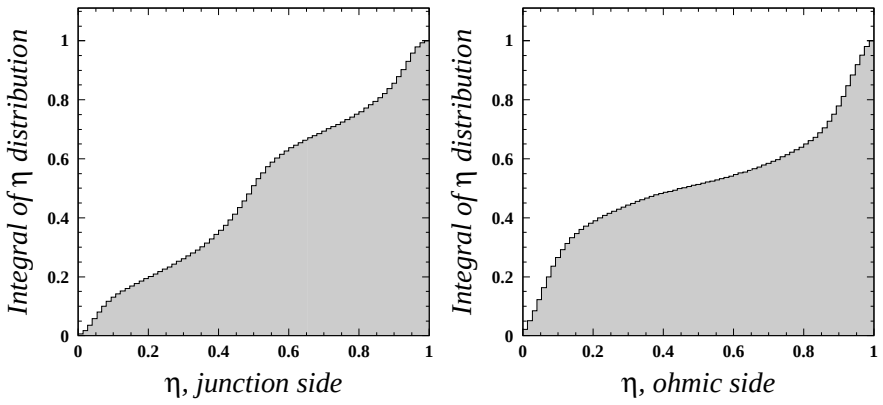


Figure 3.12: *Integral of the distribution of the η variable for the junction (left) and ohmic (right) sides of the sensors (from Ref. [66]).*

X side, the unread *floating* strip (see Sec. 2.4.3) favors the sharing of the charge and accounts for the presence of the additional peak around $\eta = 0.5$. Since most of the information on the passage of the particle is contained in the couple of strips at the sides of the impact point, while the noise of the channels is about the same for all of them, if those which have collected a low signal are excluded, the signal-noise ratio of the cluster is generally increased, and thus the spatial resolution improves as well. Therefore, a two-strip center of gravity is used, and the impact point $x_{cog2}$ is determined as:

$$x_{cog2} \;=\; \frac{S_L\; x_L + S_R\; x_R}{S_L + S_R} \;=\; x_L \;+\; P \cdot\; \eta\;, \tag{3.15}$$

where $x_R$, $x_L$ are the coordinates of the right and left strips and $P = x_R - x_L$ stands for the read-out pitch.

This method gives a good estimate of the true impact point, but only to a certain approximation. In fact, it can be demonstrated that the discretization which results from sampling over the strips a charge packet, which in our case has an almost Gaussian shape, introduces in general a systematic shift in the reconstructed impact point respect to the true

position, if the simple center-of-gravity approach is used [67]. A method which allows to take into account the non-linear effects which occur in the division of the signal consists in using the so-called *non-linear $\eta$ algorithm*. It can be easily proved (see Ref. [66]) that for an uniformly illuminated sensor the simple relation $\xi = P \cdot f(\eta)$ exists between the interstrip impact point $\xi \in [0, 1]$ and the *cumulative probability distribution function* of the $\eta$ variable $f(\eta)$. By exploiting this equality, the coordinate of the particle can be estimated as:

$$x_\eta \;=\; x_L \;+\; \xi \;=\; x_L \;+\; P \;\cdot\; f(\eta)\;. \tag{3.16}$$

By the definition of cumulative probability distribution function, $f$ for a given value $\eta^*$ represents the fraction of clusters having $\eta < \eta^*$. Hence it can be extracted from data simply by integrating the experimental distribution of the $\eta$ variable $dN/d\eta$ (represented by an histogram such as those in Fig. 3.11) which is obtained in conditions as close as possible to the ideal situation of uniform illumination. Its expression is:

$$f(\eta) \;=\; \frac{\displaystyle\int_0^{\eta} (dN/d\eta')\; d\eta'}{\displaystyle\int_0^{1} (dN/d\eta')\; d\eta'}\;, \tag{3.17}$$

and it corresponds to a strictly increasing function in the interval $[0, 1]$, with a behavior depending on the intrinsic characteristics of the sensor. The typical shape of $f(\eta)$ is depicted in Fig. 3.12, from which the non-linear behavior of the correction to the impact point can be appreciated.

Given the characteristics of the sensors of the tracking system of PAMELA, this approach to the coordinate reconstruction problem provides the best spatial resolution, at least in case of particles which hit silicon orthogonally or with not too large angles. In fact, when the incidence angle respect to the vertical direction increases, a larger number of strips may be involved in the charge collection. Therefore the spatial resolution of the detector can be improved if the information carried by

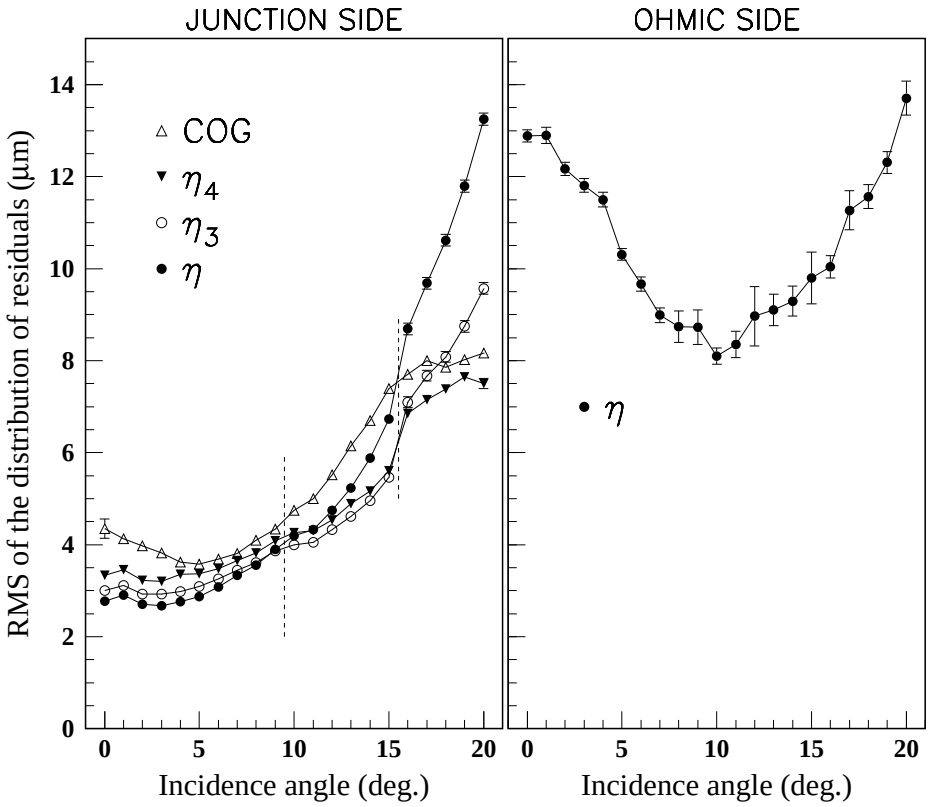


Figure 3.13: *Simulated width of the distribution of the difference between the true impact point and the reconstructed one, as a function of the particle incidence angle. On the left, the results obtained through the center-of-gravity (COG), $\eta$, $\eta_3$ and $\eta_4$ algorithms for the X side of the sensors; on the right the results of using the eta algorithm for the Y side. Vertical dotted lines indicate the points where a change in the chosen reconstruction method betters the resolution (from Ref. [64]).*

further channels is employed: in particular the non-linear $\eta$ algorithm can be modified in such a way as to use the cluster *seed* and the two strips on both its sides ($\eta_3$), or the couple of strips used to compute $\eta$ and their first neighbors ($\eta_4$). The straightforward extension of the definition of the $\eta$ variable gives:

$$\eta_3 = \frac{S_1 + 2\ S_2}{S_0 + S_1 + S_2} \qquad \text{and} \qquad \eta_4 = \frac{S_1 + 2\ S_2 + 3\ S_3}{S_0 + S_1 + S_2 + S_3}\ , \tag{3.18}$$

where $S_0$ stands for the signal of the leftmost among the used strips, and the other ones on the right are labeled with increasing indexes. In a similar way, the corresponding cumulative probability distribution functions $f_3$ and $f_4$ are estimated as in Eq. (3.17). The detector resolution has been studied for different incidence angles (see Fig. 3.13), and the procedure which has been chosen as the most satisfactory for the reconstruction of the X coordinate of the impact point consists in using the $\eta$ algorithm for incidence angles lower than 10°, $\eta_3$ between 10° and 16°, and $\eta_4$ between 16° and 20°, which is the maximum angle on the spectrometer sensors for tracks in the acceptance of PAMELA. In this way the resolution which is achieved in the determination of the X coordinate of the particle in the bending plane is lower than 4, 6 and 8 $\mu$m, for the three intervals respectively. On the contrary for the Y side the standard $\eta$ algorithm gives satisfactory results in the whole 0° – 20° range, since the larger implantation pitch causes the charge to be nearly always collected by one or two strips (about 97% of the cases), and a resolution between 8 and 14 $\mu$m is obtained[6].

For each cluster, the interstrip center of gravity is calculated according to Eq. (3.14) (or possibly even Eq. (3.18) for the X side, depending on the incidence angle), and the impact point is obtained from Eq. (3.16), once the correct cumulative probability distribution function has been

[6]Recently it has been found that another systematic effect arises when the $\eta$ algorithm is applied in the usual way to non orthogonal tracks. In this case in fact the asymmetry of the charge packet generated by ionization can result in a shift of the reconstructed impact point with respect to the true one. Ref. [68] describes the problem and suggests possible solutions: further work is at the moment in progress to include this correction in the impact-point reconstruction algorithms of the spectrometer.

computed. The determination of these functions, that is to say the calibration of the reconstruction algorithms, has to be done on a sample of clusters which can be doubtless associated to the passage of a particle, thus avoiding those generated by noise which could have passed the identification criteria described in Sec. 3.3. For this reason a subset of "clean" events is selected, in which spurious clusters are not present: they are accepted if they do not contain strips tagged as *bad* during online calibration (because of their anomalous intrinsic noise), and if they pass a cut on multiplicity, in order to decrease the possible effect of $\delta$-rays. Events are considered which have on each side of the planes just one cluster, whose position is consistent with a real track. These clusters are then classified according to the incidence angle of the particle which generated them and the distributions of the $\eta_i$ variables are computed for each group: the calibration curves $f(\eta)$, $f_3(\eta_3)$ and $f_4(\eta_4)$ at different angles are finally obtained by integration of these distributions, as in Eq. (3.17). The algorithms have been calibrated with data of cosmic rays gathered at ground level in 2005, and further calibration will be repeated later during the flight.

Another aspect that has to be taken into account in order to determine the correct impact point is the effect of the magnetic field on the charge collection. Since the detectors of the tracking system are encased in the cavity of the permanent magnet, charge carriers are subject to the Lorentz force while moving from the generation point along the particle track inside the silicon sensor to the collecting electrodes on its surfaces. The force causes the drift in the electric field generated by the reverse biasing to occur with an angle $\theta$ respect to the field lines. The projections $\theta_{\mathrm{XZ}}$ and $\theta_{\mathrm{YZ}}$ on the X-Z and Y-Z planes have a value of the tangent which is proportional to the magnetic field components along Y and X respectively:

$$\tan\theta_{\mathrm{XZ}} = \mu\ B_{\mathrm{Y}}\ , \tag{3.19}$$

$$\tan\theta_{\mathrm{YZ}} = \mu\ B_{\mathrm{X}}\ . \tag{3.20}$$

The proportionality constant is called the *Hall mobility* and its typical value in silicon is $\mu_h \simeq 310$ cm$^2$ V$^{-1}$ s$^{-1}$ and $\mu_e \simeq 1650$ cm$^2$ V$^{-1}$ s$^{-1}$ for holes and electrons respectively [54]. In the case of holes, which are responsible for the formation of the cluster on the X side of the sensor, the drift due to the $B_{\rm X}$ component of the magnetic field can be neglected, since it makes them move in the Y direction along the X strips; conversely, $B_{\rm Y}$ does not affect Y clusters, which are associated to electrons. The correction introduced in the calculation of the value of the coordinates to deal with this systematic effect is a shift of the reconstructed impact point given by:

$$\delta_{\rm X} = d \, \tan\theta_{\rm XZ} = d \, \mu_h \, B_{\rm Y} \, , \tag{3.21}$$

$$\delta_{\rm Y} = d \, \tan\theta_{\rm YZ} = d \, \mu_e \, B_{\rm X} \, , \tag{3.22}$$

where $d = 150$ $\mu$m is half the silicon sensor thickness, and the components of the magnetic field in the impact point are calculated as described in Sec. 3.5.3. With an average value of the magnetic field intensity of about $\langle B \rangle = 0.43$ T, the angle which is obtained in the X-Z projection is less than 1°, which corresponds to a displacement of about 2 $\mu$m.

## 3.5 Deflection measurement

This stage of the data reduction procedure of PAMELA's spectrometer deals with the central issue of obtaining the value of the deflection of the particles which have been recorded for each event, starting from the spatial information about the positions of their impact points on the different planes. This is a quite complex task and several steps are needed in order to accomplish it. The core of the process consists in a fitting and minimizing routine (described in Sec. 3.5.2) which finds the best trajectory passing through the points that have been measured on the silicon planes, using an algorithm which solves the equation of motion of the cosmic ray inside the cavity of the spectrometer. The knowledge of the value of the magnetic field along the path of the particle is needed

in order to do this, and it is obtained from a sampling of the field components (see Sec. 2.4.1) using an interpolation procedure that will be explained in detail in Sec. 3.5.3. A further complication arises when the event does not contain a clear signature of the passage of a single cosmic ray in the tracking system (that is to say, six pairs of X and Y clusters whose positions are well consistent with a physical track). In fact a greater number of clusters could have been identified for the presence of multiple particles in the event[7] or due to spurious noisy strips, and on the other hand possibly some of the real impact points could have not been recorded because of detection inefficiencies of the silicon sensors. In order to cope with such intricate situations a track recognition algorithm has been developed, and it is illustrated in the next section.

### 3.5.1 Track recognition

Before being able to fit a curve through a set of measured experimental points and reconstruct the track of the particle, the clusters and their associated coordinates for the two sides of each plane (which have been determined as in Sec 3.4 and that till now have been treated as independent measurements) have to be paired into a physical point of incidence on that plane. Subsequently, such points will have to be grouped as belonging to the different possible tracks.

#### Cluster charge correlation

If more than one cluster is present both on the X and Y sides of a sensor, there is not a unique way to associate them to a physical impact point, as it can be seen from From Fig. 3.14. Following Ref. [69], the connection between them can be done on the basis of the signals of the clusters, since those generated by the same particle which crosses a sensor are correlated. In fact, when a cosmic ray passes through the silicon layer, electrons and holes are released in pairs by ionization, and consequently

[7] In the majority of cases this is not due to the coincident passage of more than one cosmic ray in the trigger window, which is very unlikely for the acceptance of PAMELA, but to the interaction of a single cosmic ray with the material of the detector.

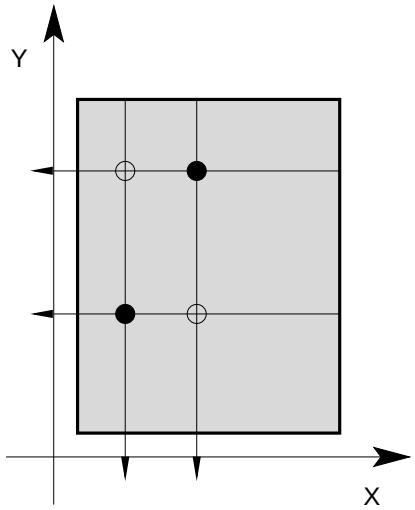


Figure 3.14: *Sketch of a silicon sensor on which two clusters have been identified both on the X and on the Y side. The coordinates reconstructed from the information on the hit strips are represented by the markers on the axes: they can be associated in two different configurations of impact points, indicated by the pairs of open and filled circles.*

the charge collected on the two faces of the double-sided detector should in principle be the same (see also Sec. 2.4.3); on the contrary groups of strips which have been identified as clusters but which are not really due to particles, have in general values of the signal uncorrelated to that of the other ones. Since in practice inefficiencies in charge collection can modify this ideal situation and cause the amount of signal to be possibly different even for the two clusters which have been actually generated by the same physical event, a calibration to establish the optimal cut to be applied in order to perform this X-Y coordinate association has to be done. For this reason, "clean" events are selected (following criteria similar to those applied for calibrating the $\eta$ functions, see Sec. 3.4), and the *charge correlation* between their clusters is analyzed, by plotting their signals $S_{\mathrm{X}}$ and $S_{\mathrm{Y}}$ for each plane. A typical example of the $S_{\mathrm{Y}}$-$S_{\mathrm{X}}$ scatter plot for a set of calibration events is shown in the upper left part

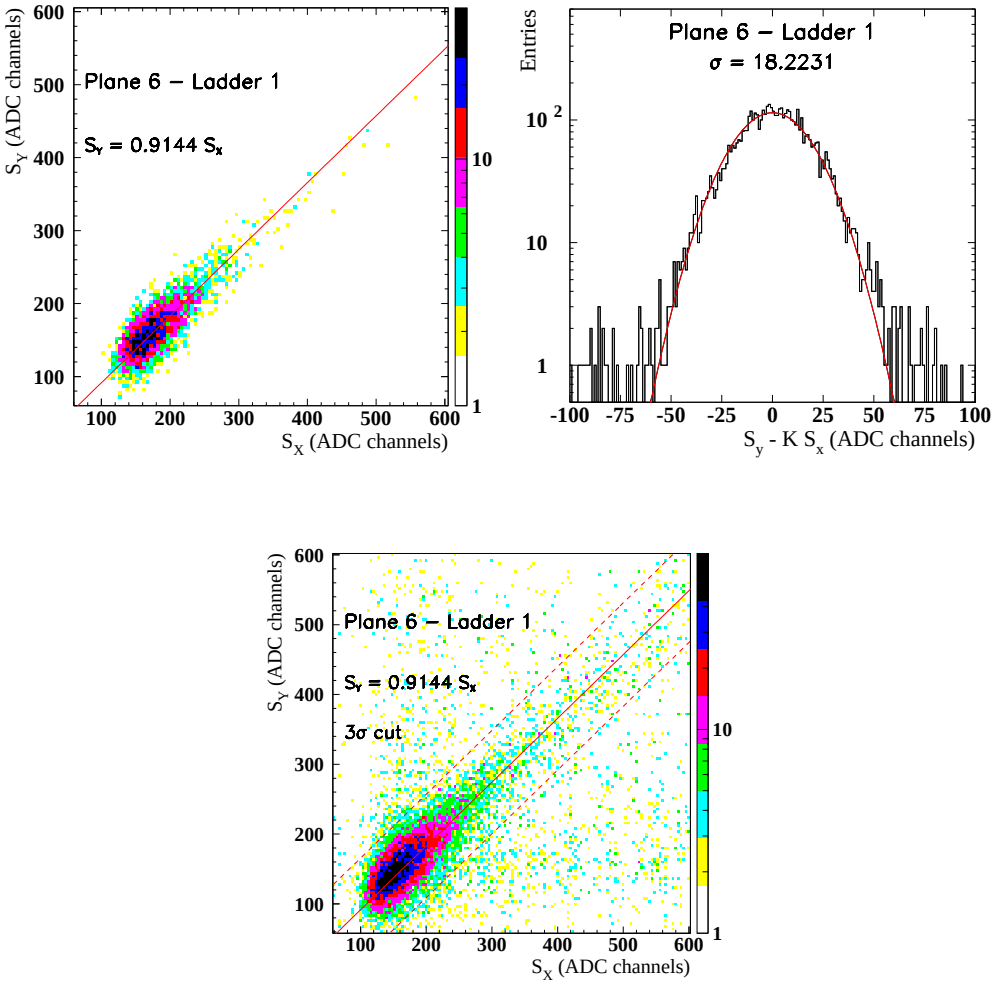


Figure 3.15: *Cluster charge-correlation plots. In the upper part, the scatter plot on the left shows the correlation between the signals of X and Y clusters for the calibration sample and the best fit line, while on the right the distribution of the distances of the points from the line is displayed and fitted with a Gaussian curve. In the lower part, the scatter plot for all the events shows how pairs whose distance from the fit line is lower than 3 times the width of the Gaussian are selected.*

of Fig. 3.15. As it can be seen, the points representing the pairs of signals arrange themselves along the bisector line, showing the correlation between the two sides of the sensor. The best fit line $S_{\rm Y} = K\ S_{\rm X}$ which is drawn over the plot has not actually a slope $K = 1$ because of the slightly different gains for the two electronic amplification chains which read out the two sides. The distance of the points from the line, evaluated as:

$$d \ = \ \frac{|S_{\rm Y} - K\ S_{\rm X}|}{\sqrt{1+K^2}} \ , \tag{3.23}$$

is taken as the parameter to decide which clusters have to be paired. A Gaussian fit such as the one reported in the upper right part of Fig. 3.15 is done on the distribution of the distances $d$ for the calibration sample, and the points that pass the selection are those which lie inside a 3-$\sigma$ region around the best line, as shown in the last plot of the figure. Those points, representing pairs of X and Y clusters which are likely to be due to the same amount of ionization charge, carry both the X and Y coordinate information of an impact point, and for this reason they are called "*couples*" and they will be used in the following track recognition phase. On the contrary, the unpaired clusters which has been excluded by the cut are called "*singles*", since the value of only one coordinate can be extracted from them: they will not be considered at once but will be possibly included only at the end of the track fitting if an impact point is missing on some plane.

A remark has to be done about the ambiguity issue raising because of the way the read-out electrodes are built on the ohmic side of the *ladders*, as explained in Sec. 2.4.3. In principle, the Y coordinate of each reconstructed impact point has an intrinsic indetermination due to the fact that the electronic channels read at the same time the signals coming from both the implanted strips on the two sensors of a *ladder*, which are 7 cm apart. At this stage, for the sake of forming *couples*, each cluster which belongs to the Y side of a plane is considered twice, as if two distinct groups of signals were present in the event. As illustrated in Fig. 3.16, the real combination associated to the physical impact points of the particle is then determined during the reconstruction of the track, since in general if the wrong sensor is chosen the quality of the fit will be

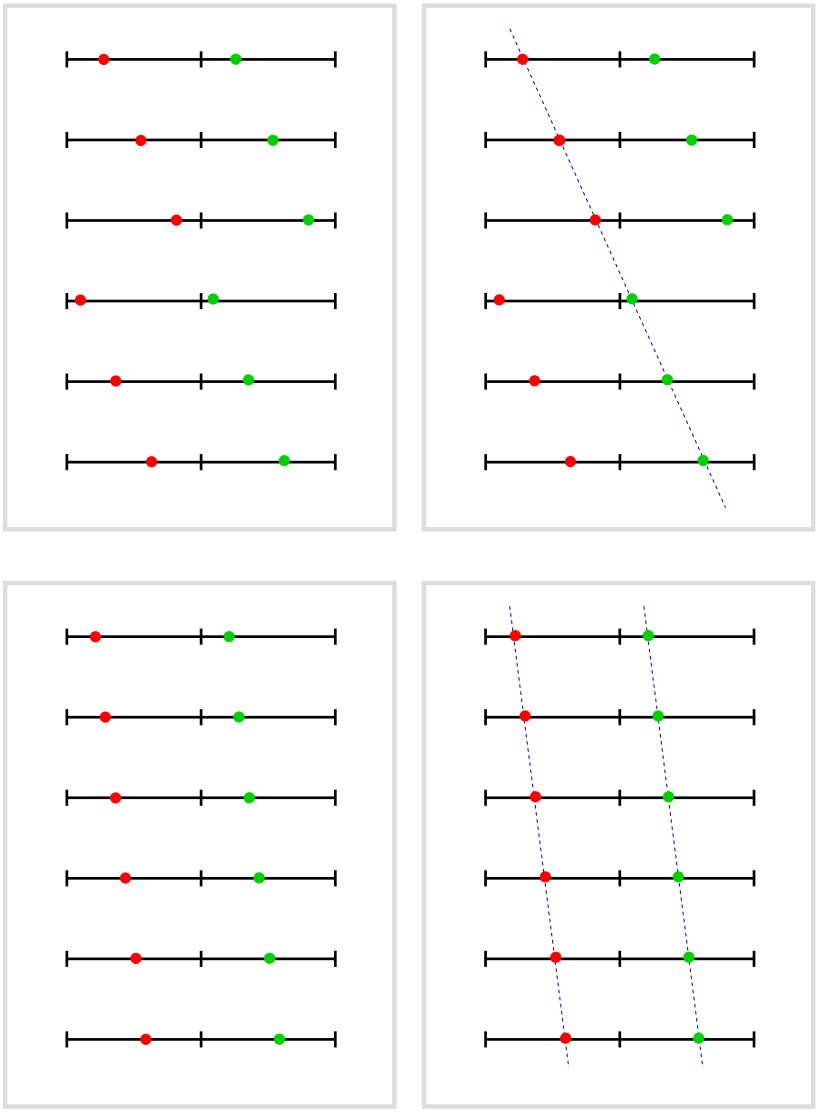

Figure 3.16: *Schematic representation of the Y-Z projection of the spectrometer, showing the ambiguity in the coordinate determination on the Y side of the silicon sensors. Each Y cluster which has been identified is duplicated on both sensors, 7 cm apart (red and green dots in the upper left figure). In most cases the indetermination is resolved as part of the normal process of track fitting, as shown in the upper right figure. In case a track in completely contained in a vertical set of sensors the ambiguity has to be resolved by means of the spatial information coming from the other detectors of PAMELA (lower part of the figure).*

worse. In case a track is completely contained in a vertical set of sensors the spatial information coming from the TOF or from the calorimeter is used in order to resolve the ambiguity.

### Tracker frame of reference and alignment of the sensors

After the *couples* that are present in the event have been identified, their coordinates (which up to this stage were referred to the intrinsic X and Y axes of the sensor they belonged to, defined by the orthogonal directions of the strips on the two sides) have to be expressed in a frame of reference common to all the spectrometer. This is needed since now the information of all the planes has to be merged together to obtain the complete representation of tracks in the three-dimensional space. The chosen reference frame is the one shown in Fig. 3.17, which has its origin at the geometrical center of the magnet, the Z axis pointing upward, the Y axis opposite to the main component of the magnetic field, and the X axis directed consequently to have a right-handed set of coordinates. As a first order of approximation, this change of frame of reference can be done simply through a translation of the coordinates of the impact points, since ideally the 36 silicon sensors which compose the tracking system are arranged in 6 planar configurations of 6 sensors with perfectly aligned strips, and their positions with respect to the origin are known from the mechanical design of the spectrometer. Actually their true positions and orientations in space are not known *a priori*, at least not to the level required in order not to spoil the very high spatial resolution of the detector, which is of few micrometers. Moreover the misalignments from their design configuration could change in time, due for instance to mechanical stresses on the device. For this reason a procedure to determine *a posteriori* the actual positions of the sensors from the analysis of data had to be developed. The detailed discussion of the alignment process which allows to perform the correct transformation of frame of reference from the sensor to the three-dimensional space is reported in Chapter 4.

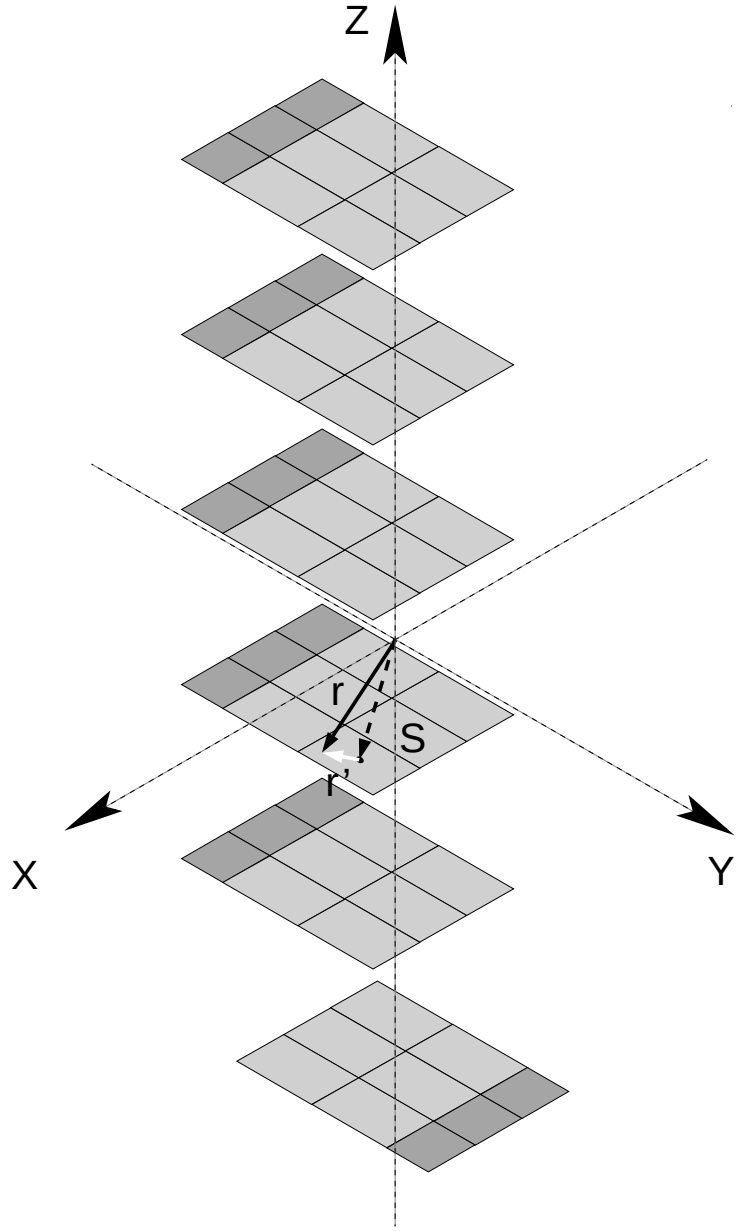


Figure 3.17: *Sketch of the ideal configuration of the tracking system. The silicon sensors are arranged in six planar configurations of six sensors with aligned strips, and their positions with respect to the origin of the coordinate system are known from the mechanical design of the spectrometer. The coordinates of a point on a sensor (represented by the* $\boldsymbol{r}'$ *vector) can be expressed in the general reference frame (as the vector* $\boldsymbol{r}$*) simply through the translation of the point according to the vector* $\boldsymbol{S}$ *which identifies the position of that sensor.*

### Hough transform and track recognition

Once the misalignments of the sensors have been taken into account and the coordinates of the *couples* have been expressed in a general reference frame, the real recognition procedure which groups them into potential tracks can start. The curve which a relativistic charged particle follows while moving in a known magnetic field can be obtained by integrating the equation of motion (2.3) or (2.4) for a given initial condition $(\boldsymbol{r}_0, \boldsymbol{r}_0')$: that is to say, the track of the particle inside the spectrometer is completely defined by a set of six numbers, namely the components of the initial position and velocity vectors. An equivalent choice of the defining parameters that is convenient for our experimental situation consists in considering a reference plane which is crossed by the particle (i.e. fixing a spatial coordinate) and assigning the value of a five-component vector, which is called the *state vector* of the track. In our case the plane is expressed as $z = z^* = const$ and is placed above the spectrometer, and the chosen state vector is:

$$\boldsymbol{\alpha} \;=\; (x^*, y^*, \sin\theta^*, \varphi^*, \eta)\;, \tag{3.24}$$

where $(x^*, y^*)$ are the coordinates of the intersection point of the track on the reference plane, $\theta^*$ and $\varphi^*$ the polar incidence angles, and $\eta$ the magnetic deflection of the particle. A certain vector $\boldsymbol{\alpha}$ corresponds to one and only one trajectory of the cosmic ray in the magnetic field, and thus the track reconstruction process reduces to finding the state vector which results in the curve which best approximates the experimental points on the silicon planes of the spectrometer. The complete fitting procedure will be explained in detail in Sec. 3.5.2: the task of the recognition phase is to identify all the possible tracks of particles in an event and to provide an initial estimate for their state vectors, which will be used as a starting point for the fitting.

At this stage, for the purpose of determining the starting value of $\boldsymbol{\alpha}$, the simplifying hypothesis of a uniform magnetic field along the Y direction is done, and consequently the approximation that trajectories of particles have a straight line as their projection on the Y-Z plane

and an arc of circumference on the X-Z plane. This, while not being very far from reality (cf. Sec. 2.4.1), allows to reduce the computation time during track recognition: in the subsequent fitting phase the real value and shape of the $\boldsymbol{B}$ field will be employed instead. The analysis is carried on independently for the X-Z and Y-Z projections using an algorithm based on a combinatorial implementation of the so-called method of the *Hough transform* [70]. The Hough transform is a general feature-extraction technique which allows to detect and isolate a pattern or a shape in a complex arrangement of objects: it was developed at first as a way to help detecting particle tracks in bubble chambers, and it is now widely employed in digital image processing too. Here it is used to recognize all the possible straight lines and circumferences that can be associated reasonably well to Y and X clusters generated by a cosmic ray. In this way, two of the five track-defining elements are extracted from the parameters of the line and the remaining three from those of the circle, and the complete vector $\boldsymbol{\alpha}$ is obtained from a suitable combination of them.

Since in the Y-Z projection the sets of clusters which can potentially belong to a physical track are expected to lie on a line $y = mz + q$, the Y coordinate of the $i$-th *couple* of the event and the Z coordinate associated to the plane where it is located are linked by the relation:

$$y_i \;=\; mz_i \;+\; q \;, \tag{3.25}$$

if the correct values of the parameters $m$ and $q$ are chosen. Inverting the role of the involved quantities, this expression can be regarded as a relation between $m$ and $q$:

$$q \;=\; -z_i m \;+\; y_i \;, \tag{3.26}$$

that for the given $i$-th *couple* represents a line in the $(m, q)$ plane, which is called the *Hough* or *parameter space*. As the slope $m$ and the $y$-intercept $q$ vary in the parameter space, all the possible lines which pass through the point $(z_i, y_i)$ in the Y-Z projection of real space are obtained. So,

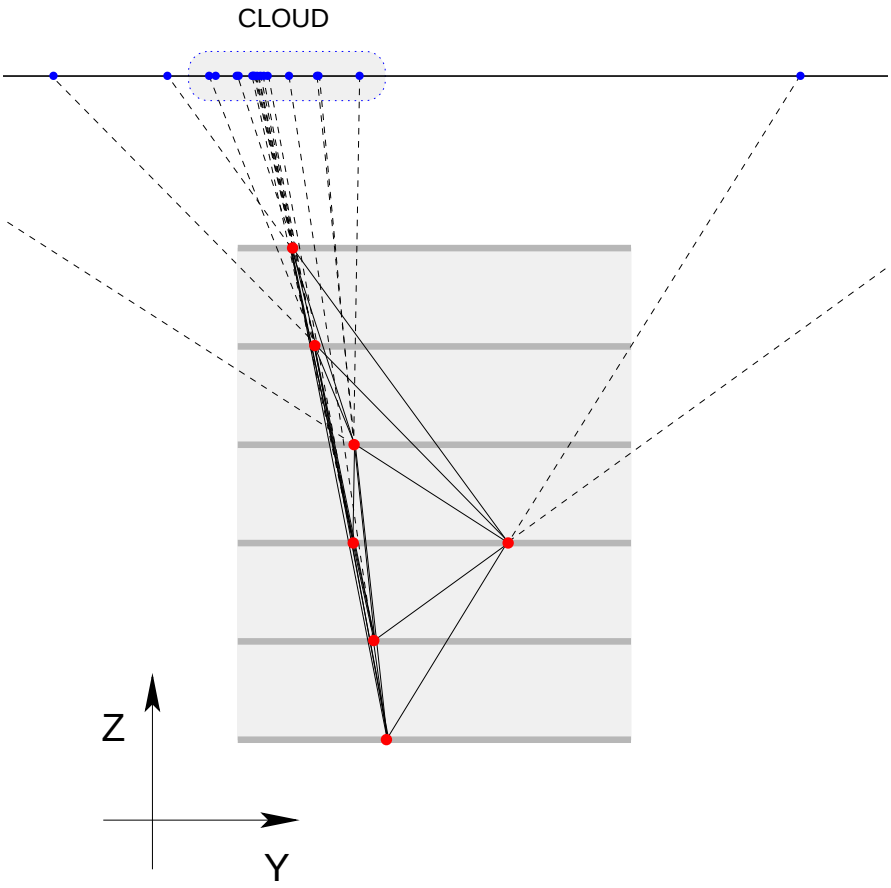


Figure 3.18: *Schematic representation of the Y-Z projection of the tracking system, which shows the principle at the basis of the combinatorial implementation of the Hough-transform algorithm. Seven points have been measures, and are represented by red dots. The straight segments which connect each combination of two points belonging to different planes are drawn: their extensions tend to have the same m and q if the points belong to the same real physical track. The two parameters of the state vector which are obtained from the analysis of the Y-Z projection are the y-intercept $y^*$ on the reference plane placed above the spectrometer and the intersection angle $\theta^*_Y$. The points in the parameter space which correspond to a track are grouped in a so-called* cloud.

since each cluster in real space is transformed into a curve, if the process is repeated for other physical points which in an ideal case lie on a straight line, the different curves in Hough space will actually intersect in a certain position which corresponds to the parameters of that line. Conversely, if the clusters do not belong to a real track the intersection points in Hough space will be scattered around. In the realistic case of the impact points generated on the detecting planes of the spectrometer by a cosmic ray, a precise intersection will not be obtained, since they will not be exactly collinear, but the curves in Hough space will gather around the ideal track parameters nevertheless.

An alternative approach to the method of the Hough transform consists in picking in turn each possible pair $(i, j)$ of Y clusters belonging to different planes and in calculating the intersection point $(m, q)$ of their transformed curves. This means that the linear system:

$$\begin{cases} q = -z_i m + y_i \\ q = -z_j m + y_j \end{cases} \tag{3.27}$$

has to be solved for every two *couples* in the event: this implementation of the algorithm is equivalent to that described above and is the one which has been chosen. The sets of points that represent the slopes and the $y$-intercepts of all the possible straight lines connecting the clusters will in general be scattered in the parameter space, but some will group together if any track can be identified among them: the gathering points represent the initial guesses which will have to be used (for the two parameters which can be extracted from the Y-Z projection) when fitting those tracks. A schematic representation of the principle of this technique is depicted in Fig. 3.18.

A similar method is used in the X-Z projection, but since there the expected curve in real space is a circumference, the coordinates of the X clusters of three *couples* $(i, j, k)$ are needed in order to determine its center $(z_c, x_c)$ and radius $r$, and in this case the Hough space is no more a plane but has three dimensions, consequently. The system of equations that has to be solved is:

$$\begin{cases} (z_c - z_i)^2 + (x_c - x_i)^2 - r^2 = 0 \\ (z_c - z_j)^2 + (x_c - x_j)^2 - r^2 = 0 \\ (z_c - z_k)^2 + (x_c - x_k)^2 - r^2 = 0 \end{cases} \tag{3.28}$$

and the intersection of the three surfaces to which the X clusters correspond in the $(z_c, x_c, r)$ space gives the required circumference.

For the practical implementation of the algorithm, on the Y-Z plane the *couples* that have been identified in the event are associated in pairs $(i, j)$, which are called "*doublets*", and for each of them the system (3.27) is solved by computing the equation of the straight line which connects them:

$$\frac{y - y_i}{y_j - y_i} = \frac{x - x_i}{x_j - x_i} \,. \tag{3.29}$$

The resulting parameters $(m, q)$ are then expressed as the vector:

$$\boldsymbol{\alpha}_{\mathrm{Y}} = (y^*, \tan\theta^*_{\mathrm{Y}}) \,, \tag{3.30}$$

where $y^*$ is the intersection of the track with the reference plane and $\theta^*_{\mathrm{Y}}$ is the angle which it forms with the Z axis. Similarly, on the X-Z projection, *couples* are grouped in "*triplets*" $(i, j, k)$ and the solution of the system (3.28) is found by determining the equation of the circumference that passes through them:

$$\begin{vmatrix} z^2 + x^2 & z & x & 1 \\ z_i^2 + x_i^2 & z_i & x_i & 1 \\ z_j^2 + x_j^2 & z_j & x_j & 1 \\ z_k^2 + x_k^2 & z_k & x_k & 1 \end{vmatrix} = 0 \,. \tag{3.31}$$

The three parameters $(z_c, x_c, r)$ that are obtained in this way correspond to a vector:

$$\boldsymbol{\alpha}_{\mathrm{X}} = (x^*, \tan\theta^*_{\mathrm{X}}, k) \,, \tag{3.32}$$

which contains the intersection $x^*$ with the reference plane, the angle $\theta^*_{\rm X}$ between the tangent line and the Z axis, and the curvature $k = 1/r$.

Not all the accumulation areas in Hough space are taken as reliable estimates of the parameters of possible tracks. A first selection is performed by requiring that each point in a group is closer than a given threshold from at least another one. The calibration used to find the optimal value for this cut consists in an analysis of the distribution of the reciprocal distances for a sample of "clean" events like those used to calibrate the cuts on the charge correlation between X and Y clusters. A group of points in the parameter space fulfilling this requisite is called a "*cloud*" (see also Fig. 3.18). As a further selection, *clouds* are discarded if they contain a too low number of points, that is to say if the combinations of clusters on different planes in real space that have similar values of the parameters are not sufficient to give a reliable estimate of the track. Since the purpose of these discriminations is not that of obtaining an accurate value of the state vector but just a first estimate for all the possible tracks, cuts are chosen to be not extremely strict, in this way maximizing the number of trajectories that can be recognized.

For each selected *cloud*, the value of the corresponding vector $\boldsymbol{\alpha}_{\rm X}$ or $\boldsymbol{\alpha}_{\rm Y}$ is calculated as the average on the points that it contains. By merging the information which comes from any combination of X and Y *clouds* with a sufficient number of points in the two projections of the track, a so-called "*track candidate*" is obtained. The estimate of its 5-component state vector (defined in Eq. (3.24)) to be used as a first guess in the fit, is derived directly from the quantities expressed above in Eq. (3.30) and (3.32) by using the following relations between their components:

$$\begin{cases} \varphi^* \;=\; \arctan\left(-\,\dfrac{\tan\theta^*_{\rm Y}}{\tan\theta^*_{\rm X}}\right) \\ \sin\theta^* \;=\; \dfrac{\tan\theta^*}{\sqrt{1+\tan^2\theta^*}}\,, \qquad \text{where} \quad \tan\theta^* \;=\; -\,\dfrac{\tan\theta^*_{\rm X}}{\cos\varphi^*} \\ \eta \;=\; \dfrac{k}{0.3\,\langle B\rangle} \end{cases} \tag{3.33}$$

where the last equality comes from Eq. (2.6) and (2.1). The track candidate is used in the fitting procedure (described later in Sec. 3.5.2), and an improved value of the state vector, that corresponds to a trajectory which better approximates the experimental impact points, is searched for: as a result of the procedure a $\chi^2$ estimator of the goodness of the fit for each candidate is found too.

When this procedure has been applied to all the possible combinations of X-Z and Y-Z *clouds* of the event, the track that has the best $\chi^2$ is analyzed to check if impact points are missing on some plane of the spectrometer and, in case, if some of the unused points can be included in the track. The points to be included are at first looked for among the other *couples* of the event. Then the pairs of clusters which form them are separated again, united to the pool of *singles* (i.e. the clusters on any side of a sensor which could not have been associated to a corresponding one on the other X or Y side), and the check is repeated for them. The decision whether or not to include a *couple* or a *single* depends on their distance from the point which is expected on that plane on the basis of the fit. Once the best-$\chi^2$ track has been completed or no more *singles* are available, it is taken as a real physical trajectory of a cosmic ray, and the clusters that it contains (and which cannot therefore belong to any other track candidate) are excluded from further analysis. The other candidates formed by *clouds* for which the requirements about the minimum number of points is still valid, go through a similar process, and finally a group of recognized tracks and of unassigned clusters are found as a result.

A graphical representation of events after the track reconstruction is reported in Fig. 3.19. The upper part shows an event where a single cosmic ray is present. The points on the two projections has been correctly associated in *couples* and grouped in *clouds* which represent the physical trajectory of the particle. The track which results from the fitting algorithm is drawn as well. The white dot on one of the X sides has been discarded and remains as an unassigned *single*, probably a cluster due to noise which has passed the identification threshold. The calculated rigidity of the particle is 3.49 GV/$c$ and the reduced $\chi^2$ of the fit is about 6.

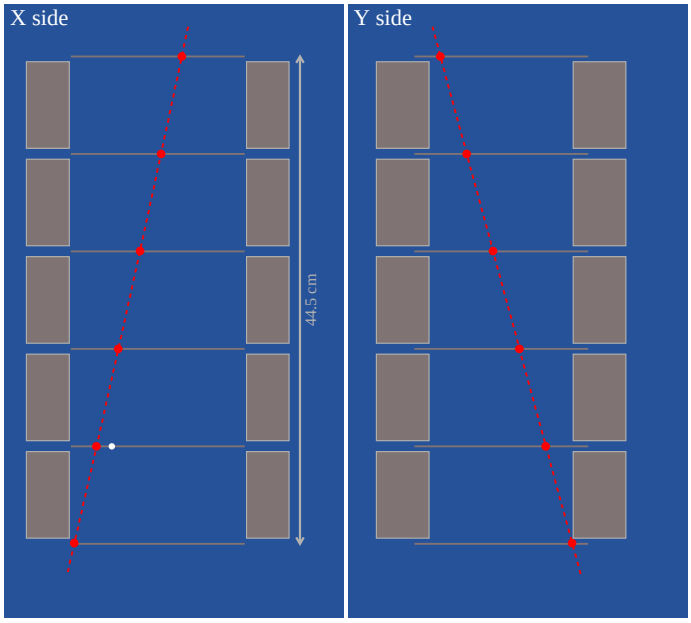


Date 2005 File 050220_001 Event 1180

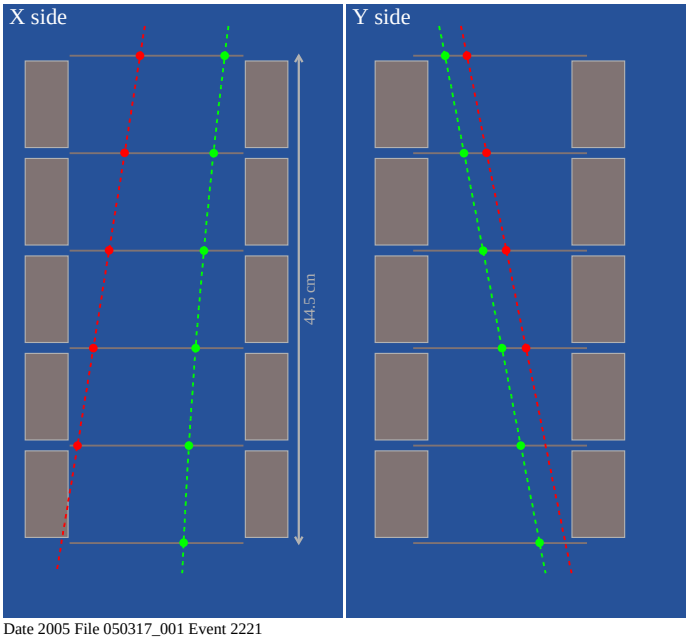


Date 2005 File 050317_001 Event 2221

Figure 3.19: *Representation of reconstructed events in the spectrometer: in the upper part of the figure, a single-track event which contains a spurious cluster; in the lower part, a double-track event in which all the clusters have been correctly associated to the two cosmic rays. The reconstructed rigidity (with its sign corresponding to the particle charge) and the reduced $\chi^2$ of the fit are reported too.*

On the contrary, the lower part of Fig. 3.19 shows a more complex event where two cosmic rays have been detected. Two tracks have been identified and all the measured points have been correctly associated. While the green track is completely contained in the spectrometer, by looking at the X-Z projection it can be seen that the red one represents a cosmic ray which hit the lowest block of the magnetic cavity: for this reason there is no impact point on the bottom plane of the tracker, while on the contrary the missing Y cluster on the previous plane is probably due to a detection inefficiency of the silicon sensor. In spite of this, the X *single* has been correctly included in the track. The rigidities of these two cosmic rays are 8.22 GV/$c$ and 0.825 GV/$c$ (the sign of $R$ for the green track shows that the particle has a negative electric charge), while the reduced $\chi^2$ of the fit are about 1 and 10, respectively. The high values of the $\chi^2$ for low energy particles is due to the fact that a complete treatment of the uncertainty of the measured coordinates which takes into account the effect of multiple scattering has not been yet implemented in the fit, and a simple constant value for the resolution is used (see also next Sec. 3.5.2).

### 3.5.2 Track fitting

The track fitting algorithm is used to determine the state vector that corresponds to the trajectory which gives the best approximation of the experimental impact points on the silicon detecting planes. For a certain set of initial conditions, which are provided by means of the value that the state vector:

$$\boldsymbol{\alpha} \;=\; (x^*, y^*, \sin\theta^*, \varphi^*, \eta) \tag{3.34}$$

takes on a reference plane $z = z^* = const$, the equations of motion of a charged particle in the magnetic field $\boldsymbol{B}$, expressed as:

$$\frac{\mathrm{d}^2\boldsymbol{r}}{\mathrm{d}l^2} \;=\; \eta\left(\frac{\mathrm{d}\boldsymbol{r}}{\mathrm{d}l}\times\boldsymbol{B}\right)\;, \tag{3.35}$$

are solved, and the trajectory is found. The impact points which are obtained from the intersection between the trajectory and the planes of the spectrometer are then compared with the measured ones: a $\chi^2$-function which states how much the fit differs from the actual physical track is built, and new values of the initial conditions of integration, that result in impact points nearer to the experimental ones, are extracted from it. This procedure is iterated until convergence of the initial conditions of integration. The first guess of the state vector, in the case of the track fitting which is performed during the determination of the deflection of the recognized tracks, comes from the analysis by means of the Hough transform which has been described in the previous Sec. 3.5.1. The solution of Eq. (3.35) is found by using Nyström algorithm [71], which is based on the stepwise numerical integration of the equations with the Runge-Kutta method, as it has been coded in FORTRAN in the CERN software libraries [60]. This method allows to obtain the trajectory starting directly from the system of second-order differential equations of motion without the need of the intermediate step of reducing them to a first-order system, in this way improving the computational efficiency. Whereas during the track-recognition phase a simplified magnetic configuration has been employed, here the real $\boldsymbol{B}$ field is used. Its value, which is needed in each step of the integration, is extracted from the measured values following the procedure explained in Sec. 3.5.3.

The function from which a better estimate of the state vector is calculated at each iteration is:

$$\chi^2(\boldsymbol{\alpha}) \;=\; \sum_{i}^{N} \left[ \left( \frac{x_i - \tilde{x}_i(\boldsymbol{\alpha})}{\sigma_{x_i}} \right)^2 + \left( \frac{y_i - \tilde{y}_i(\boldsymbol{\alpha})}{\sigma_{y_i}} \right)^2 \right] , \tag{3.36}$$

where $(x_i, y_i)$ represents the measured point on the $i$-th plane, $\sigma_{x_i}$ and $\sigma_{y_i}$ its uncertainties, $(\tilde{x}_i, \tilde{y}_i)$ the coordinates obtained from the fit for a certain $\boldsymbol{\alpha}$, and the sum includes the planes on which an impact point has been identified. A constant value is used for the errors on the measure of the spatial coordinates: a more sophisticated analysis which takes into account the degradation of the resolution due to the multiple scattering

of particles in the silicon planes, and also the intrinsically greater indetermination of the impact point associated to high-multiplicity clusters is in progress. A refined value of the $\chi^2$, which results in reconstructed coordinates nearer to the experimental ones, can be obtained by minimizing the $\chi^2$ as a function of the components of $\boldsymbol{\alpha}$ [72]:

$$\frac{\partial}{\partial \alpha_k}\left(\chi^2(\boldsymbol{\alpha})\right) \;=\; 0\,, \qquad k \;=\; 1\ldots 5\,. \tag{3.37}$$

Starting from the $\chi^2$ evaluated for a given initial guess $\boldsymbol{\alpha}_0$, the function at a nearby value $\boldsymbol{\alpha} = \boldsymbol{\alpha}_0 + \Delta\boldsymbol{\alpha}$ is obtained by means of a second-order Taylor series expansion:

$$\chi^2(\boldsymbol{\alpha}) \;\simeq\; \chi^2(\boldsymbol{\alpha}_0) + \sum_{h=1}^{5} \left.\frac{\partial \chi^2}{\partial \alpha_h}\right|_{\boldsymbol{\alpha}_0} \Delta\alpha_h + \frac{1}{2}\sum_{h,l=1}^{5} \left.\frac{\partial^2 \chi^2}{\partial \alpha_h \partial \alpha_l}\right|_{\boldsymbol{\alpha}_0} \Delta\alpha_h \Delta\alpha_l\,, \tag{3.38}$$

in which the sums are on the five components of the $\boldsymbol{\alpha}$ vector. When this expression replaces $\chi^2(\boldsymbol{\alpha})$ in the minimization conditions (3.37), it gives:

$$0 + \sum_{h=1}^{5} \left.\frac{\partial \chi^2}{\partial \alpha_h}\right|_{\boldsymbol{\alpha}_0} \frac{\partial \Delta\alpha_h}{\partial \alpha_k} + \frac{1}{2}\sum_{h,l=1}^{5} \left.\frac{\partial^2 \chi^2}{\partial \alpha_h \partial \alpha_l}\right|_{\boldsymbol{\alpha}_0} \frac{\partial}{\partial \alpha_k}\left(\Delta\alpha_h \Delta\alpha_l\right) \;\simeq\; 0 \tag{3.39}$$

with $k = 1\ldots 5$. Now, since:

$$\frac{\partial \Delta\alpha_h}{\partial \alpha_k} \;=\; \delta_{hk}\,, \tag{3.40}$$

where $\delta_{hk}$ is the Kronecker delta, Eq. (3.39) becomes:

$$\left.\frac{\partial \chi^2}{\partial \alpha_k}\right|_{\boldsymbol{\alpha}_0} + \sum_{h=1}^{5} \left.\frac{\partial^2 \chi^2}{\partial \alpha_h \partial \alpha_k}\right|_{\boldsymbol{\alpha}_0} \Delta\alpha_h \;\simeq\; 0\,, \qquad k \;=\; 1\ldots 5\,. \tag{3.41}$$

By introducing the first-derivative vector $\boldsymbol{V}$ and the second-derivative matrix $\mathsf{Z}$, both calculated in $\boldsymbol{\alpha}_0$:

| $k$ | $\alpha_k$ | $\dfrac{\partial \tilde{x}_i}{\partial \alpha_k}$ | $\dfrac{\partial \tilde{y}_i}{\partial \alpha_k}$ |
|---|---|---|---|
| 1 | $x^*$ | 1 | 0 |
| 2 | $y^*$ | 0 | 1 |
| 3 | $\sin\theta^*$ | $(z_i - z_0)\cos\alpha_4 \dfrac{1}{\left(\sqrt{1-\alpha_3^2}\right)^3}$ | $(z_i - z_0)\sin\alpha_4 \dfrac{1}{\left(\sqrt{1-\alpha_3^2}\right)^3}$ |
| 4 | $\varphi^*$ | $-(z_i - z_0)\sin\alpha_4 \dfrac{\alpha_3}{\sqrt{1-\alpha_3^2}}$ | $(z_i - z_0)\cos\alpha_4 \dfrac{\alpha_3}{\sqrt{1-\alpha_3^2}}$ |
| 5 | $\eta$ | $\dfrac{1}{\alpha_5}\left[\tilde{x}_i - \left(\alpha_1 + (z_i - z_0)\cos\alpha_4 \dfrac{\alpha_3}{\sqrt{1-\alpha_3^2}}\right)\right]$ | $\dfrac{1}{\alpha_5}\left[\tilde{y}_i - \left(\alpha_2 + (z_i - z_0)\sin\alpha_4 \dfrac{\alpha_3}{\sqrt{1-\alpha_3^2}}\right)\right]$ |

Table 3.1: *Partial first derivatives of the reconstructed coordinates with respect to* $\boldsymbol{\alpha}$.

$$
\begin{aligned}
(\boldsymbol{V})_k &= \left.\frac{\partial \chi^2}{\partial \alpha_k}\right|_{\boldsymbol{\alpha}_0}, \\
(\mathsf{Z})_{h,k} &= \left.\frac{\partial^2 \chi^2}{\partial \alpha_h \partial \alpha_k}\right|_{\boldsymbol{\alpha}_0},
\end{aligned}
\tag{3.42}
$$

Eq. (3.41) can be rewritten as:

$$
\boldsymbol{V} \; + \; \mathsf{Z}\,(\boldsymbol{\alpha} - \boldsymbol{\alpha}_0) \; \simeq \; 0\,, \tag{3.43}
$$

and the improved vector is:

$$
\boldsymbol{\alpha} \; \simeq \; \boldsymbol{\alpha}_0 \; - \; \mathsf{Z}^{-1}\,\boldsymbol{V}\,. \tag{3.44}
$$

This value of the state vector is used as a new set of initial conditions for integrating Eq. (3.35), and the procedure is repeated until the desired degree of convergence is reached. The full expressions of $\boldsymbol{V}$ and $\mathsf{Z}$, obtained from Eq. (3.36), are:

$$(\boldsymbol{V})_k = 2\left[\sum_i^N \left(\frac{x_i - \tilde{x}_i}{\sigma_{x_i}^2}\right) \left.\frac{\partial \tilde{x}_i}{\partial \alpha_k}\right|_{\boldsymbol{\alpha}_0} + \sum_i^N \left(\frac{y_i - \tilde{y}_i}{\sigma_{y_i}^2}\right) \left.\frac{\partial \tilde{y}_i}{\partial \alpha_k}\right|_{\boldsymbol{\alpha}_0}\right], \quad (3.45)$$

$$\begin{aligned}(\mathsf{Z})_{h,k} = {} & 2\sum_i^N \frac{1}{\sigma_{x_i}^2}\left[\left.\frac{\partial \tilde{x}_i}{\partial \alpha_h}\right|_{\boldsymbol{\alpha}_0} \left.\frac{\partial \tilde{x}_i}{\partial \alpha_k}\right|_{\boldsymbol{\alpha}_0} + (x_i - \tilde{x}_i) \left.\frac{\partial^2 \tilde{x}_i}{\partial \alpha_h \partial \alpha_k}\right|_{\boldsymbol{\alpha}_0}\right] + \\ & + 2\sum_i^N \frac{1}{\sigma_{y_i}^2}\left[\left.\frac{\partial \tilde{y}_i}{\partial \alpha_h}\right|_{\boldsymbol{\alpha}_0} \left.\frac{\partial \tilde{y}_i}{\partial \alpha_k}\right|_{\boldsymbol{\alpha}_0} + (y_i - \tilde{y}_i) \left.\frac{\partial^2 \tilde{y}_i}{\partial \alpha_h \partial \alpha_k}\right|_{\boldsymbol{\alpha}_0}\right]. \quad (3.46)\end{aligned}$$

The second derivatives that appear in the expression above are neglected, while first derivatives are calculated at first order directly from the definition (3.34) of $\boldsymbol{\alpha}$, and are reported in Tab. 3.1.

### 3.5.3 Magnetic field interpolation

The knowledge of the magnetic field along the path of particles crossing the spectrometer is needed during data reduction, both to account for the effect of the Lorentz force in the silicon sensors in order to correct the coordinates of the impact points (Sec. 3.4), and to reconstruct tracks (Sec. 3.5.2). A measure of the components of the field is available on a three-dimensional grid, with a pitch of 5 mm (see Sec. 2.4.1). To obtain $\boldsymbol{B}$ in a generic point of space, a three-dimensional linear interpolation of the sampled values is performed.

With reference to Fig. 3.20, if $P = (x, y, z)$ is the point where the knowledge of $\boldsymbol{B}$ is required, the smallest cubic cell of the grid which contains it, and which is identified by its eight vertexes $P_i$, $i = 1 \ldots 8$, is considered. For each of the field components $B_l$, $l = \mathrm{X}, \mathrm{Y}, \mathrm{Z}$, a series of linear interpolations is done along the three orthogonal axis of the reference frame. First, the value in $P_{12}$ is calculated from the experimental

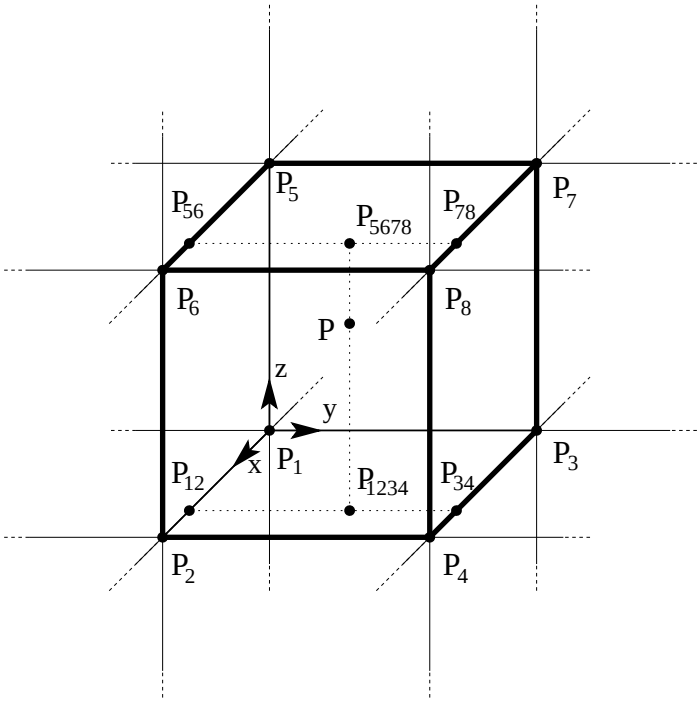


Figure 3.20: *Three-dimensional cell used for interpolating the magnetic field in a generic point $P$. The eight nearest vertexes of the sampling grid $P_i$ are shown, as well as the intermediate interpolation points $P_{ij}$ and $P_{ijhk}$.*

measurements in $P_1 = (x_d, y_d, z_d)$ and $P_2 = (x_u, y_d, z_d)$:

$$\begin{aligned} \widetilde{B}_l(P_{12}) &= B_l(P_1) + \frac{B_l(P_2) - B_l(P_1)}{x_u - x_d}\,(x - x_d) = \\ &= (1-s)\; B_l(P_1) \;+\; s\; B_l(P_2)\;, \end{aligned} \tag{3.47}$$

where $\widetilde{B}_l$ represents the interpolated field and $s$ is a reduced coordinate varying in the interval $[x_d, x_u]$, defined by:

$$s \;=\; \frac{x - x_d}{x_u - x_d}\;. \tag{3.48}$$

Then the same procedure is repeated between $P_3 = (x_d, y_u, z_d)$ and $P_4 = (x_u, y_u, z_d)$, and also for the two remaining couples of vertexes $P_5, P_6$ and $P_7, P_8$, in this way ending the four interpolations along the X direction and obtaining $\widetilde{B}_l(P_{34})$, $\widetilde{B}_l(P_{56})$ and $\widetilde{B}_l(P_{78})$. These values are in turn interpolated along the Y axis, obtaining:

$$\widetilde{B}_l(P_{1234}) \;=\; (1-t)\; B_l(P_{12}) \;+\; t\; B_l(P_{34})\;, \tag{3.49}$$

and $\widetilde{B}_l(P_{5678})$ in a similar way. Here $t$ is a reduced variable for the Y coordinate, analogous to $s$. Finally a last interpolation is performed along Z to find $\widetilde{B}_l(P)$. The complete algorithm can be summarized in the following expression:

$$\begin{aligned}
\widetilde{B}_l(P) \;=\;& (1-s)\,(1-t)\,(1-w)\; B_l(P_1) \;+\; s\,(1-t)\,(1-w)\; B_l(P_2) \;+ \\
+\;& (1-s)\,t\,(1-w)\; B_l(P_3) \;+\; s\,t\,(1-w)\; B_l(P_4) \;+ \\
+\;& (1-s)\,(1-t)\,w\; B_l(P_5) \;+\; s\,(1-t)\,w\; B_l(P_6) \;+ \\
+\;& (1-s)\,t\,w\; B_l(P_7) \;+\; s\,t\,w\; B_l(P_8)\;,
\end{aligned} \tag{3.50}$$

where the three reduced coordinates are:

$$s \;=\; \frac{x - x_d}{x_u - x_d}\,, \qquad t \;=\; \frac{y - y_d}{y_u - y_d}\,, \qquad w \;=\; \frac{z - z_d}{z_u - z_d}\,. \tag{3.51}$$

The same technique is used as well to get the value of the magnetic field intensity in any point of the PAMELA instrument. The interpolation is applied to experimental measurements of the $\boldsymbol{B}$ field components taken outside the cavity of the spectrometer, in this way allowing to extend the reconstructed particle trajectory to the regions where the other detectors are placed.

# Chapter 4

# Alignment of the tracking system

*The determination of the deflection of charged particles with the spectrometer of PAMELA is based on the reconstruction of the trajectory that they follow while crossing the detecting planes located inside the magnetic cavity. Hence it is very important to be able to measure with small uncertainties the coordinates of the impact points on the silicon sensors which compose the tracking system. The procedure described in Sec. 3.4 allows to accomplish this task and to obtain a very high spatial resolution, better than 3 $\mu$m on the bending plane for perpendicularly incident cosmic rays. Nonetheless, at the same time such an high resolution in identifying the impact points is not really useful at all in measuring particle deflection if the mutual positions of the silicon sensors are not known, since for fitting the track the information coming from all the planes has to be put together. As stated in Sec. 3.5.1, during the procedure of track recognition and fitting, the coordinates of the clusters as measured on the sensor they belong to, have to be expressed in a general frame of reference, common to the whole spectrometer. In this chapter, the method which has been developed to determine the correct transformation of reference frame is described.*

## 4.1 The misalignment problem

The nominal positions of the 36 sensors of the tracking system, with respect to the center of the magnet, is known from the mechanical design of the spectrometer. According to this ideal configuration, the couple of detectors which form a *ladder* should be connected together in such a way that they lie on the same plane and that the corresponding strips are parallel and aligned, and the same should be true for the three *ladders* of a plane. Likewise, the six planes should stand one parallel to each other and with aligned strips. If this were the true configuration, the impact point coordinates on a given sensor could be related to the general spectrometer's reference frame simply by a translation. This transformation would in this case be associated to the known vector which identifies the center of the sensor with respect to the origin of coordinates. The situation is represented in Fig. 3.17. Actually in reality the positions of the detectors differ from those of the mechanical design, so that this simple transformation has to be completed with additional corrective terms. Since the coordinates of the impact points can be measured with a resolution of some micrometers, misalignments have to be corrected with an accuracy of that order of magnitude or better, if systematic errors in deflection measurements at high energies are to be avoided. This translates in the arduous task of determining with an uncertainty of the order of 1 $\mu$m the positions of the 36 sensors of the spectrometer, whose mutual distances are of some tens of centimeters.

This requirement has to be compared with the mechanical tolerances in constructing the aluminium structures that contain the magnetic blocks and that support the tracking system planes, which are of the order of tens of micrometers. Moreover, other displacements and rotations are necessarily introduced during the assembly phase, as well as a consequence of shocks and vibrations which can possibly occur during the transport of the instrument, and mainly during the launch of the rocket which will put the satellite into orbit: the combined result of all these effects can possibly amount to hundreds of micrometers. To account for the launch-phase, the calibration needed to obtain the parameters which are used to correct for the misalignments will have to be done in flight. A

further complication arises since the tracking system lies inside the magnetic field generated by a permanent magnet: the unavoidable presence of the field prevents standard methods for aligning the system, such as the use of straight trajectories of particles, from being useful.

A technique has been developed, to determine the alignment parameters from a set of curved tracks of charged particles inside the magnetic field. As it will be explained later, the deflection of the particles has to be known in order to do this. A first set of alignment parameters has been obtained from data taken during a test session on a particle beam at CERN SPS in 2003 (see Sec. 4.2), and in this case the knowledge of the momentum of particles came directly from the machine parameters. The complete alignment of the tracking system has been then performed by integrating this calibration (after correcting it as described in Sec. 4.4) with another one which has been done using tracks of cosmic rays gathered at ground level in Rome in the first months of 2005 (see Sec. 4.3). The parameters which results from this procedure will be used as an initial set for data acquired in flight by PAMELA. Afterwards the procedure will be repeated periodically in order to account for the possible further misalignments which may occur in the launch of the satellite or during its lifetime: tracks of electrons whose energy has been measured by the calorimeter will be used for this task (see Sec. 4.5).

## 4.2 Single-tower alignment

The real position and orientation in three-dimensional space of each silicon sensor in PAMELA's reference frame, can be unambiguously defined by a set of six numbers, which represent the components of a vector of translation and three angles of rotations respect to the ideal configuration given by the mechanical design of the instrument[1]. The convention which has been chosen to specify this transformation of frame of reference, consists in using in turn the rotations $\omega$, $\gamma$ and $\beta$ along the Z, Y and X orthogonal coordinate axes passing through the center of the ideal

[1]For the sake of the alignment, each sensor is considered as a perfectly rigid body with the shape of a rectangular parallelepiped.

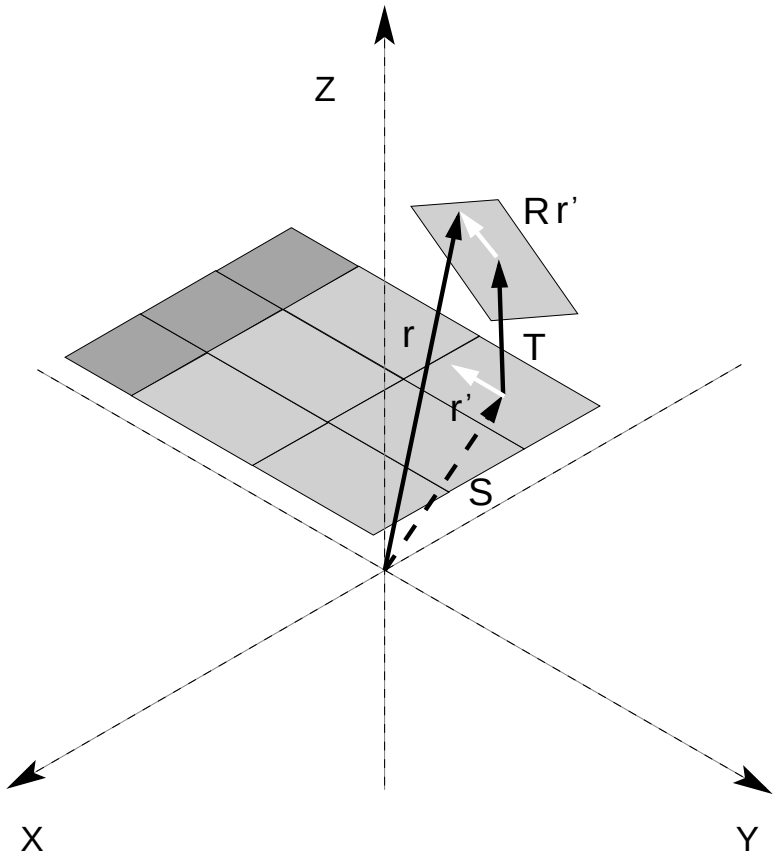


Figure 4.1: *Sketch of the transformation of frame of reference which corrects for the misalignment of the sensors. The vector* $\boldsymbol{r'}$ *contains the coordinates of a point as measured in the silicon sensor frame. Before translating the vector according to the sensor position in the mechanical design (vector* $\boldsymbol{S}$*, see also Fig. 3.17), the sensor has to be rotated by the matrix* R *and translated by the vector* $\boldsymbol{T}$ *to account for the misalignment. The final position of the point in the general reference frame is identified by the vector* $\boldsymbol{r}$ *given by Eq. (4.1).*

sensor, and the translations $\Delta z$, $\Delta y$ and $\Delta x$ along those three axes which shift the sensor from its design position to the real one.

For a point lying on a plane parallel to the X and Y sides of a sensor and passing through its center, let $\boldsymbol{r'} = (x', y', 0)$ represent the coordinates as measured respect to the center of the sensor. Then the coordinates $\boldsymbol{r} = (x, y, z)$ in PAMELA's reference frame after the rototranslation from the ideal to the real position can be expressed as:

$$\boldsymbol{r} \;=\; (\mathsf{R}\,\boldsymbol{r'} \;+\; \boldsymbol{T}) \;+\; \boldsymbol{S}\,, \tag{4.1}$$

where $\mathsf{R}$ is the rotation matrix, $\boldsymbol{T}$ the translation vector, and $\boldsymbol{S}$ is the vector which specify the position of the center of the sensor that the point belongs to (see Fig 4.1). If $\mathsf{R}_x$, $\mathsf{R}_y$, $\mathsf{R}_z$ represent the rotations of the angles $\beta$, $\gamma$, $\omega$ around the orthogonal reference axes:

$$\mathsf{R}_x \;=\; \begin{pmatrix} 1 & 0 & 0 \\ 0 & \cos\beta & -\sin\beta \\ 0 & \sin\beta & \cos\beta \end{pmatrix}\,, \tag{4.2}$$

$$\mathsf{R}_y \;=\; \begin{pmatrix} \cos\gamma & 0 & \sin\gamma \\ 0 & 1 & 0 \\ -\sin\gamma & 0 & \cos\gamma \end{pmatrix}\,, \tag{4.3}$$

$$\mathsf{R}_z \;=\; \begin{pmatrix} \cos\omega & -\sin\omega & 0 \\ \sin\omega & \cos\omega & 0 \\ 0 & 0 & 1 \end{pmatrix}\,, \tag{4.4}$$

the matrix:

$$\mathsf{R} \;=\; \begin{pmatrix} r_{11} & r_{12} & r_{13} \\ r_{21} & r_{22} & r_{23} \\ r_{31} & r_{32} & r_{33} \end{pmatrix} \tag{4.5}$$

describing a generic rotation can be written, according to Euler's rota-

tion theorem, in terms of them as:

$$\mathsf{R} = \mathsf{R}_x \, \mathsf{R}_y \, \mathsf{R}_z \, . \tag{4.6}$$

The elements of $\mathsf{R}$ then correspond to:

$$\begin{aligned}
r_{11} &= \cos\gamma \cos\omega \\
r_{12} &= -\cos\gamma \sin\omega \\
r_{13} &= \sin\gamma \\
r_{21} &= \sin\beta \sin\gamma \cos\omega + \cos\beta \sin\omega \\
r_{22} &= -\sin\beta \sin\gamma \sin\omega + \cos\beta \cos\omega \\
r_{23} &= -\sin\beta \cos\gamma \\
r_{31} &= -\cos\beta \sin\gamma \cos\omega + \sin\beta \sin\omega \\
r_{32} &= \cos\beta \sin\gamma \sin\omega + \sin\beta \cos\omega \\
r_{33} &= \cos\beta \cos\gamma
\end{aligned} \tag{4.7}$$

and, if a first-order approximation is used, the matrix reduces to:

$$\mathsf{R} = \begin{pmatrix} 1 & -\omega & \gamma \\ \omega & 1 & -\beta \\ -\gamma & \beta & 1 \end{pmatrix} \, . \tag{4.8}$$

The translation vector is instead simply given by:

$$\boldsymbol{T} \; = \; (\Delta x, \Delta y, \Delta z) \, , \tag{4.9}$$

and the vector $\boldsymbol{S}$ contains the known coordinates of the center of the sensor in the reference frame of PAMELA, according to the mechanical design:

$$\boldsymbol{S} \; = \; (X, Y, Z) \, . \tag{4.10}$$

Using Eq. (4.8), (4.9) and (4.10), the rototranslation (4.1) which provides

the real coordinates $\boldsymbol{r} = (x, y, z)$ as a function of those measured on the sensor $\boldsymbol{r}' = (x', y', 0)$ becomes:

$$\begin{cases} x &= x' &- \omega\, y' &+ \Delta x &+ X \\ y &= \omega\, x' &+ y' &+ \Delta y &+ Y \\ z &= -\gamma\, x' &+ \beta\, y' &+ \Delta z &+ Z \end{cases} . \tag{4.11}$$

In this framework, the alignment issue reduces to identifying for each sensor the six parameters $\boldsymbol{A} = (\beta, \gamma, \omega, \Delta x, \Delta y, \Delta z)$.

The principle of the method consists in using a sample of properly selected tracks (see Sec. 4.2.1 for the description of the selection criteria) whose deflection, and hence the "shape of the trajectory" in the magnetic field, is known, and in determining the misalignments respect to the design position and orientation by comparing the expected coordinates of the impact points with those which are actually measured. A $\chi^2$ function which contains the differences between the two sets of coordinates (the so-called "residuals") is built, and its minimum value is searched for as the components of the $\boldsymbol{A}$ vector of the hit detectors are let vary, as it will be explained in detail in Sec. 4.2.2. In order to clarify the procedure, let us consider separately each group of six detecting elements one under another along the cavity of the spectrometer: to such set, the name of "*tower* of sensors" is given. First of all it has to be pointed out that not all the $6 \times 6$ parameters which identify the elements in a *tower* can be determined, but only a relative alignment is possible. In principle an absolute frame of reference exists to which positions could be referred: in fact the presence of a nonuniform magnetic field causes the space around the sensors to be not isotropic, so that the coordinate axes could be oriented, and the origin placed, according to its shape. However in practice the inhomogeneities of $\boldsymbol{B}$ prove to be too small for the method to be sensitive enough to them, as it will be shown in Sec. 4.2.2. As a consequence, two of the sensors of the *tower* are taken as reference and they are regarded as being really placed according to their ideal design configuration: this means that their rotations $\beta$, $\gamma$, $\omega$ and translations $\Delta x$, $\Delta y$, $\Delta z$ are set to zero and kept constant during the minimization process. This is sufficient to establish unambiguously positions and orientations

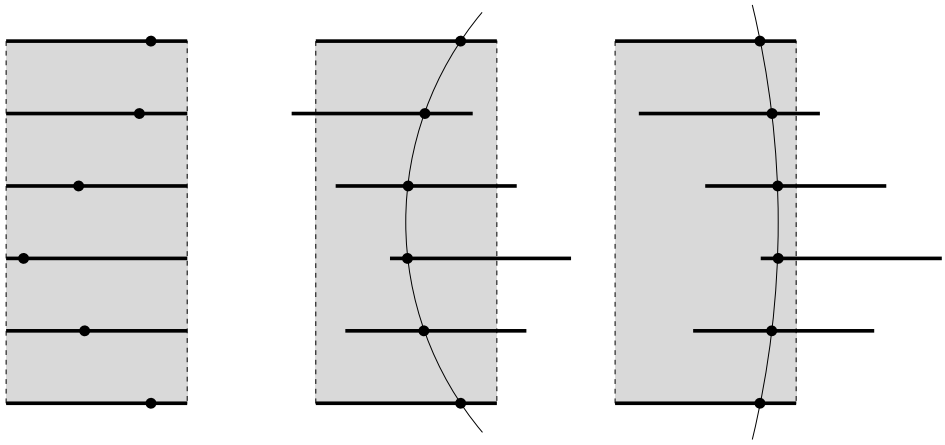


Figure 4.2: *Principle of the alignment method. The pictures represent simplified two-dimensional sketches of a* tower *of sensors. In (a) a set of measured impact points are shown, according to the ideal configuration of the planes. If the couple of farthest sensors are kept fixed as reference, the correct positions of the others can be found as those that make the points lie on the reconstructed trajectory of the particle (b). However, the deflection of the track has to be known, since for particles acquired in a magnetic field there are infinite combinations of different positions and curvatures which comply with the measured points, as for instance in (c).*

of the other elements of the *tower*, if the deflection of the particles in the alignment sample is known. In fact, as shown in Fig. 4.2, even if two sensors are fixed in the chosen reference frame, there is still an infinite number of possible configurations of the other ones which are compatible with trajectories of charged particles with different rigidities in the magnetic field. On the contrary, if the shape of the track is correctly reconstructed on the basis of its known deflection, and two positions in space are determined on the reference planes, the comparison between the other measured points and the expected ones results in a unique configuration of the sensors. A consequence of this kind of approach to the misalignment problem is that the incoming direction of particles can be

affected by a systematic error, of the order of the mechanical precision of the couple of reference sensors, since their reciprocal position cannot be determined. In spite of this uncertainty in the identification of the angle of incidence of cosmic rays, the effect does not interfere with a correct measurement of their momentum, which is the real quantity of interest.

Since any of the six *towers* which compose the tracking system is equivalent to the others for the sake of the alignment, the procedure has been applied independently to each of them. In this way the issue of determining the parameters of the 36 sensors of the spectrometer has been divided into two parts: first each *tower* is aligned with respect to its couple of reference elements using the described technique; then the whole tracking system is considered and the mutual positions of the *towers* are obtained, as explained in Sec. 4.3.

### 4.2.1 Event selection

For the alignment of the single *towers*, events acquired during a test session at the CERN SPS facility in 2003 have been used. The set-up was such that a proton beam with a momentum $p = 50$ GeV/$c$ hit in turn each of the six sensors on the top plane of the spectrometer perpendicularly, in this way crossing all the sensors of the associated *tower*. Moreover, the moving support which PAMELA lay on with its longitudinal axis parallel to the floor, was inclined respect to the beam, first in the X-Z plane in order to have particles crossing the sensors of each *tower* with an angle of about 2°, then in the Y-Z plane with an incidence angle of about 5°. These values were chosen such as to make all the impact points be contained inside a single *tower*: in this way three sets of tracks (perpendicular and inclined in the two projections) were available for each of them. The importance of having non-orthogonal trajectories of particles available for the alignment will be better explained later in Sec. 4.2.2.

The selection of events is performed according to criteria similar to those used in the calibration of the impact-point reconstruction algorithms. Events are required to contain only one track, whose clusters have been detected without loss of information, in this way assuring a

correct and unambiguous identification of the impact points on all the planes. The conditions that have to be fulfilled are:

- cluster *seed* and first-neighbor strips not tagged as *bad* ;
- multiplicity $m < 5$ .

The former cut prevents clusters lying on zones of the sensor with low efficiency or with noisy strips to be used; the latter is useful to limit the negative effects on the resolution due to high-energy $\delta$-rays, which can produce a displacement of the reconstructed impact point (see the discussion in Sec. 3.3). After this preliminary selection, the measured points for each event are assigned to particle trajectories: an algorithm less elaborate is used than the Hough-transform method which is employed in the recognition phase of the main data-reduction procedure, since the purpose of this selection is to isolate events with just one reliable track, and not to identify all the possible particles. For the events in which at least one cluster that has passed the above selection is present on both sides of every plane, track candidates are formed by considering all the possible combinations on the six planes. Candidates are then analyzed separately in the X-Z and Y-Z projections, by means of a line and a circle fit, and if more than one track is identified the event is discarded. The circle fit is performed following the so-called *algebraic method*. If the standard approach of minimizing the geometric distance between the measured points and a circumference is attempted, the problem results to be not linear, and an iterative procedure is required. With the chosen technique instead the quantity which is considered for the $i$-th point $(x_i, z_i)$ is:

$$D_i \;=\; \sqrt{(x_c - x_i)^2 + (z_c - z_i)^2 - r^2}\;, \tag{4.12}$$

and the associated sum of squares on the $N_{pl} = 6$ planes:

$$\chi^2_{xz} \;= \sum_{i=1}^{N_{pl}} D_i^2 \;=\; \sum_{i=1}^{N_{pl}} \left(x_i^2 \;+\; z_i^2 \;+\; p_1\, x_i \;+\; p_2\, z_i \;+\; p_3\right)\;, \tag{4.13}$$

results to be linear in the parameters:

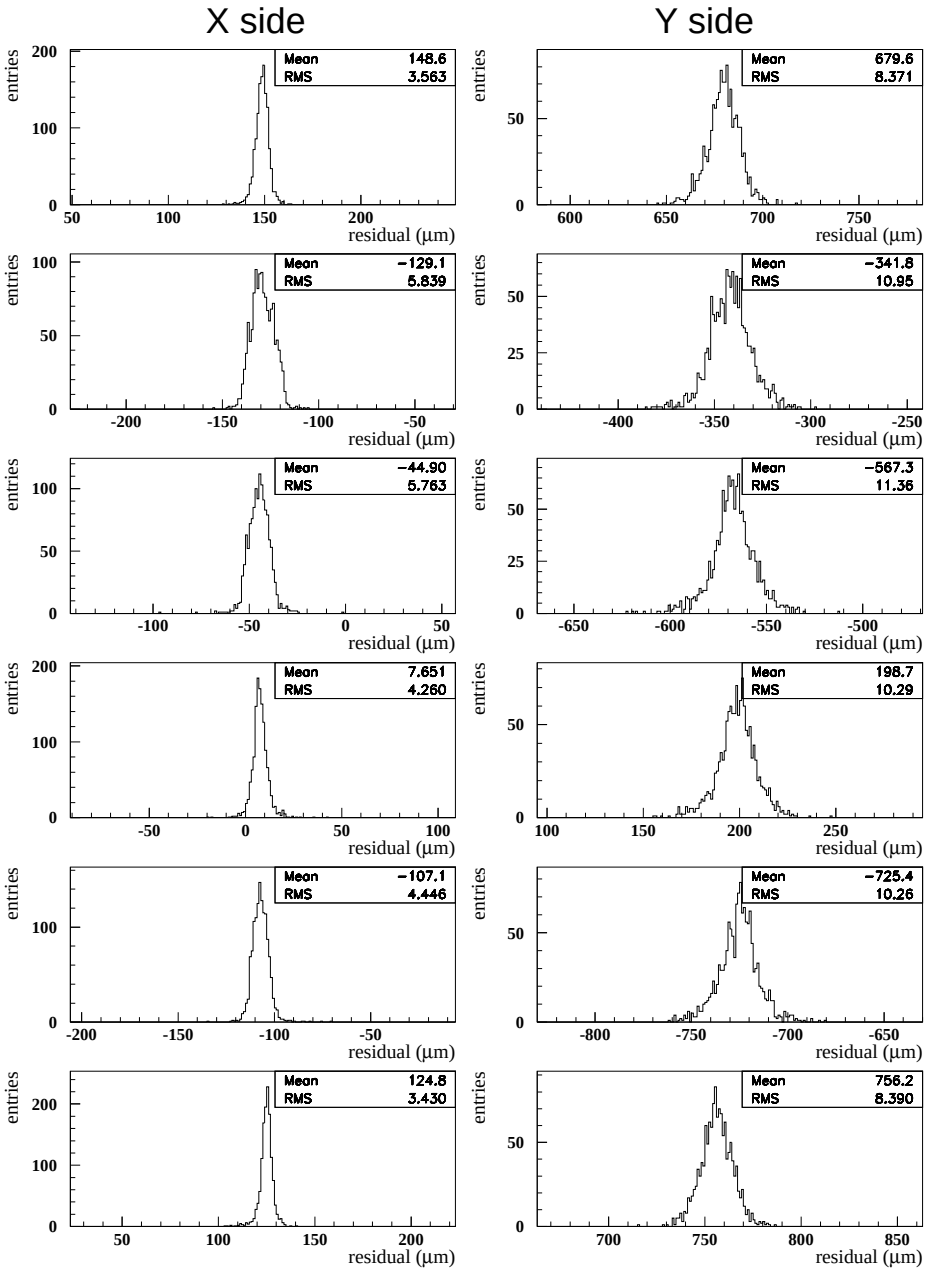


Figure 4.3: *Distributions of the differences between the points measured on a* tower *of sensors and those obtained from a circular fit (X side, left column) and a linear fit (Y side, right column), for a sample of orthogonal tracks of test-beam events.*

$$\begin{cases} p_1 &= -2\ x_c \\ p_2 &= -2\ z_c \\ p_3 &= x_c^2\ +\ z_c^2\ -\ r^2 \end{cases} . \tag{4.14}$$

If the minimum of $\chi^2_{xz}$ is searched for, the system of equations:

$$\begin{pmatrix} \sum x_i^2 & \sum x_i z_i & \sum x_i \\ \sum x_i z_i & \sum z_i^2 & \sum z_i \\ \sum x_i & \sum z_i & \sum 1 \end{pmatrix} \begin{pmatrix} p_1 \\ p_2 \\ p_3 \end{pmatrix} = - \begin{pmatrix} \sum x_i^3 + \sum x_i z_i^2 \\ \sum x_i^2 z_i + \sum z_i^3 \\ \sum x_i^2 + \sum z_i^2 \end{pmatrix} \tag{4.15}$$

is obtained. From Eq. (4.15) the parameters $p_1$, $p_2$ and $p_3$, and consequently the center $(x_c, z_c)$ and the radius $r$ of the circle can be calculated.

The X-Z and Y-Z fits allow also to obtain an estimate of the incidence angle of the particle on the different sensors: this information is used to compute the correct coordinate of the impact point by choosing the most appropriate $\eta$ reconstruction algorithm (see Sec. 3.4). The final selection on the track sample to be used for the alignment is performed by means of a cut on the $\chi^2$ on both the projections, and also on the residuals between the measured points and the reconstructed ones: in this way events in which multiple scattering has altered the particle trajectory are removed, as well as combinations of twelve clusters which are not really associated to a particle. In Fig. 4.3 an example of the distributions of residuals for the two sides of the sensors of a *tower*, in case of orthogonal tracks, are displayed. As it can be seen, the differences between measured and fitted points are not centered on zero, as a consequence of the misalignments with respect to the ideal mechanical positions where the detectors are supposed to be. The discrepancies, which are even of several hundreds of micrometers, are the result of a combination of the rotation and translation of the sensors. At the end of the selection stage, the three sets of tracks (orthogonal and inclined in the X-Z and Y-Z projections) for each *tower* are merged together, and a group of 600 events which will be used for the alignment are extracted from this sample.

### 4.2.2 The alignment method

The events which have been selected contain a single trajectory of a clearly identified particle, whose impact points have been measured correctly on each side of the planes, and whose momentum is known from the accelerator machine parameters. For the $j$-th event, the coordinates $\boldsymbol{r}'_{ij} = (x'_{ij}, y'_{ij}, 0),\ i = 1 \dots N_{pl}$ measured in the silicon sensor frame are transformed according to Eq. (4.1) in order to express them in the spectrometer general reference frame, common to all the planes, as $\boldsymbol{r}_{ij}(\boldsymbol{A}) = \big(x_{ij}(\boldsymbol{A}), y_{ij}(\boldsymbol{A}), z_{ij}(\boldsymbol{A})\big)$. As a first guess, the values of the 36 alignment parameters $\boldsymbol{A} = (\beta_i, \gamma_i, \omega_i, \Delta x_i, \Delta y_i, \Delta z_i)$ of the 6 elements of the *tower* which is being considered are taken equal to zero (i.e. sensors are placed in their ideal design configuration).

The measured points are therefore fitted to reconstruct the track of the particle inside the magnetic field of the spectrometer. The procedure is similar to that which has been previously explained in detail in Sec. 3.5.2 and makes use of the $\boldsymbol{B}$ interpolation technique already described in Sec. 3.5.3, but two main differences have to be noted. First, while during the standard reconstruction of an event (after the alignment parameters have been already determined) the starting guess for the minimization process derives from the Hough-transform algorithm, in this case the initial value of the state vector $\boldsymbol{\alpha}$ comes from the simple line and circle fits done during the selection of events. The second and more important difference resides in the fact that the purpose of the track fitting consists in general in calculating the particle deflection, while here this value is known *a priori* from the beam momentum: consequently, the fifth component of the state vector $\boldsymbol{\alpha} = (x^*, y^*, \sin\theta^*, \varphi^*, \eta)$ is kept fixed during the minimization procedure.

After the best trajectory and the corresponding reconstructed coordinates $\tilde{\boldsymbol{r}}_{ij}(\boldsymbol{A}) = \big(\tilde{x}_{ij}(\boldsymbol{A}), \tilde{y}_{ij}(\boldsymbol{A}), \tilde{z}_{ij}(\boldsymbol{A})\big)$ have been determined for each track, they are compared with the originally measured coordinates of the impact points $\boldsymbol{r}_{ij}(\boldsymbol{A})$, and the function:

$$\chi^2(\boldsymbol{A}) = \sum_{j=1}^{N_{ev}} \chi_j^2(\boldsymbol{A}) = \\ = \sum_{j=1}^{N_{ev}} \sum_{i=1}^{N_{pl}} \left[ \left( \frac{x_{ij}(\boldsymbol{A}) - \tilde{x}_{ij}(\boldsymbol{A})}{\sigma_{x_i}} \right)^2 + \left( \frac{y_{ij}(\boldsymbol{A}) - \tilde{y}_{ij}(\boldsymbol{A})}{\sigma_{y_i}} \right)^2 \right] \tag{4.16}$$

is calculated, by adding up the $\chi_j^2$ of the single tracks of the $N_{ev}$ events (see also Eq. 3.36). A new iterative minimization is performed on this global $\chi^2$, by varying the values of the components of the vector $\boldsymbol{A}$, which appear in both the sets of coordinates that are used to build the sum of the squares of the residuals. For each *tower*, the number of free alignment parameters should be 24 (6 parameters $\times$ 4 free sensors), but actually another one can be added, as it will be explained later. It has to be noted that for each variation of the vector $\boldsymbol{A}$, all the tracks of the sample have to be fitted again to reconstruct the trajectories which result from the new configuration of sensors.

As explained in Sec. 4.2, for each of the six *towers* of the spectrometer a couple of elements have to be kept fixed in the minimization, as reference positions. The best choice for them would be the pair of most external sensors, since in this way the indetermination on the incoming direction of particles would be minimized. However the bottom plane of the tracking system differs from the others in its geometric configuration: in fact, as it is represented in Fig. 3.17, its sensors are turned upside down by means of a rotation around a line parallel to the X axis, and they are shifted along the Y coordinate with respect to the other elements of the *tower*. This choice is connected to the need of space for housing the boards that contain the acquisition electronics of the planes: since each board is placed on the external side of one of the five magnetic blocks, the sixth board had to be put on the bottom block too, on the opposite side respect to the fifth one. This translates into a different way the aluminium frame which contains those silicon detectors is attached to the structure of the magnet, and it makes convenient to choose the plane located over the bottom one as reference for the alignment.

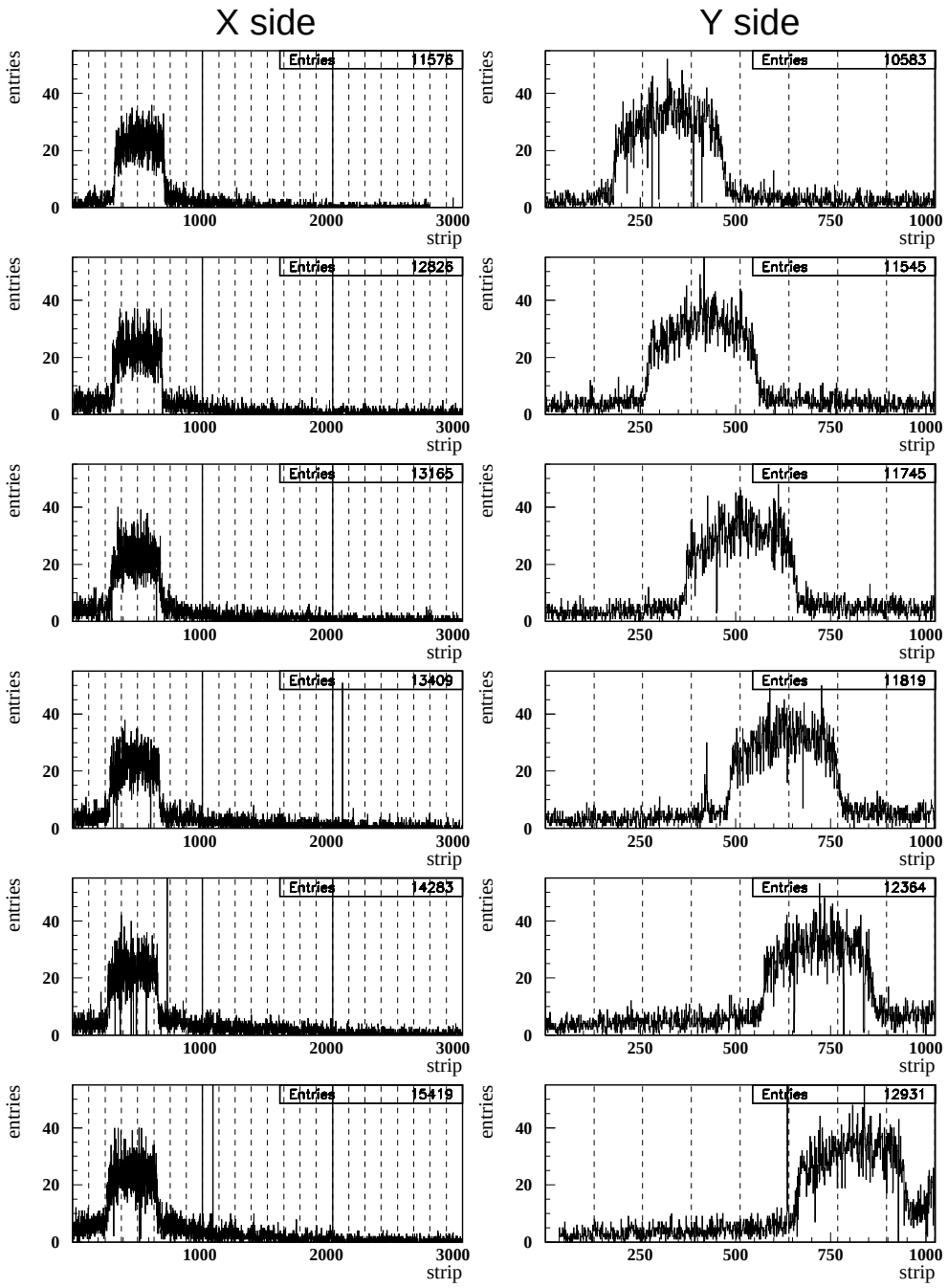


Figure 4.4: *Beam profile for one of the alignment samples. From top to bottom, the six planes are shown as they appear along the path of particles. The plots on the X side represent the number of hits on each strip as a function of the strip number for the three ladders of the plane (3072 channels), while on the Y side both the sensors which form a ladder are added up, because of the read-out ambiguity (1024 channels). Vertical dotted lines highlight the divisions between groups of 128 strips connected to the same VA1 chip.*

Among the three coordinates of the particle impact points on the silicon planes, only those that are actually measured, namely $x$ and $y$, appear in the expression given by Eq. (4.16) for the $\chi^2$. The parameters which are contained directly in the correction for the misalignment of $x$ and $y$ (see Eq. (4.11)) are only $\Delta x$, $\Delta y$ and $\omega$, while $\beta$, $\gamma$ and $\Delta z$ get involved exclusively as higher-order corrections, through $z$, in the calculation of the fit-reconstructed coordinates $\tilde{x}$ and $\tilde{y}$. For this reason the method is less sensitive to variations of the rotations around the X and Y axes and of the translations along Z than to the others. In particular, it is necessary that the event sample which is used for the alignment contains not only perpendicular trajectories of particles with respect to the sensors, but also inclined ones. In fact, for instance, in case all the tracks were orthogonal to the planes, a variation of $\Delta z$ would not make the coordinates $\tilde{x}$ and $\tilde{y}$ resulting from the fit vary, and likewise the $\chi^2$. For a similar reason, in order to better the sensitivity to rotations, impact points are required to be spread on a not too small fraction of the area of the sensors. In Fig. 4.4 a representation of the beam profile for one of the alignment samples of tracks is shown. In this case particles hit the sensors perpendicularly in the bending projection and with an angle in the other one; the width of the beam is about 400 strips in the X-Z plane (which corresponds to $\sim 2.0$ cm) and about 350 strips in the Y-Z plane ($\sim 2.3$ cm).

In order to determine the values of the parameters that minimize the $\chi^2$, the MINUIT package, which is part of the CERN software libraries [60], is used. A careful study of the optimal approach to the problem had to be done in order to minimize this complicated function, which represents a generalized surface in a 25-dimensional space. Several different strategies have been attempted, and the following one has proved to be the best procedure to solve this problem. As stated before, some of the parameters (namely the translations along the X and Y axes and the rotations around the Z axis) are simpler to be calculated than the others, because the measured coordinates depend directly on them. For this reason, first the minimum of the $\chi^2$ is found only respect to those variables, while $\beta$, $\gamma$ and $\Delta z$ are kept constant for all the sensors. When the lowest value of the function has been found, also the remaining

components of the vector $\boldsymbol{A}$ are freed, and a new minimum is looked for: in such a way, during the first step the search directions on the $\chi^2$ surface are along its steepest descent and this favors the convergence of the method. This approach also helps in preventing MINUIT from moving towards unwanted regions of the function space characterized by unphysical values of the parameters. Much care has to be put in the choice of the optimal settings of the algorithm as well, such as the vertical tolerance in the research of the minimum that the best $\boldsymbol{A}$ vector corresponds to.

Previously it has been explained how the rotations and the translations which the method is able to determine are those of all the sensors save a pair of them, that have to be kept fixed in their design positions. Actually, it is found experimentally that if, once the process has converged to a minimum of the 24 standard parameters, these ones are fixed to their current values and those of the reference sensors are let free to vary one by one, indeed the function appears flat along the corresponding directions in the parameter space (i.e. it is not sensitive to a movement that changes their mutual distance, for instance), except for one. In fact the $\chi^2$ shows a minimum also as the rotation angle around Z of one of the two reference sensors changes: this means that, with a careful control of the minimization algorithm, it is possible to determine their mutual rotation around the Z axis too, which corresponds to a torsion of the whole *tower*. In other words, the method is sensitive enough to detect when a twisting of the particle trajectory on itself results in a lower value of the $\chi^2$. On the contrary, the fact that if some of the other parameters of the reference sensors are let free to vary the $\chi^2$ displays no dependence on them shows that, for the sensitivity which the method can reach, a relative displacement of theirs makes the other elements of the *tower* arrange in such a way that the deflection of the particle (which, it has to be remarked is provided in input to the procedure, and its value is fixed) does not change. This behavior has been confirmed also by means of an analysis of a set of simulated data, as explained in next Sec. 4.2.3.

A final stage of the process, which is performed in order to exclude tracks that for some reason has not been correctly reconstructed in the fitting procedure, consists in discarding events whose $\chi^2_j$ results more

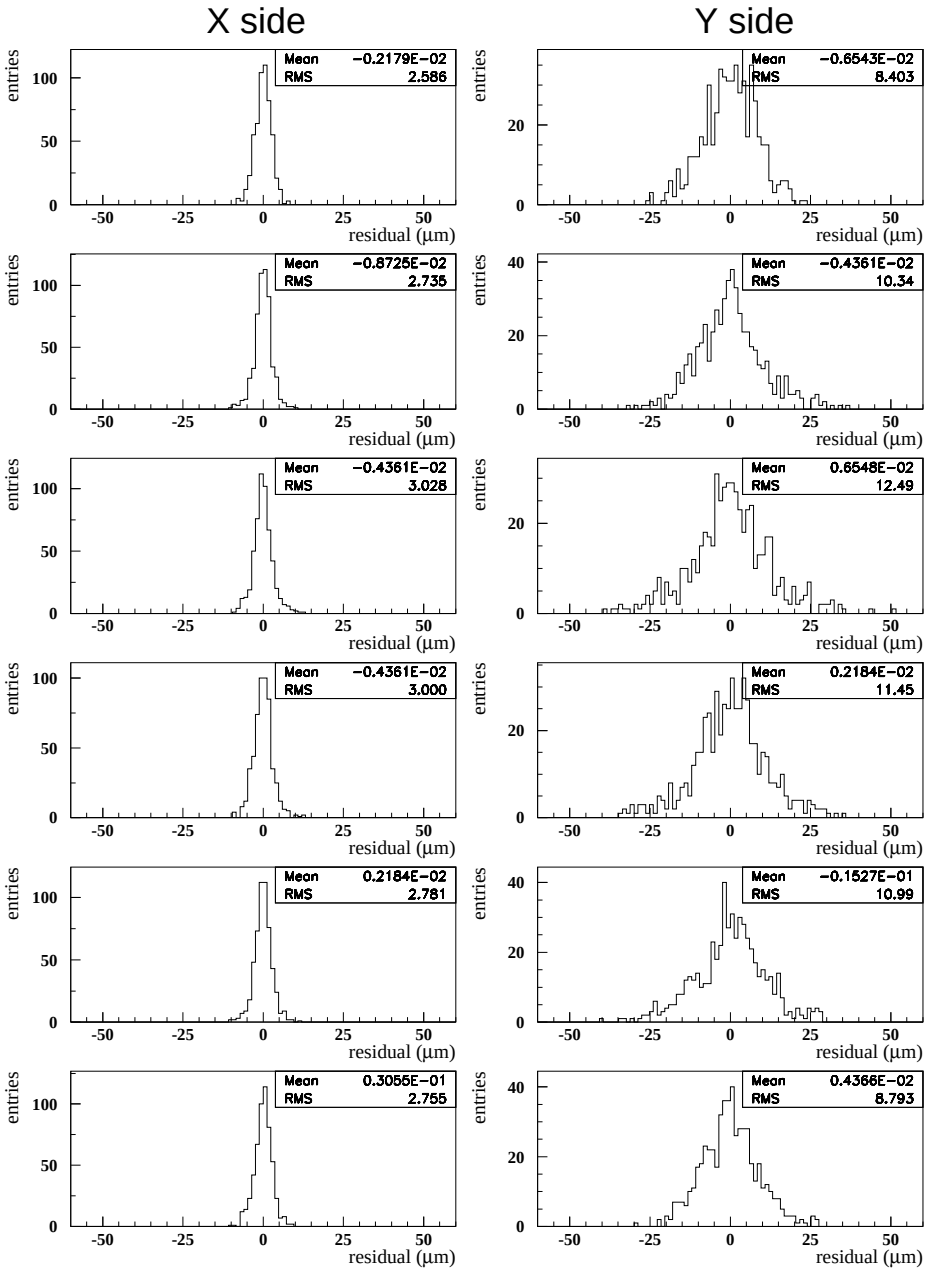


Figure 4.5: *Distributions of the differences between the measured points and those obtained from the track fitting, for a* tower *of sensors after the alignment with test-beam data.*

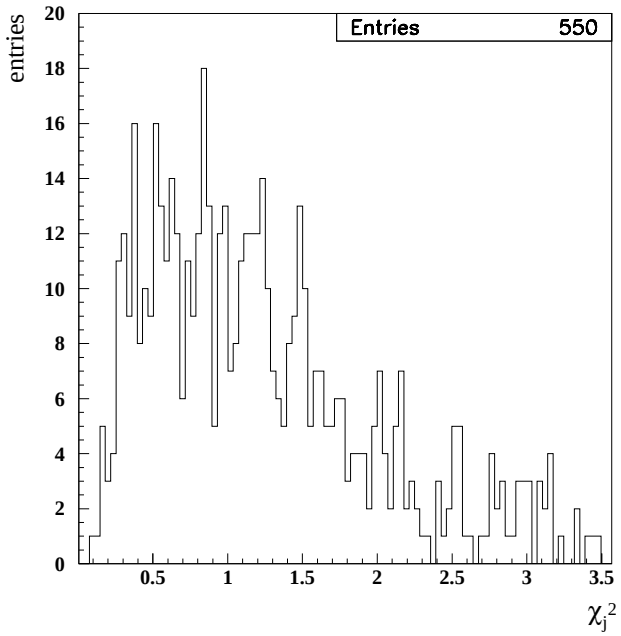


Figure 4.6: *Distribution of the reduced $\chi^2_j$ for the tracks which have been used to align a* tower *of sensors. The number of degrees of freedom for each $\chi^2_j$ is 8: the number of measures is 12 (6 X + 6 Y coordinates), the fitted parameters are 4 (the five components of the state vector, expect for the fixed value of the deflection $\eta$).*

than 3 standard deviations away from the mean value, and in repeating the whole minimization until no more tracks are excluded. The number of events which survive this selection and which are actually used for the alignment varies with each *tower*, ranging between 550 and 567.

The whole alignment procedure requires on average about 10 hours of computing time on a 3 GHz processor, for each of the six *towers* of the tracking system.

In Fig. 4.5 the distributions of the differences between the measured and the reconstructed points on the two sides of the six sensors of a *tower* are shown. By comparing these plots with those of Fig. 4.3, it can be

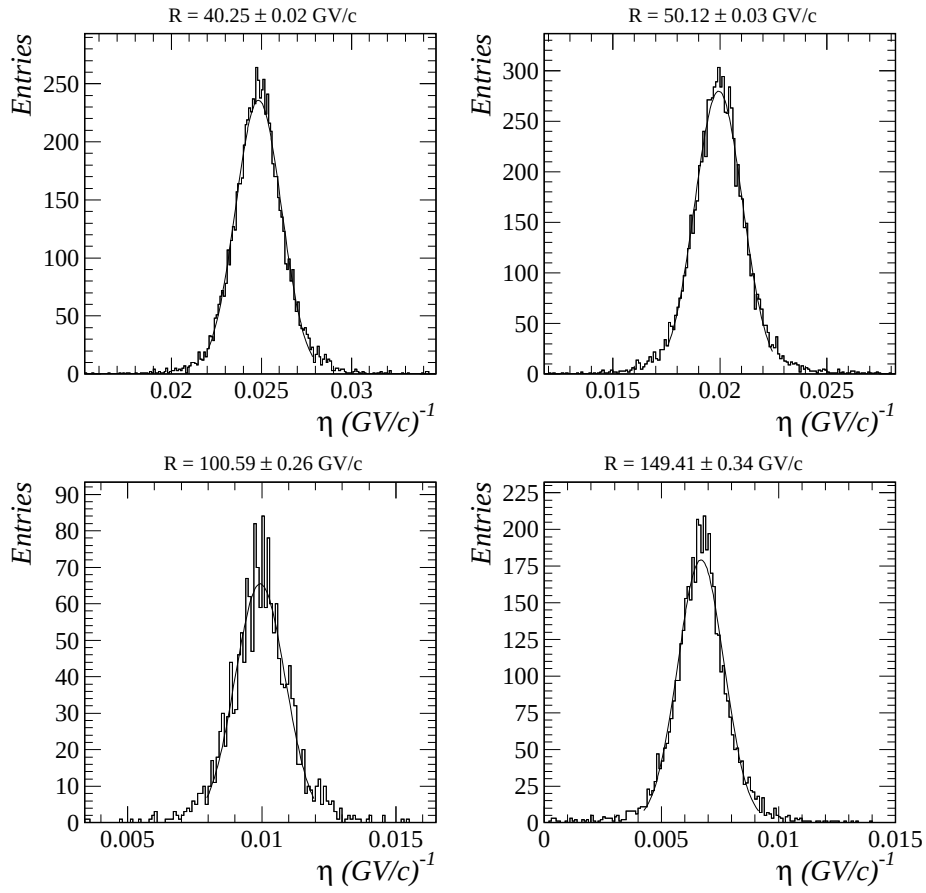


Figure 4.7: *Deflection distributions of test-beam protons after the alignment procedure has been applied. The rigidity obtained as the mean of a Gaussian fit on data is reported for each plot. This has to be compared with the nominal values of the rigidity as obtained from the machine parameters, which are 40, 50, 100 and 150 GV/c respectively, with an uncertainty of the order of 1%.*

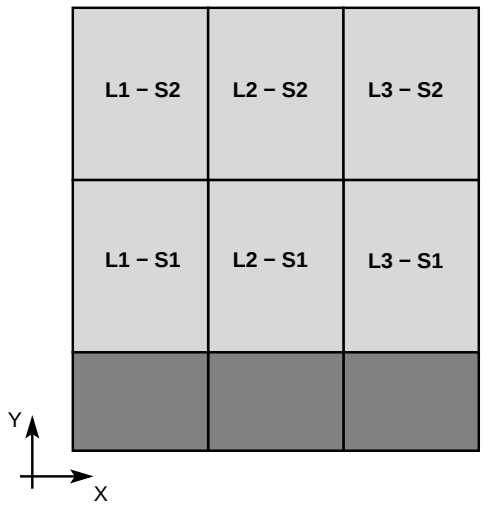


Figure 4.8: *Schematic representation of a plane of the tracking system, showing the naming scheme for the six* towers *of sensors. They are identified by a couple of labels that represent the ladder (L1, L2, L3) and the sensor (S1, S2). The bottom row of dark rectangles shows the hybrids which house the front-end electronics.*

seen that now the residuals are very well centered on zero and also that their widths are lower. The distributions refer to all the tracks which survived the event selection, so they contain perpendicular and inclined trajectories (2° in the X-Z plane and 5° in the Y-Z plane.) The widths are consistent with those expected from the simulation of the impact-point reconstruction (see Fig. 3.13). The corresponding distribution of the reduced $\chi^2_j$ of the tracks is shown in Fig. 4.6. Fig. 4.7 contains instead an example of how the correct deflection of particles can be measured after the impact points have been corrected for the misalignment. The plots refers to four different rigidities of the proton beam, which are consistent with the measured values.

The parameters of the 36 sensors which are found by means of the single-*tower* alignment procedure are reported in Tab. 4.1. Each column corresponds to one of the *towers*, which are identified by a couple of labels (see Fig. 4.8) that represent the ladder (L1, L2, L3) and the sensor (S1,

| | | L 1 - S 1 | | L 1 - S 2 | | L 2 - S 1 | | L 2 - S 2 | | L 3 - S 1 | | L 3 - S 2 | |
|---|---|---|---|---|---|---|---|---|---|---|---|---|---|
| | | Value | Error | Value | Error | Value | Error | Value | Error | Value | Error | Value | Error |
| PLANE 1 | $\beta$ | 0. | FIXED | 0. | FIXED | 0. | FIXED | 0. | FIXED | 0. | FIXED | 0. | FIXED |
| | $\gamma$ | 0. | FIXED | 0. | FIXED | 0. | FIXED | 0. | FIXED | 0. | FIXED | 0. | FIXED |
| | $\omega$ | 0. | FIXED | 0. | FIXED | 0. | FIXED | 0. | FIXED | 0. | FIXED | 0. | FIXED |
| | $\Delta x$ | 0. | FIXED | 0. | FIXED | 0. | FIXED | 0. | FIXED | 0. | FIXED | 0. | FIXED |
| | $\Delta y$ | 0. | FIXED | 0. | FIXED | 0. | FIXED | 0. | FIXED | 0. | FIXED | 0. | FIXED |
| | $\Delta z$ | 0. | FIXED | 0. | FIXED | 0. | FIXED | 0. | FIXED | 0. | FIXED | 0. | FIXED |
| PLANE 2 | $\beta$ | 0.6 | 1.2 | -3.0 | 1.2 | 0.1 | 1.0 | -0.7 | 1.0 | 1.3 | 1.4 | 1.7 | 1.4 |
| | $\gamma$ | -1.72 | 0.85 | -5.41 | 0.88 | 0.11 | 0.63 | 0.35 | 0.54 | 4.9 | 1.1 | 1.5 | 1.0 |
| | $\omega$ | -0.934 | 0.029 | -0.765 | 0.028 | -0.598 | 0.030 | -0.643 | 0.030 | -0.827 | 0.042 | -0.833 | 0.043 |
| | $\Delta x$ | 160.31 | 0.23 | 245.01 | 0.23 | 165.13 | 0.25 | 234.37 | 0.25 | 154.74 | 0.31 | 236.19 | 0.32 |
| | $\Delta y$ | 682.90 | 0.69 | 671.20 | 0.70 | 613.86 | 0.68 | 611.57 | 0.66 | 562.98 | 0.70 | 561.01 | 0.69 |
| | $\Delta z$ | -57. | 14. | -82. | 15. | -51.6 | 9.9 | 14.6 | 9.1 | -165. | 9.8 | -79.4 | 9.7 |
| PLANE 3 | $\beta$ | -1.0 | 1.1 | 0.5 | 1.1 | 0.3 | 1.0 | -1.4 | 1.0 | -0.2 | 1.1 | 0.2 | 1.1 |
| | $\gamma$ | 3.03 | 0.77 | 2.49 | 0.82 | 1.04 | 0.60 | 0.92 | 0.53 | 0.1 | 1.2 | 1.6 | 1.2 |
| | $\omega$ | 1.547 | 0.033 | 1.54 | 0.033 | 1.433 | 0.035 | 1.475 | 0.036 | 1.487 | 0.045 | 1.606 | 0.044 |
| | $\Delta x$ | 159.57 | 0.25 | 99.13 | 0.25 | 139.32 | 0.22 | 94.51 | 0.23 | 138.79 | 0.28 | 78.72 | 0.26 |
| | $\Delta y$ | 525.65 | 0.63 | 533.00 | 0.63 | 565.67 | 0.65 | 555.9 | 0.64 | 578.45 | 0.73 | 586.26 | 0.71 |
| | $\Delta z$ | 140. | 10. | 104. | 11. | 43.1 | 6.3 | 24.7 | 7.0 | -67.0 | 9.9 | -44.2 | 8.4 |
| PLANE 4 | $\beta$ | 0.3 | 1.1 | 0.5 | 1.2 | 1.03 | 0.82 | -0.82 | 0.82 | 4.8 | 1.0 | 3.0 | 1.0 |
| | $\gamma$ | 1.34 | 0.92 | -0.11 | 0.92 | -0.91 | 0.72 | 0.52 | 0.68 | -3.5 | 1.7 | -1.1 | 1.7 |
| | $\omega$ | 1.689 | 0.042 | 1.783 | 0.042 | 1.564 | 0.039 | 1.592 | 0.041 | 1.848 | 0.047 | 1.862 | 0.046 |
| | $\Delta x$ | 19.91 | 0.25 | -20.07 | 0.26 | -27.56 | 0.21 | -50.41 | 0.23 | 29.85 | 0.22 | -25.67 | 0.22 |
| | $\Delta y$ | -581.75 | 0.67 | -577.86 | 0.67 | -565.19 | 0.67 | -569.42 | 0.64 | -529.71 | 0.76 | -529.09 | 0.72 |
| | $\Delta z$ | 65. | 10. | 45. | 10. | -25.2 | 6.7 | 26.8 | 6.6 | 18. | 15. | 61. | 14. |
| PLANE 5 | $\beta$ | 0. | FIXED | 0. | FIXED | 0. | FIXED | 0. | FIXED | 0. | FIXED | 0. | FIXED |
| | $\gamma$ | 0. | FIXED | 0. | FIXED | 0. | FIXED | 0. | FIXED | 0. | FIXED | 0. | FIXED |
| | $\omega$ | 1.437 | 0.038 | 1.580 | 0.038 | 1.727 | 0.039 | 1.609 | 0.041 | 1.415 | 0.045 | 1.364 | 0.043 |
| | $\Delta x$ | 0. | FIXED | 0. | FIXED | 0. | FIXED | 0. | FIXED | 0. | FIXED | 0. | FIXED |
| | $\Delta y$ | 0. | FIXED | 0. | FIXED | 0. | FIXED | 0. | FIXED | 0. | FIXED | 0. | FIXED |
| | $\Delta z$ | 0. | FIXED | 0. | FIXED | 0. | FIXED | 0. | FIXED | 0. | FIXED | 0. | FIXED |
| PLANE 6 | $\beta$ | 3.01 | 0.94 | 6.30 | 0.93 | 2.12 | 0.67 | 6.49 | 0.69 | 3.89 | 0.91 | 7.79 | 0.92 |
| | $\gamma$ | 2.4 | 1.3 | 5.1 | 1.4 | 4.36 | 0.74 | 4.44 | 0.76 | -2.8 | 2.3 | -4.4 | 2.3 |
| | $\omega$ | 2.843 | 0.038 | 2.998 | 0.037 | 1.987 | 0.039 | 2.010 | 0.040 | 1.495 | 0.046 | 1.490 | 0.044 |
| | $\Delta x$ | -244.60 | 0.28 | -321.67 | 0.31 | -280.22 | 0.25 | -267.96 | 0.26 | -276.22 | 0.29 | -257.30 | 0.28 |
| | $\Delta y$ | -1905.99 | 0.89 | -1888.92 | 0.89 | -1854.57 | 0.85 | -1856.54 | 0.84 | -1875.0 | 1.0 | -1876.5 | 1.0 |
| | $\Delta z$ | 707.7 | 9.1 | 590.9 | 9.6 | 427. | 10. | 422.7 | 9.0 | 583. | 34. | 674. | 34. |

Table 4.1: *Single*-tower *alignment parameters. The rotation angles $\beta$, $\gamma$ and $\omega$ are in milliradians, while the translations $\Delta x$, $\Delta y$ and $\Delta z$ are in micrometers. Statistical errors are reported with two significant digits.*

S2), while rows contain the values of $\boldsymbol{A} = (\beta, \gamma, \omega, \Delta x, \Delta y, \Delta z)$ for the six planes. The elements 1 and 5 of each *tower* have their parameters set to zero (save the rotation around the Z axis of the fifth sensor), as they have been chosen as reference for the alignment procedure. Rotation angles are expressed in milliradians, translations in micrometers, and the errors which are reported are those of statistic origin, coming from the minimization procedure. The order of magnitude of the corrections respect to the ideal design configuration is of hundreds of micrometers, and agrees with the one that has been anticipated in Sec. 4.1. The bottom plane (which is the one with a different mechanical structure) shows the largest displacements along the Y direction, as expected. As it can be seen, the errors in calculating the misalignments of the sensors which can be obtained with this method using about 550 events, are low enough to allow not to spoil the very high spatial resolution of the detector (the widths of the distributions of residuals in Fig. 4.5 give an idea of the performances of the spectrometer). In particular, the translations along the X and Y axes and the rotations around the Z axis (which are the kind of misalignments that give the most significant contributions, see Eq. (4.11)) can be determined with high precision. The average uncertainties on the six parameters are: $\delta\beta = 1.0$ mrad, $\delta\gamma = 1.0$ mrad, $\delta\omega = 0.039$ mrad, $\delta\Delta x = 0.26$ $\mu$m, $\delta\Delta y = 0.74$ $\mu$m, $\delta\Delta z = 12$ $\mu$m.

### 4.2.3 Check of the alignment procedure

The principle at the basis of the alignment procedure has been verified by means of simulated data generated with the GPAMELA software [73]. This tool is based on the GEANT 3.21 package (which is part of the CERN software libraries [60]), and allows to simulate particles and reproduce their interaction within the PAMELA instrument.

A set of events with the same characteristics of those of the test-beam data used for the alignment (50 GeV/$c$ protons crossing a *tower* of sensors with three different incidence angles, see Sec. 4.2.1) have been generated. The geometry of the spectrometer which is used in the software for the production of particles complies with that of the design of the instrument; that is to say the parameters $\boldsymbol{A} = (\beta, \gamma, \omega, \Delta x, \Delta y, \Delta z)$ which account for

| | PLANE 1 | | PLANE 2 | | PLANE 3 | |
|---|---|---|---|---|---|---|
| | Value | Error | Value | Error | Value | Error |
| $\beta$ | 0. | FIXED | 0.02 | 0.35 | -0.06 | 0.34 |
| $\gamma$ | 0. | FIXED | 0.21 | 0.44 | 0.28 | 0.48 |
| $\omega$ | 0. | FIXED | 0.004 | 0.012 | 0.003 | 0.016 |
| $\Delta x$ | 0. | FIXED | -0.05 | 0.18 | -0.04 | 0.19 |
| $\Delta y$ | 0. | FIXED | 0.06 | 0.68 | 0.13 | 0.65 |
| $\Delta z$ | 0. | FIXED | 0.3 | 6.2 | 0.3 | 6.4 |
| | PLANE 4 | | PLANE 5 | | PLANE 6 | |
| | Value | Error | Value | Error | Value | Error |
| $\beta$ | -0.21 | 0.39 | 0. | FIXED | 0.14 | 0.48 |
| $\gamma$ | 0.14 | 0.49 | 0. | FIXED | -0.07 | 0.61 |
| $\omega$ | 0.016 | 0.024 | 0.023 | 0.029 | 0.032 | 0.032 |
| $\Delta x$ | -0.01 | 0.20 | 0. | FIXED | -0.18 | 0.39 |
| $\Delta y$ | 0.11 | 0.69 | 0. | FIXED | -0.12 | 0.89 |
| $\Delta z$ | -1.4 | 7.2 | 0. | FIXED | 3. | 12. |

Table 4.2: *Alignment parameters for a* tower *of sensors as obtained from the check of the procedure by means of simulated data. The rotation angles $\beta$, $\gamma$ and $\omega$ are in milliradians, the translations $\Delta x$, $\Delta y$ and $\Delta z$ in micrometers. Statistical errors are reported with two significant digits.*

the misalignments are all set to zero. Data are treated as truly detected events: they go through the standard selection processes, and a sample of 600 tracks out of them is chosen for one of the *towers* of the spectrometer.

The alignment procedure is applied to those events, but a wrong set of parameters is given as input to the algorithm: in this way the sensors are artificially rotated and translated of random quantities of the order of some milliradians and some millimeters respectively in arbitrary directions. The objective of the check is to obtain back the true null alignment parameters which had been previously used to generate the events in the simulation. Indeed, this approach is equivalent to generating events according to a misaligned configuration of sensors with respect to the design one (that is the true experimental situation in case of real data), and afterwards trying to determine the corresponding parameters starting from the ideal mechanical positions of the sensors.

The results of the process on this set of simulated data are reported in Tab. 4.2. From the table it can be seen that the algorithm is actually able to retrieve the correct values for the rotations and translations of

the free parameters of the *tower* elements within the statistical error, and that no evidence of a systematic uncertainty can be inferred.

Simulated data have also been used to control the assumption of the method regarding the way the positions of the other sensors are modified, respect to those resulting from the single-*tower* alignment, when the parameters of the reference sensors change. As stated before in Sec. 4.2.2, the $\chi^2$ does not vary if, for instance, their distance is modified: this means that for the sake of the algorithm, all the configurations which differ for the mutual position of the reference sensors are equally acceptable, and they result in the same magnetic deflection of particles[2]. In fact by applying the alignment algorithm to a set of simulated data and modifying artificially the fixed parameters of the reference sensors (for instance, if the translation $\Delta x$ of the upper one is set to $+100$ $\mu$m respect to the real position), it can be seen that all the other detectors arrange accordingly ($+75$, $+50$, $+25$, 0, $-25$ $\mu$m respectively, in this example). The situation is represented schematically in Fig. 4.9.

## 4.3 Whole-tracker alignment

The algorithm which has been described allows, once it is applied independently to each one of the six *towers* of the spectrometer, to calculate the corrections that have to be applied with respect to the design configuration of the sensors, and thus to obtain their true positions in space. In this way the deflection of particles which cross from top to bottom a single *tower* can be measured. While being fit for an artificial beam of particles with a definite incoming direction, this is not completely useful in case of cosmic rays, whose flux is isotropic: in order to measure the deflection of particles in all the acceptance of PAMELA, the information about the positions of the six *towers* has to be merged together, and an alignment of the whole tracking system is required. A procedure has been developed, which employs particles whose trajectory go across the

[2]What occurs at first order if the positions of the reference sensors differ from the true ones is a not a systematic error on deflection, that is to say on the magnitude of the momentum $\boldsymbol{p}$, which is the quantity that the spectrometer is finally going to measure, but on the incoming direction of the particle. See also Fig. 4.9.

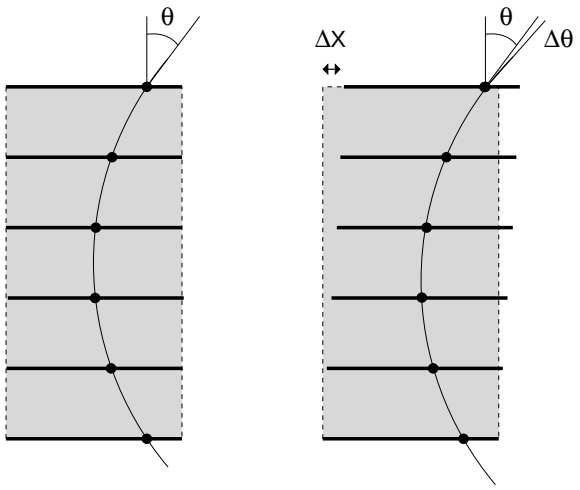


Figure 4.9: *Sketch of the way a* tower *is deformed when one of the reference sensors is shifted respect to its design position. In order to maintain the mutual alignment, the other sensors are displaced too, proportionally to their distance from the reference one. At first order this changes the measured incoming direction of the particle but not its deflection.*

*towers*, and which allows to determine the mutual positions of all the 36 silicon sensors of the spectrometer. Since a suitable sample of such kind of tracks was not present among the available test-beam data, the algorithm has been optimized for cosmic-ray tracks, even in view of its use as a method to calibrate the alignment corrections after the launch and during the satellite lifetime.

The principle at the basis of the method is similar to that of the single-*tower* alignment: a set of suitably selected "clean" events and their associated impact points on the silicon planes are used to build a function which is minimized by the correct set of alignment parameters. The starting configuration for the minimization is the result of the previously described test-beam alignment, in which a pair of elements in each *tower* is kept in the positions defined by the mechanical design. The $\chi^2$ is analogous to that of Eq. (4.16), but the free variables that it depends on are now the vectors $\boldsymbol{A} = (\beta, \gamma, \omega, \Delta x, \Delta y, \Delta z)$ of the sensors which had

been previously chosen as reference. As their rotations and translations are let vary, the sum of the squares of the residuals between the points which have been measured and those reconstructed from the track fitting in the magnetic field will change, and will show a minimum when the true configuration of all the 36 sensors is reached.

While the rotations and translations of the pairs of reference elements vary, those of the other detectors have to be modified accordingly, in order to preserve the relative alignment inside each *tower*. The way the parameters are modified is suggested by the study done by means of the simulated data, which has been described in Sec. 4.2.3 and Fig. 4.9: to a translation of a reference sensor respect to its design position, a progressive displacement of all the others follows, according to their distance from it since, as it has been stated in Sec. 4.2.2, the $\chi^2$ is not sensitive to such deformations for a fixed deflection. In practice, a simplified approach to the issue of maintaining the relative alignment inside each *tower* has been adopted. It consists in using a function which computes how the parameters of a single *tower* have to be modified when one of its reference sensors is rototranslated, or the other is translated respect to the first one. The former transformation, which will be labeled "RT1", is done on the sensor belonging to plane 1, and it has as a consequence that all the sensors of the *tower* follow the rototranslation as a rigid body. The latter, which will be indicated as "T5", concerns sensor 5, and in this case the *tower* is deformed as described before.

The relation between the final value of the angles of rotation and of the translation vector for a generic detector, as a function of those of the its reference sensors, can be found by an appropriate composition of these two transformations. In practice, what has to be determined is the way the coordinates of a point on a sensor change when the *tower* is rototranslated according to RT1 and deformed as to T5. The equation:

$$\boldsymbol{r}_i'' \;=\; \mathsf{R}_i\, \boldsymbol{r}_i' \;+\; \boldsymbol{T}_i \;, \tag{4.17}$$

gives the vector $\boldsymbol{r}_i''$, which identifies a point measured on a sensor belonging to the $i$-th plane, respect to the ideal position of the mechanical design, after its coordinates $\boldsymbol{r}_i' = (x_i', y_i', 0)$ have been corrected for the

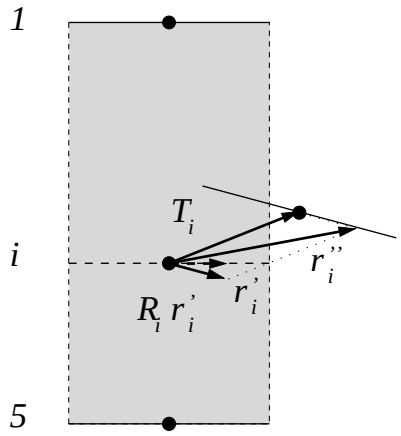


Figure 4.10: *Sketch of the transformation used for the whole-tracker alignment. For clarity, only three planes are drawn in this and in the following schematic two-dimensional representations of the tracking system; their centers are represented by the black dots. This picture refers to the vectors involved in Eq. (4.17).*

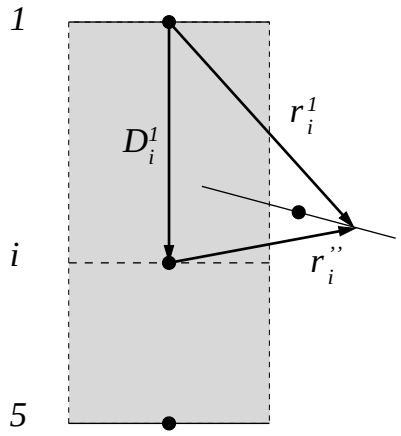


Figure 4.11: *Sketch of the vectors involved in Eq. (4.18).*

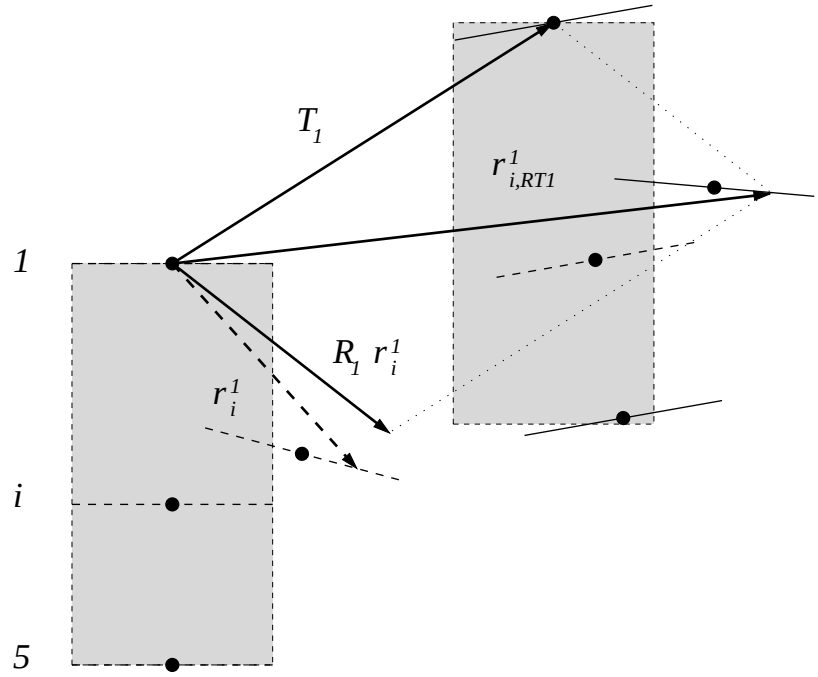


Figure 4.12: *Sketch of the vectors involved in Eq. (4.19).*

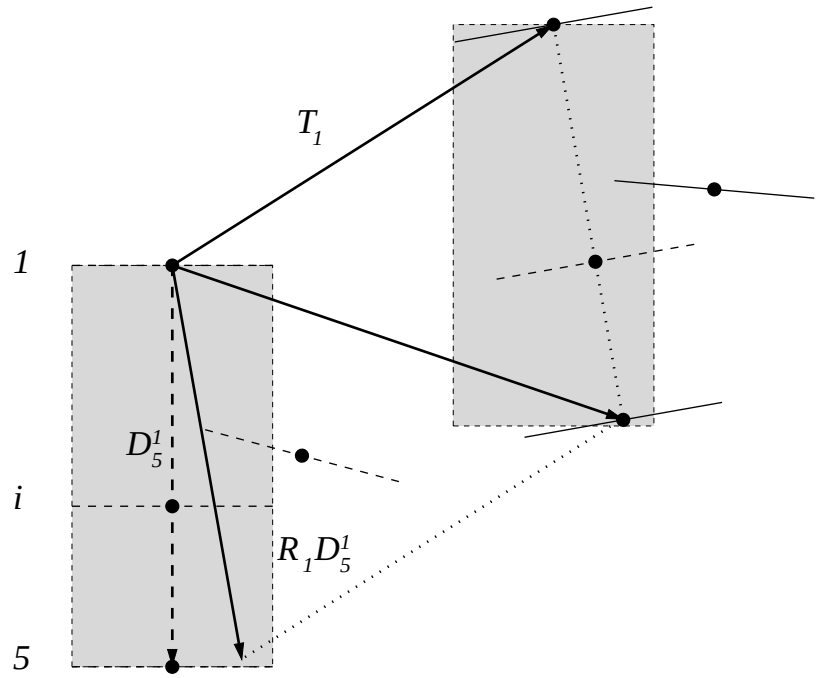


Figure 4.13: *Sketch of the vectors involved in Eq. (4.20).*

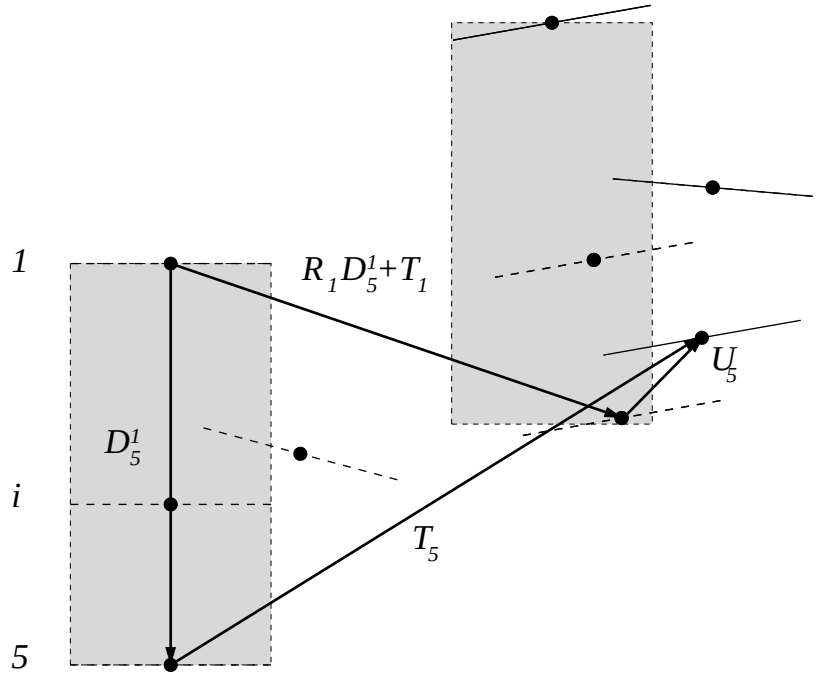


Figure 4.14: *Sketch of the vectors involved in Eq. (4.20).*

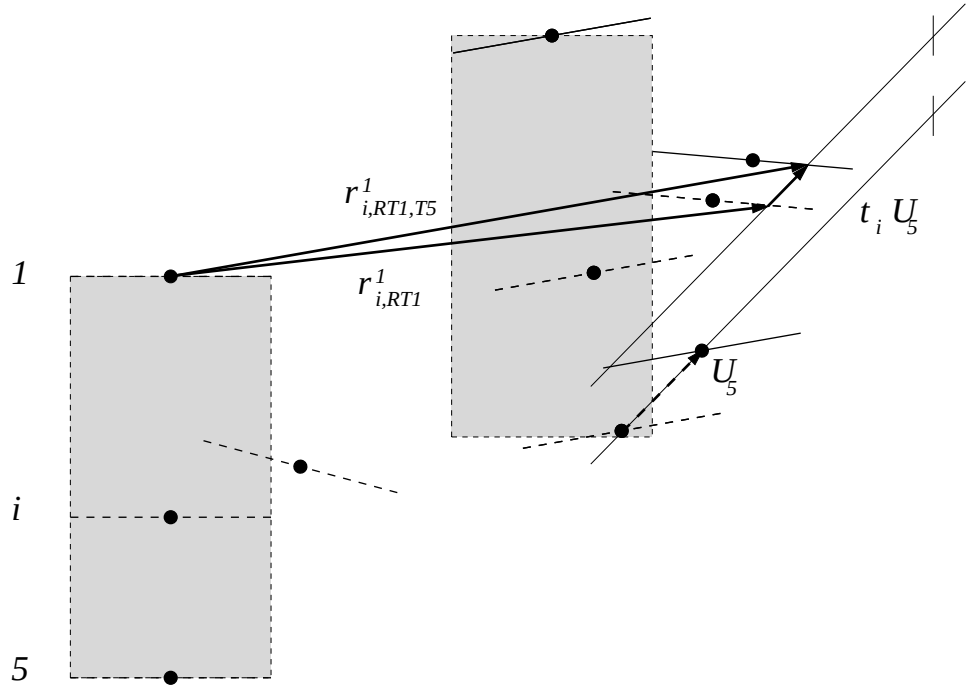




Figure 4.15: *Sketch of the vectors involved in Eq. (4.21).*

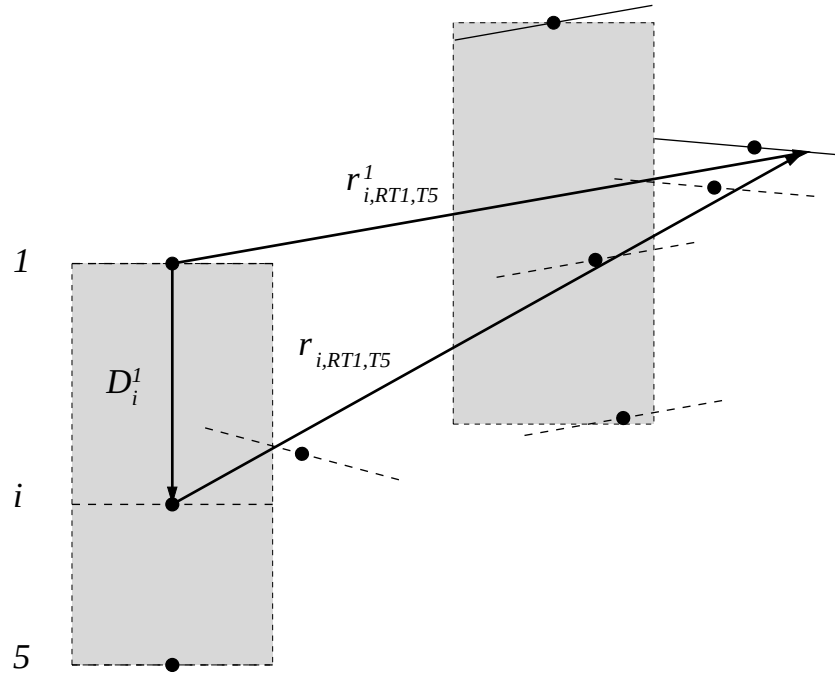


Figure 4.16: *Sketch of the vectors involved in Eq. (4.23).*

single-*tower* misalignment by means of the rotation $\mathsf{R}_i$ and the translation $\boldsymbol{T}_i$. The vectors which are involved in this and in next equations are represented in Fig. 4.10 ÷ 4.16. In order to rototranslate the vector $\boldsymbol{r}_i''$ according to RT1, it has to be first expressed with respect to the ideal position of sensor 1, since that is the center of such rotation. This can be done simply as (see Fig. 4.11):

$$\boldsymbol{r}_i^1 \;=\; \boldsymbol{r}_i'' \;+\; \boldsymbol{D}_i^1 \;, \tag{4.18}$$

where $\boldsymbol{D}_i^1 = \boldsymbol{S}_i - \boldsymbol{S}_1$ represents the vector which connects sensor 1 to sensor $i$ in the mechanical design configuration. Now the rigid-body transformation RT1, defined by the rotation $\mathsf{R}_1$ and by the translation $\boldsymbol{T}_1$, can be performed as (see Fig. 4.12):

$$\boldsymbol{r}^1_{i,\mathrm{RT1}} \;=\; \mathsf{R}_1\, \boldsymbol{r}^1_i \;+\; \boldsymbol{T}_1\,. \tag{4.19}$$

The reference sensor 5 is also affected by RT1 and as a consequence it is moved in the position identified by $(\,\mathsf{R}_1\;\boldsymbol{D}^1_5 + \boldsymbol{T}_1)$, as it is shown in Fig. 4.13. However, this in general is not the place where it had to stay according to the transformation T5 that we require. Therefore it has to be translated by a certain vector $\boldsymbol{U}_5$ which fulfills:

$$(\,\mathsf{R}_1\;\boldsymbol{D}^1_5 + \boldsymbol{T}_1\,) \;+\; \boldsymbol{U}_5 \;=\; \boldsymbol{D}^1_5 \;+\; \boldsymbol{T}_5\,, \tag{4.20}$$

where $\boldsymbol{T}_5$ is the translation which identifies the real position of sensor 5 respect to its design configuration (see Fig. 4.14). As a consequence of T5 the other sensors shift by a vector which is proportional to $\boldsymbol{U}_5$ according to their distance from sensor 5 (see Fig. 4.15):

$$\boldsymbol{r}^1_{i,\mathrm{RT1,T5}} \;=\; \boldsymbol{r}^1_{i,\mathrm{RT1}} \;+\; t_i \cdot \boldsymbol{U}_5\,, \tag{4.21}$$

where:

$$t_i \;=\; \left|\frac{Z_i - Z_1}{Z_5 - Z_1}\right|\,, \tag{4.22}$$

and where $\boldsymbol{r}^1_{i,\mathrm{RT1,T5}}$ is the final vector which was looked for, but still expressed respect to the ideal center of sensor 1. Going back to its own center (see Fig. 4.16):

$$\boldsymbol{r}_{i,\mathrm{RT1,T5}} \;=\; \boldsymbol{r}^1_{i,\mathrm{RT1,T5}} \;-\; \boldsymbol{D}^1_i\,, \tag{4.23}$$

the final position of the $i$-th sensor after the transformations TR1 and T5 is obtained. Tracing back from Eq. (4.23) to Eq. (4.17), this can be expressed as a single rotation $\hat{\mathsf{R}}_i$ and a single translation $\hat{\boldsymbol{T}}_i$ of the point in order to go from its measured coordinates $\boldsymbol{r}'_i$ to the new ones $\boldsymbol{r}_{i,\mathrm{RT1,T5}}$:

$$\boldsymbol{r}_{i,\mathrm{RT1,T5}} \;=\; \hat{\mathsf{R}}_i \; \boldsymbol{r}'_i \;+\; \hat{\boldsymbol{T}}_i \tag{4.24}$$

if we identify:

$$\hat{\mathsf{R}}_i \;=\; \mathsf{R}_1 \; \mathsf{R}_i \;, \tag{4.25}$$

and:

$$\hat{\boldsymbol{T}}_i \;=\; \mathsf{R}_1 \; (\boldsymbol{T}_i + \boldsymbol{D}_i^1) + \boldsymbol{T}_1 - \boldsymbol{D}_i^1 + t_i \cdot (\boldsymbol{D}_5^1 \;+\; \boldsymbol{T}_5 - \mathsf{R}_1 \; \boldsymbol{D}_5^1 - \boldsymbol{T}_1) \;. \tag{4.26}$$

These equations allow to calculate how the rototranslation parameters $\mathsf{R}_i$ and $\boldsymbol{T}_i$ obtained from the single-*tower* alignment procedure have to be modified in order to preserve the relative alignment of the sensors, when the reference elements 1 and 5 are let free to vary.

As in the first part of the alignment process, here too it is not possible to define the configuration of the tracking system in an absolute frame of reference: a pair of elements have to be fixed and all the alignment parameters have to be associated to their position (again, this principle corresponds experimentally to the fact that the $\chi^2$ surface in the parameter space is flat along the directions corresponding to the movements of the reference elements). The solution that has been adopted consists in blocking the couple of reference sensors of a *tower* (L2-S1 is the one that has been chosen) to their ideal mechanical design positions. In this way the total number of free variables of the function to be minimized is 45: 5 *towers* $\times$ (6 + 3) parameters, namely ($\beta_1$, $\gamma_1$, $\omega_1$, $\Delta x_1$, $\Delta y_1$, $\Delta z_1$) and ($\Delta x_5$, $\Delta y_5$, $\Delta z_5$), where the subscript refers to the plane number[3].

A major difference between this procedure and the single-*tower* alignment consists in the characteristics of the tracks that are used to find the

[3]The number of free variables that is actually needed for the final minimization is 45, but during the analysis of the behavior of the function a larger number of internal free variables was needed. Since the released version of MINUIT is able to manage only 50 simultaneously varying parameters, it has been necessary to obtain the source code of the software and recompile the package by changing this maximum limit.

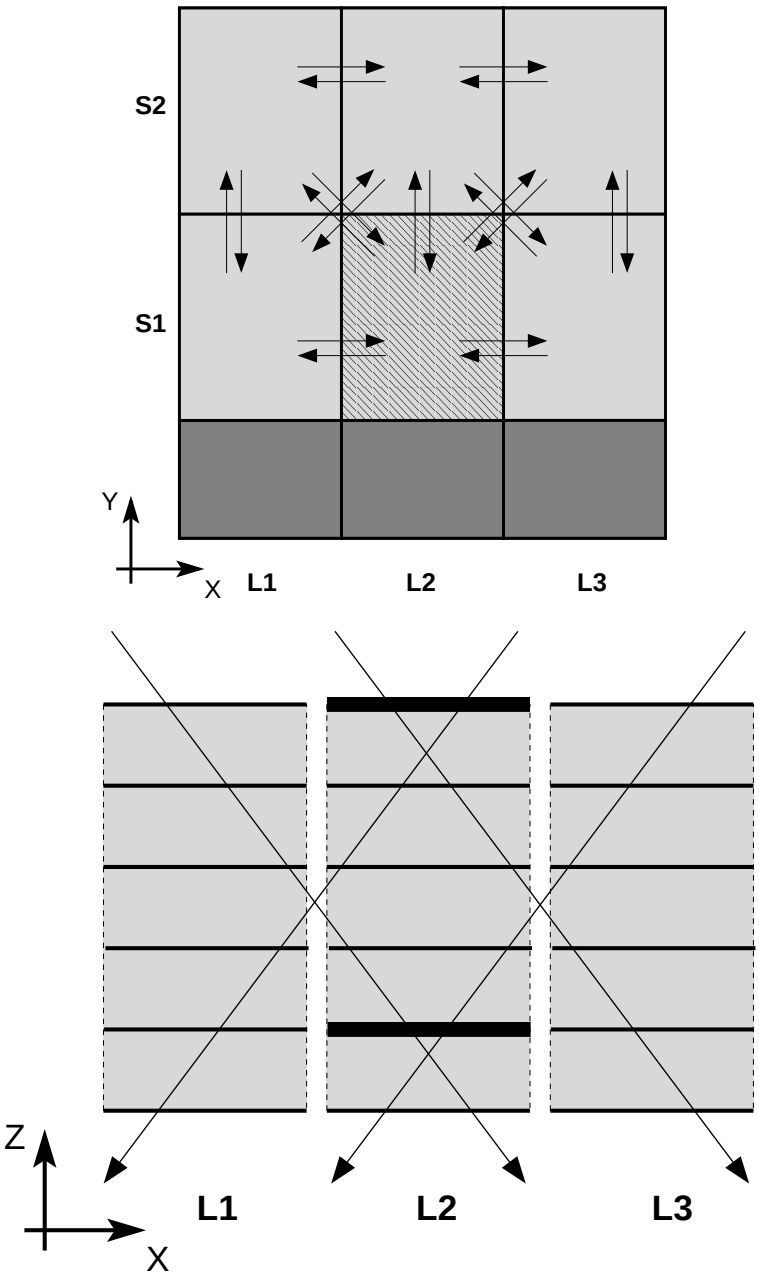


Figure 4.17: *Representation of the 22 sets of tracks selected for the whole-tracker alignment. In the upper and lower part of the figure the X-Y and X-Z cross sections of the spectrometer are shown. The pair of sensors which are kept fixed as reference in the minimization are highlighted.*

residuals and build the $\chi^2$ function. First of all, as it has been anticipated at the beginning of the section, track are selected among cosmic rays which cross more than a *tower* at the same time: this creates the needed "connection" between the up-to-now independent sets of alignment parameters. The possible combinations of hit sensors which can be obtained are depicted in Fig. 4.17. In particular, those trajectories are chosen which cross the first three elements of a *tower* and the last three of an adjacent one. Moreover, since now cosmic rays are used, the value of the deflection is not known *a priori* as in the case of the alignment with test-beam data. This issue is nonetheless resolved by the particular choice of selected tracks: each of the two groups of three sensors which they hit in turn, have already been corrected for their internal misalignments (since they belong to a single *tower*), so that the value of the deflection of the particle, which is let free to vary event-by-event in the minimization, is actually constrained. When, during the research of the minimum, the parameters of a reference sensor of a *tower* are modified, those of the other elements of that *tower* will change too according to Eq. (4.25) and (4.26) in order to keep them self-aligned, while the position of the whole *tower* will be modified respect to the other ones in such a way that the impact points are better fitted by the reconstructed trajectory.

The sample of events that has been used consists in cosmic-ray data which had been acquired in Rome in the first months of 2005 during the final stages of hardware integration and software debugging of PAMELA, before it was transported to Russia. The selection follows criteria similar to those described in Sec. 4.2.1, but with some variations due to the different required track geometry and characteristics of the "beam". In particular, incidence angles up to the acceptance limit are now possible and all the surface of the detectors is in this case illuminated. Moreover, additional cuts on the $\chi^2$ and on the particle rigidity obtained from a first-estimate fit are performed, in order to lower the effect of multiple scattering, which is now no more negligible as in the case of the 50-GeV/$c$ proton beam.

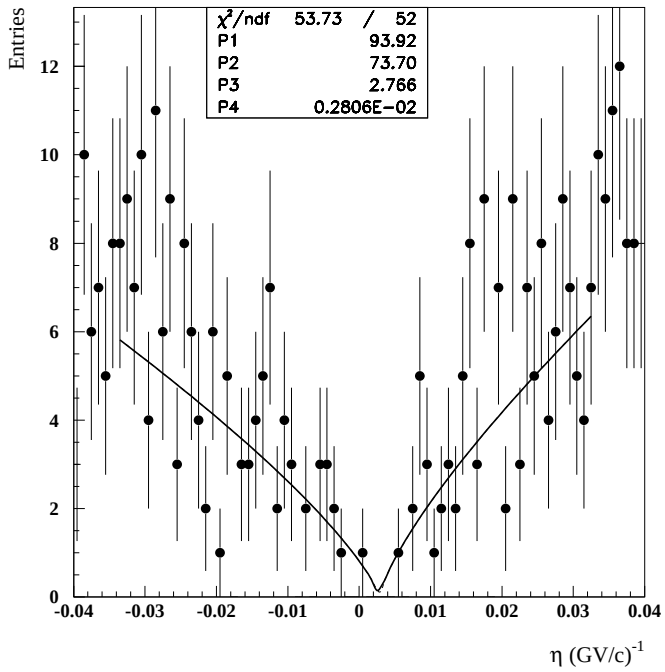


Figure 4.18: *Detail of the high-energy region of the deflection distribution of cosmic rays at ground level, after the test-beam alignment procedure has been applied. A fit of the data is reported too: a shift with respect to* $\eta = 0$ *(GV/c)*$^{-1}$*, of the minimum of the distribution, which correspond to the highest rigidity region, can be noticed.*

## 4.4 Correction of the single-tower parameters

A first analysis of the cosmic rays acquired at ground level has been performed, using the alignment parameters which result from the single-*tower* alignment, done by means of test-beam data. As it has been explained at the beginning of Sec. 4.3, this is not the optimal way to proceed in order to measure cosmic-ray events, since if a particle crosses two *towers*, the trajectory will be reconstructed with large uncertainties be-

cause their reciprocal misalignments have not been taken into account. Yet, this kind of study has been useful in order to point out an issue about the application of the test-beam parameters to the analysis of ground data.

For tracks which hit only one of the six *towers*, these corrections should allow to measure correctly particle deflection, as showed in Sec. 4.2.2 for the CERN data. On the contrary, if tracks which are fully contained in a *tower* are selected, and the distribution of their measured deflection is plotted, as in Fig. 4.18, it can be seen that the minimum which corresponds to the highest values of rigidity is not located in $\eta = 0$ $(\mathrm{GV}/c)^{-1}$ as it should be. Moreover, if the residuals are examined, it can be seen that the distributions are not properly centered on zero, but shifted randomly by quantities of the order of some micrometers (see Fig. 4.19). This shows that the alignment parameters that have been used are not able to correct completely the misalignments of the sensors, for the data set which have been analyzed. Since the offsets of the six sensors belonging to a same plane of the spectrometer are similar (the plots contain the results obtained for six samples of cosmic-ray events which hit each *tower*, all added up together) and are compatible with a rigid movement of theirs, the simpler explanation is that displacements of the whole planes have happened. Actually, in addition to the mechanical stresses which could have possibly occurred during the transport of the instrument, the major event which could have determined these further misalignments, in between the test-beam at CERN in 2003 and the acquisition of cosmic rays in Rome in 2005, was a vibration test session which took place in Munich on the PAMELA detector. A rigid movement of the six sensors of a plane is mechanically compatible with the effects of such vibrations on the aluminium frame which contains the silicon detectors, and which is connected to the structure of the magnet by means of simple screws (see also Fig. 2.12). In order to correct for this further displacements which have occurred since the test-beam alignment, the single-*tower* parameters have to be changed, since those which have been used to analyze cosmic-ray data do not correspond anymore to the physical configuration with which particles were acquired.

The strategy that has been adopted is a sort of "second-order" cor-

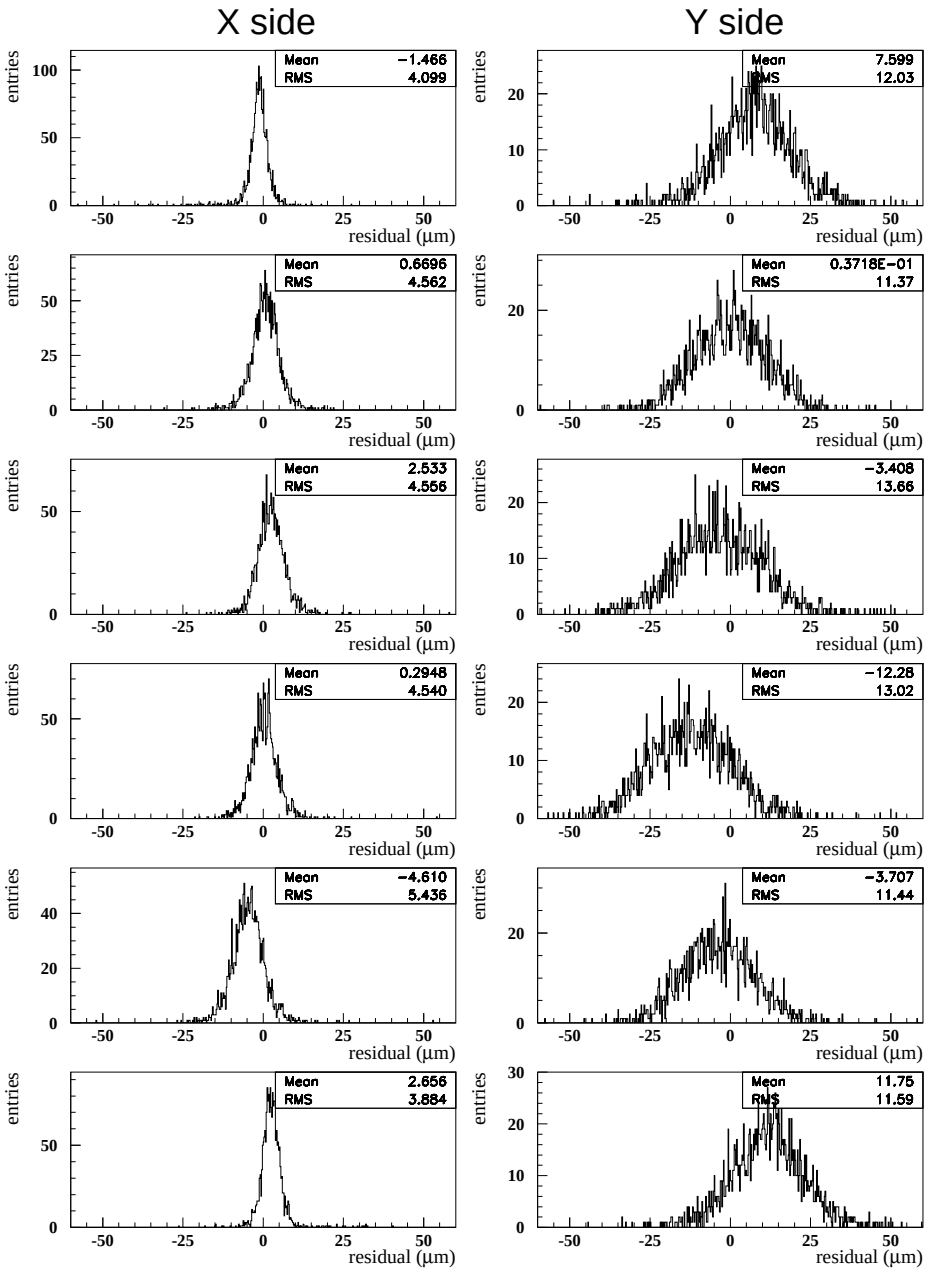


Figure 4.19: *Distributions of the differences between the points measured on the sensors and those obtained from the track fitting, after the test-beam alignment procedure has been applied. The plots contain the results corresponding to six samples of cosmic-ray events which hit each* tower*, all added up together, and suggest that a displacement of the whole planes has occurred respect to the test-beam configuration of the tracking system.*

rection of the rotations and the translations of the sensors, by means of the single-*tower* alignment procedure, which is now applied to ground cosmic-ray data. A crucial issue that has to be dealt with is, again, the lack of the knowledge of the rigidity of particles. During the flight, as it will be explained in next Sec. 4.5, the alignment will be performed using tracks of electrons, whose energy can be measured by means of the calorimeter. On ground this technique cannot be used, since the number of high-energy electrons is too small to obtain a reliable result: most of the particles are in fact minimum-ionizing muons which do not produce a shower in the calorimeter and whose energy cannot be therefore measured independently of the spectrometer. As it has been shown in Fig 4.18, if the deflection is determined after correcting the measured coordinates through the improper set of parameters, a systematically shifted value is found. Since the minimum of the distribution is a characteristic feature of the cosmic-ray spectrum, it can be used as a way to correct the alignment procedure, in the hypothesis that this deflection offset is the same for all the tracks and that the shape of the $\eta$ distribution is not affected by it.

After selecting a set of "clean" events which hit a single *tower* of sensors, the impact points of each track are corrected according to the test-beam alignment parameters and the trajectory is reconstructed. The biased value of the deflection which is obtained is then modified by means of the calculated offset in the $\eta$-distribution minimum (see Fig. 4.18), according to the reasonable hypothesis, confirmed by the analysis of the distribution of the residuals, that the systematic error is due to random rigid rototranslations of each whole plane of six sensors. The correction that is found is of the order of $10^{-3}$ $(\mathrm{GV}/c)^{-1}$. The updated value of the deflection is then used to align each *tower* according to the procedure described in Sec. 4.2.

As a check of the procedure, the distributions of residuals of tracks whose impact points have been corrected by means of the new set of alignment parameters can be used. Actually, the lack of shifts in the residuals is not sufficient by itself in assuring that the right corrections have been determined: in fact, an appropriate misalignment of the sensors, such as a "coherent" bending, can result in a systematic error in the measure

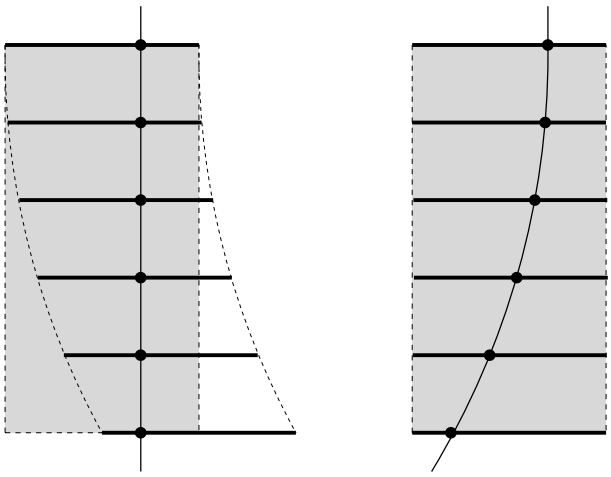

Figure 4.20: *Sketch of a particular class of plane misalignments which can result in an incorrect measurement of the deflection of particles without noticeable offsets in the distribution of residuals. A track reconstructed with a certain deflection $\eta \neq 0$ and with centered residuals (as on the right) in the hypothesis of an aligned system, could correspond in reality to a particle with a different deflection ($\eta = 0$ in this example) if the tracker is deformed in a "coherent" way as in the left part of the figure.*

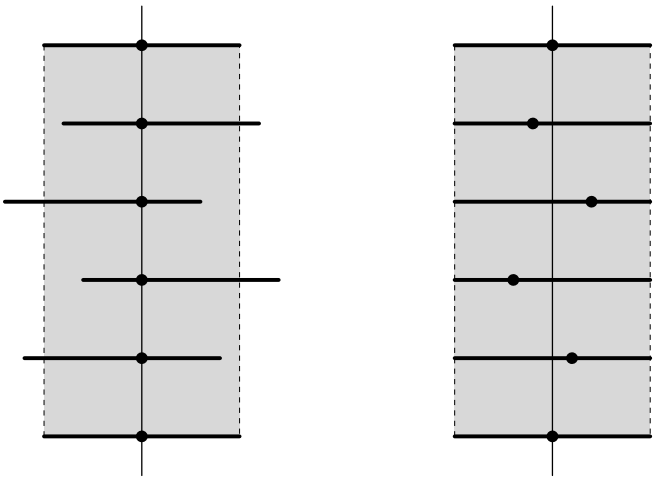

Figure 4.21: *Sketch of a particular class of plane misalignments in which random displacements give rise to residuals which are not centered, but to a null systematic effect on deflection on average. Starting from the true configuration of the system on the left, other alignment configurations can be found (as on the right) which, in spite of being different from the correct one, result in the right value for the deflection, but also in non-zero offsets in the residuals.*

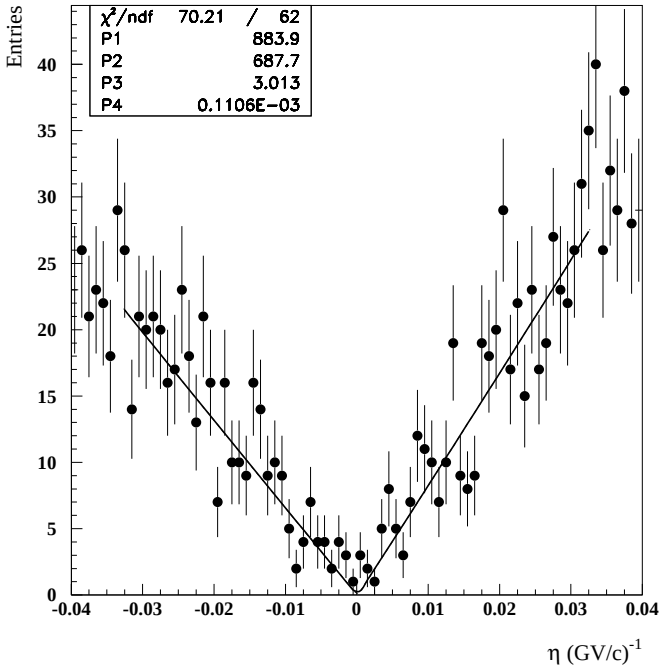


Figure 4.22: *Detail of the high-energy region of the deflection distribution of cosmic rays at ground level, after the correct single-*tower *alignment has been applied. The fitted value of the minimum of the distribution shows that no evidence for a systematic shift can be inferred.*

of the deflection without the residuals being not centered on zero (see Fig. 4.20). This is the reason why the correction of the test-beam parameters cannot be done simply by shifting the sensors in order to cancel the offsets in the residuals: that procedure would correspond to aligning the spectrometer around a biased value of the curvature of the tracks and would not remove the systematic effect on the deflection. Conversely, also the condition alone that no offset appears in the measured $\eta$ distribution is not enough, because random displacements can balance their effects and give rise to an average null systematic error, even if sensors are not really aligned and residuals are not centered (see Fig. 4.21). On

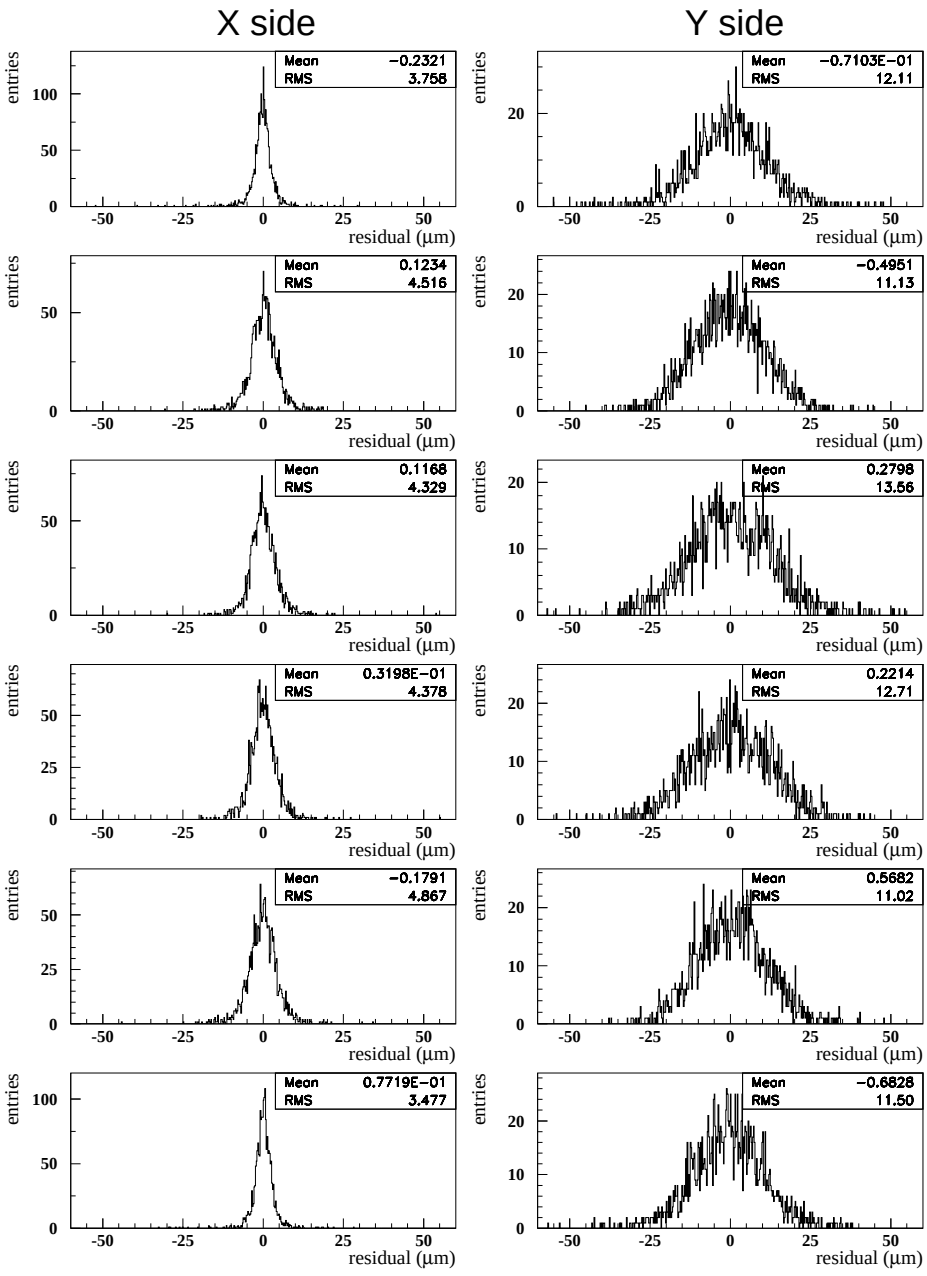


Figure 4.23: *Distributions of the differences between the points measured on the sensors and those obtained from the track fitting, after the correct single-*tower *alignment. The plots contain the results obtained for six samples of cosmic-ray events which hit each* tower*, all added up together.*

| | | L 1 - S 1 | | L 1 - S 2 | | L 2 - S 1 | | L 2 - S 2 | | L 3 - S 1 | | L 3 - S 2 | |
|---|---|---|---|---|---|---|---|---|---|---|---|---|---|
| | | Value | Error | Value | Error | Value | Error | Value | Error | Value | Error | Value | Error |
| PLANE 1 | $\beta$ | -1.031E-05 | 7.3E-07 | 1.12E-05 | 1.1E-06 | 0. | FIXED | 1.635E-05 | 7.4E-07 | -1.76E-05 | 1.1E-06 | 9.E-07 | 1.1E-06 |
| | $\gamma$ | -4.53E-06 | 5.9E-07 | 1.406E-05 | 7.6E-07 | 0. | FIXED | -7.29E-06 | 7.0E-07 | -3.72E-06 | 9.4E-07 | -8.5E-07 | 6.3E-07 |
| | $\omega$ | 1.18E-06 | 1.6E-07 | 1.46E-06 | 1.9E-07 | 0. | FIXED | -2.21E-06 | 1.0E-07 | -3.5E-07 | 2.0E-07 | 2.09E-06 | 1.4E-07 |
| | $\Delta x$ | 10.7 | 1.5 | 20.9 | 1.9 | 0. | FIXED | -17.9 | 1.5 | 22.0 | 1.7 | 19.5 | 1.8 |
| | $\Delta y$ | -21.4 | 1.6 | -14.7 | 1.6 | 0. | FIXED | -18.0 | 1.3 | -9.9 | 2.1 | -9.0 | 1.9 |
| | $\Delta z$ | 120.6 | 4.9 | 89.6 | 6.0 | 0. | FIXED | 85.2 | 4.2 | 9.2 | 8.4 | 165.0 | 7.0 |
| PLANE 2 | $\beta$ | 0.8 | 1.2 | -0.5 | 1.2 | 0.4 | 1.0 | 0.9 | 1.0 | 2.0 | 1.4 | 1.9 | 1.4 |
| | $\gamma$ | -1.23 | 0.85 | -3.05 | 0.88 | 2.86 | 0.63 | 1.07 | 0.54 | 4.9 | 1.1 | 3.1 | 1.0 |
| | $\omega$ | -0.942 | 0.029 | -0.738 | 0.028 | -0.583 | 0.030 | -0.547 | 0.030 | -0.828 | 0.042 | -0.728 | 0.043 |
| | $\Delta x$ | 153.06 | 0.23 | 218.78 | 0.23 | 158.76 | 0.25 | 190.96 | 0.25 | 159.83 | 0.31 | 213.06 | 0.32 |
| | $\Delta y$ | 651.03 | 0.69 | 643.48 | 0.70 | 616.27 | 0.68 | 602.43 | 0.66 | 581.31 | 0.70 | 579.12 | 0.69 |
| | $\Delta z$ | 30. | 14. | 25. | 15. | -37.1 | 9.9 | 54.4 | 9.1 | -156.3 | 9.8 | 18.5 | 9.7 |
| PLANE 3 | $\beta$ | -2.1 | 1.1 | -1.2 | 1.1 | -0.3 | 1.0 | -1.7 | 1.0 | 0.3 | 1.1 | 0.4 | 1.1 |
| | $\gamma$ | 2.43 | 0.77 | 1.92 | 0.82 | 1.93 | 0.60 | 3.05 | 0.53 | 0.9 | 1.2 | 1.0 | 1.2 |
| | $\omega$ | 1.505 | 0.033 | 1.582 | 0.033 | 1.431 | 0.035 | 1.487 | 0.036 | 1.438 | 0.045 | 1.643 | 0.044 |
| | $\Delta x$ | 135.56 | 0.25 | 31.89 | 0.25 | 129.25 | 0.22 | 27.11 | 0.23 | 126.72 | 0.28 | 15.96 | 0.26 |
| | $\Delta y$ | 484.10 | 0.63 | 486.36 | 0.63 | 571.94 | 0.65 | 553.52 | 0.64 | 618.44 | 0.73 | 626.14 | 0.71 |
| | $\Delta z$ | 238. | 10. | 119. | 11. | 64.1 | 6.3 | 42.1 | 7.0 | -49.8 | 9.9 | -9.3 | 8.4 |
| PLANE 4 | $\beta$ | -1.6 | 1.1 | -1.4 | 1.2 | 1.55 | 0.82 | -1.06 | 0.82 | 1.8 | 1.0 | 0.5 | 1.0 |
| | $\gamma$ | 4.00 | 0.92 | 0.89 | 0.92 | -1.09 | 0.72 | 0.60 | 0.68 | -1.6 | 1.7 | -1.9 | 1.7 |
| | $\omega$ | 1.655 | 0.042 | 1.699 | 0.042 | 1.592 | 0.039 | 1.530 | 0.041 | 1.797 | 0.047 | 1.923 | 0.046 |
| | $\Delta x$ | -12.64 | 0.25 | -123.78 | 0.26 | -34.16 | 0.21 | -138.59 | 0.23 | 9.95 | 0.22 | -120.97 | 0.22 |
| | $\Delta y$ | -631.29 | 0.67 | -634.84 | 0.67 | -553.32 | 0.67 | -560.41 | 0.64 | -459.08 | 0.76 | -462.04 | 0.72 |
| | $\Delta z$ | 69. | 10. | -20. | 10. | -18.8 | 6.7 | -49.2 | 6.6 | -16. | 15. | -30. | 14. |
| PLANE 5 | $\beta$ | -1.031E-05 | 7.3E-07 | 1.12E-05 | 1.1E-06 | 0. | FIXED | 1.635E-05 | 7.4E-07 | -1.76E-05 | 1.1E-06 | 9.E-07 | 1.1E-06 |
| | $\gamma$ | -4.53E-06 | 5.9E-07 | 1.406E-05 | 7.6E-07 | 0. | FIXED | -7.29E-06 | 7.0E-07 | -3.72E-06 | 9.4E-07 | -8.5E-07 | 6.3E-07 |
| | $\omega$ | 1.447 | 0.038 | 1.497 | 0.038 | 1.771 | 0.039 | 1.565 | 0.041 | 1.284 | 0.045 | 1.448 | 0.043 |
| | $\Delta x$ | -34.85 | 0.95 | -137.5 | 1.2 | 0. | FIXED | -100.52 | 0.92 | -26.7 | 1.0 | -128.5 | 1.1 |
| | $\Delta y$ | -78.3 | 1.1 | -83.7 | 1.1 | 0. | FIXED | 1.46 | 0.99 | 79.9 | 1.5 | 82.1 | 1.4 |
| | $\Delta z$ | -21.5 | 3.5 | -133.6 | 3.4 | 0. | FIXED | -145.8 | 2.6 | -103.5 | 4.3 | -229.1 | 4.9 |
| PLANE 6 | $\beta$ | 0.26 | 0.94 | 4.04 | 0.93 | 2.12 | 0.67 | 5.05 | 0.69 | 1.99 | 0.91 | 5.79 | 0.92 |
| | $\gamma$ | 3.3 | 1.3 | 3.8 | 1.4 | 4.36 | 0.74 | 2.83 | 0.76 | -4.9 | 2.3 | -6.1 | 2.3 |
| | $\omega$ | 2.834 | 0.038 | 2.958 | 0.037 | 1.987 | 0.039 | 1.973 | 0.040 | 1.449 | 0.046 | 1.524 | 0.044 |
| | $\Delta x$ | -303.73 | 0.28 | -499.32 | 0.31 | -280.22 | 0.25 | -388.50 | 0.26 | -319.64 | 0.29 | -429.81 | 0.28 |
| | $\Delta y$ | -2008.56 | 0.89 | -2015.67 | 0.89 | -1854.57 | 0.85 | -1878.52 | 0.84 | -1783.2 | 1.0 | -1787.7 | 1.0 |
| | $\Delta z$ | 643.4 | 9.1 | 494.6 | 9.6 | 427. | 10. | 319.7 | 9.0 | 483. | 34. | 431. | 34. |

Table 4.3: *Whole-tracker alignment parameters. The rotation angles $\beta$, $\gamma$ and $\omega$ are in milliradians, while the translations $\Delta x$, $\Delta y$ and $\Delta z$ are in micrometers.*

the contrary, if both the residuals are centered and the deflection distribution has its minimum in zero, this means that the correct parameters have been determined, since if random misalignments were present the former condition would have not been fulfilled, and the same would happen to the latter if a "coherent" bending were present. The measure of $\eta$ which is obtained from cosmic rays after the improved single-*tower* alignment is reported in Fig. 4.22, while the associated residuals are shown in Fig. 4.23.

Once the set of single-*tower* parameters which actually corresponds to the detector configuration at the time of acquisition has been determined, the whole-tracker alignment can be performed, according to the procedure which has already been described in Sec. 4.3. Tab. 4.3 contains the values of the parameters for the 34 free sensors respect to the pair belonging to the *tower* L2-S1 which has been chosen as reference, while Fig. 4.24 and Fig. 4.25 show the residuals and the deflection distribution which are obtained when these parameters are used in the analysis of cosmic-ray data acquired at ground level.

## 4.5 In-flight alignment with cosmic rays

The alignment parameters that have been obtained with the procedures described till now allow to perform the data reduction of cosmic rays which have been acquired on ground with PAMELA. They will also be used as an initial set for the subsequent analysis of particles gathered during the flight of the satellite, but their validity for the in-orbit conditions will have to be checked and updated if necessary. In fact, as a difference of some micrometers in the positions of the planes of the spectrometer has been noticed from the last test on a particle beam to the acquisition of cosmic rays during the detector integration in Rome, after a vibration test session, in the same way it is possible that in the following period of time further misalignments occurred, or that they will occur, in particular in the launch phase of the rocket. For this reason a periodic calibration of the correction parameters is foreseen during the entire lifetime of the mission.

The methods which have been developed can be employed in order to

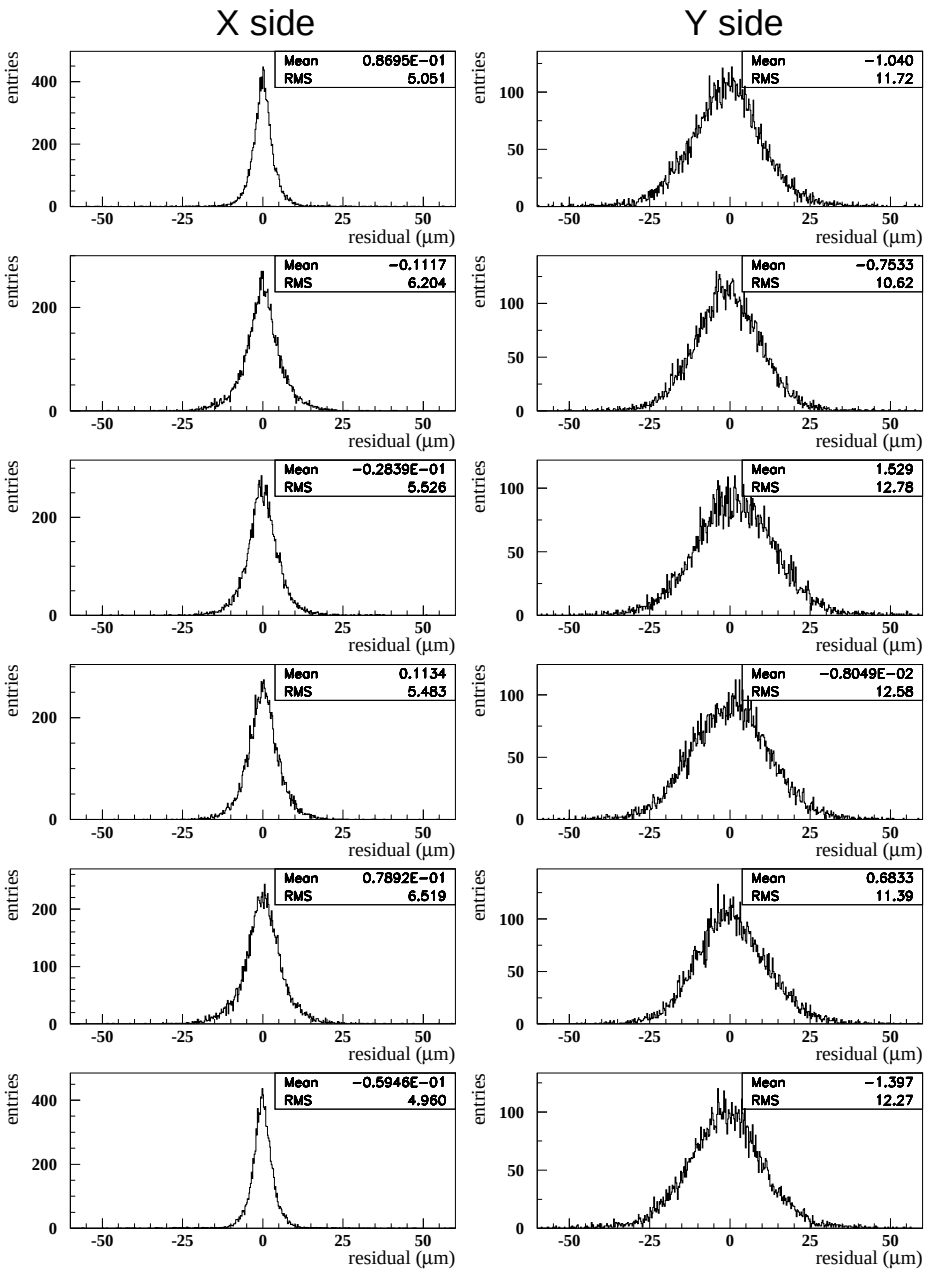


Figure 4.24: *Distributions of the differences between the points measured on the sensors and those obtained from the track fitting, after the whole-tracker alignment. The plots contain the results obtained for a sample of cosmic-ray events which hit any combination of sensors.*

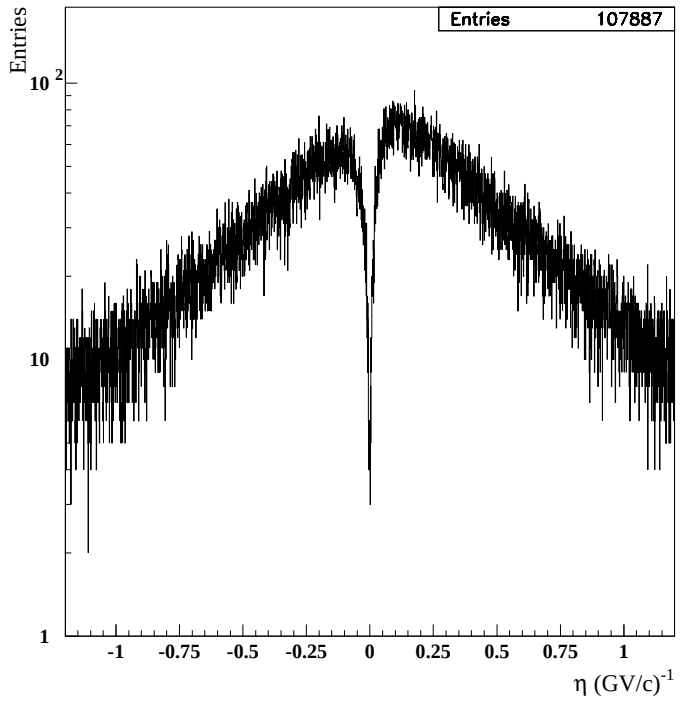


Figure 4.25: *Deflection distribution of cosmic rays at ground level, after the whole-tracker alignment has been applied. The larger abundance of positive particles can be noticed.*

accomplish this task, both as regards the preliminary alignment of each *tower*, as well as for the complete one. However, some aspects of the process will have to be adapted to the changed experimental conditions. Indeed, the availability of particles hitting the whole surface of sensors, and with all the incidence angles that are allowed by the acceptance of the instrument, will permit to determine the entire set of rototranslation parameters with a better accuracy than as it has been possible by means of the partially limited area and inclination of an artificial beam of particles. On the other hand, a main difference in the procedure will be the fact that the value of the deflection needed to determine the configuration of the

sensors will have to be obtained by means of the energy measurement provided by the calorimeter of PAMELA. This instrument, as explained in Sec. 2.5.1, is able to identify particles which interact electromagnetically and to measure their energy. For what concerns the alignment procedure, it will be used in particular to isolate a suitable sample of electrons whose tracks have been reconstructed by the spectrometer: thanks to the information on the particle energy coming from the calorimeter, the deflection can be calculated and the algorithm applied. The main factors that have to be taken into account in such approach are the resolution of the calorimeter in providing the energy measurement and the available statistics of electrons in cosmic rays. While the former issue in practice limits the useful energy range to $E > 5$ GeV in order to have a resolution better than 7%, the latter gives a upper limit to about 100 GeV. Estimates done on the basis of the electron flux measured by previous experiments in relation to the geometrical acceptance of PAMELA [74], show that it should be possible to gather sufficient statistics in that energy range for the alignment of the single *towers* of the tracking system in about 3 months of data taking.

# Chapter 5

# Data analysis of cosmic rays at ground level

*In a period of about two months, from the beginning of February till the end of March 2005, PAMELA has been being used to detect cosmic rays at ground level. This represents the first acquisition that has been done with the complete and fully functional detector configuration. The cosmic-ray events have been processed according to the data reduction procedures described in Chapters 3 and 4, and they have been used for an analysis of the muon component at ground level, as reported in this chapter.*

## 5.1 Measurement of muon charge ratio

Charged particles which arrive to the surface of the Earth consist in the secondary products of the interaction of cosmic rays in the atmosphere: as described in Sec. 1.2, muons represent the most abundant component at ground level. The magnetic deflection $\eta$ of the cosmic rays which have been acquired during the integration of the various subsystems and the associated debugging phase, as measured by means of the spectrometer of PAMELA, has been shown in Fig. 4.25.

The data analysis performed to obtain this all-particle distribution has been integrated with the calorimeter discrimination capabilities, in

order to reduce the $p$ and $e^{\pm}$ contamination and isolate a $\mu^{\pm}$ sample. This has allowed to measure the muon charge ratio as a function of rigidity at ground level. Particles which have been gathered in Rome (Lat. 41° 51′ N, Long. 12° 36′ E) are associated to a geomagnetic latitude $\lambda \simeq 41.85°$. The corresponding geomagnetic cut-off for the cosmic primaries can be evaluated by means of Eq. (1.4), and results:

$$R_{\text{cut-off}} \simeq 4.6 \text{ GV}/c \,. \tag{5.1}$$

The rejection of proton, electron and positron events has been performed with a series of cuts on a set of characteristic quantities, which are related to the features of the interaction and of the energy release of these particles in the calorimeter. The cuts have been calibrated on the basis of the analysis of test-beam data and of simulations of the detector for different particles at several energies [75]. In particular, among the variables which are calculated during the calorimeter data-reduction process, those that have been used are:

- **nstrips**, which is the total number of hit silicon strips in the 22 couples of X and Y detecting layers;
- **qtot**, which represents the total energy measured in the whole calorimeter, expressed in *mip*, which is the energy released in a sensor by a high-energy particle at its ionization minimum;
- **planetot**, which represents the number of layers in which an energy deposit has been identified at a distance lower than 1 cm from the extrapolated trajectory of the particle, as measured by the spectrometer;
- **qmean**, which is the average value of the energy in *mip*, calculated on the five layers where the smallest release has been measured.

The contamination due to $e^{\pm}$ and to the fraction of $p$ which interact in the tungsten absorbers, is rejected through a selection on *nstrips* and *qtot*, while the non-interacting protons, which as regards these variables

have a behavior similar to that of muons, are discriminated by means of cuts on *planetot* and *qmean* for energies lower than about 1 GeV.

In fact by analyzing test-beam and simulated data, it can be seen that while for $\mu$ the number of hit strips as they pass through the calorimeter is usually 44 (one for each silicon layer they cross), for interacting particles *nstrips* is significantly larger, due to the production of secondaries. Likewise, the total energy released in the calorimeter is accordingly different, since muons tend to lose energy only because of ionization[1], and as a consequence they show a peak at about 50 *mip* in the distribution of *qtot*, while $e^{\pm}$ and interacting $p$ result in particle showers and higher energy deposits.

Due to the low number of interaction lengths of the absorbing material with respect to radiation lengths (see Sec. 2.5.1) the interaction probability of protons in the calorimeter is small as compared to that of electrons and positrons. While being useful for lepton-hadron discrimination of particles in the upper part of the atmosphere, on the contrary this represents a drawback for the task of identifying muons in a ground cosmic-ray sample. In order to reject $p$ which do not generate showers large enough to have them excluded by the previously described selections, *planetot* and *qmean* are used. The first variable is used to discard events where the number of hits along the trajectory which is expected on the basis of the spectrometer track reconstruction is lower than a given threshold. Mostly important, the second quantity allows a separation to be performed thanks to the different ionization energy loss between protons and muons at low rigidity. In fact, for a given value of the energy below about 1 GeV, $\mathrm{d}E/\mathrm{d}x$ for $p$ is larger than for $\mu$, due to the difference in their masses. Hence with a cut on the energy measured on the detecting layers where no showers have been produced, these particles can be discriminated.

In summary, the muon selection conditions are:

- $nstrips < 60$ ,

- $qtot < 80$ ,

[1]The critical energy, at which radiative losses get as large as ionization losses, is above 150 GeV for muons in tungsten.

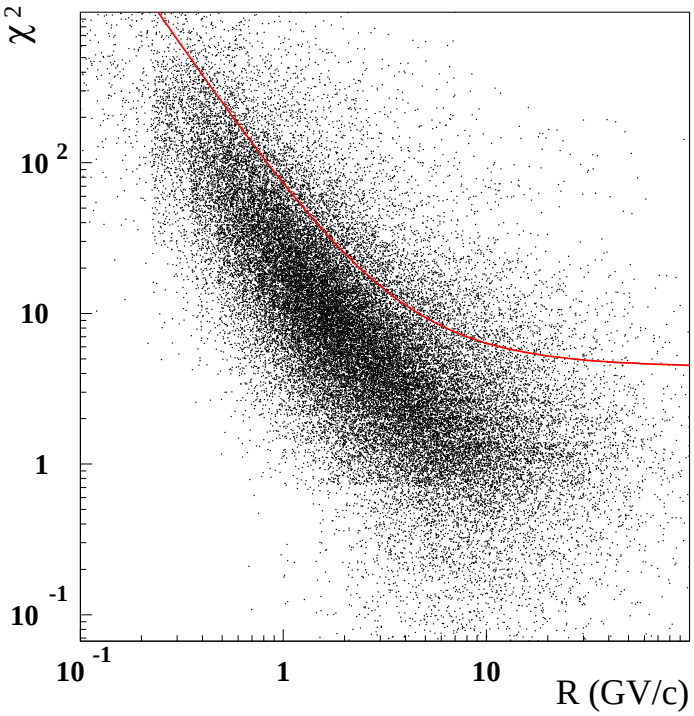


Figure 5.1: *Chi-square of reconstructed tracks as a function of rigidity. Events above the line are excluded.*

- *planetot* $> 5$ ,

- *qmean* less than a threshold depending on rigidity, which follows the functional behavior of the Bethe-Bloch equation.

As regards the spectrometer, the selection which has been done consists in choosing a set of well measured tracks, by requiring at least four measured hits out of six on the Y-Z projection of the trajectory, and five on the X-Z one. In addition the impact points in the bending plane are requested to belong to a set of planes that include both the most external ones, in order to assure the maximum track length (i.e. the best momentum resolution, as it can be seen from Eq. (2.9)). Finally, a

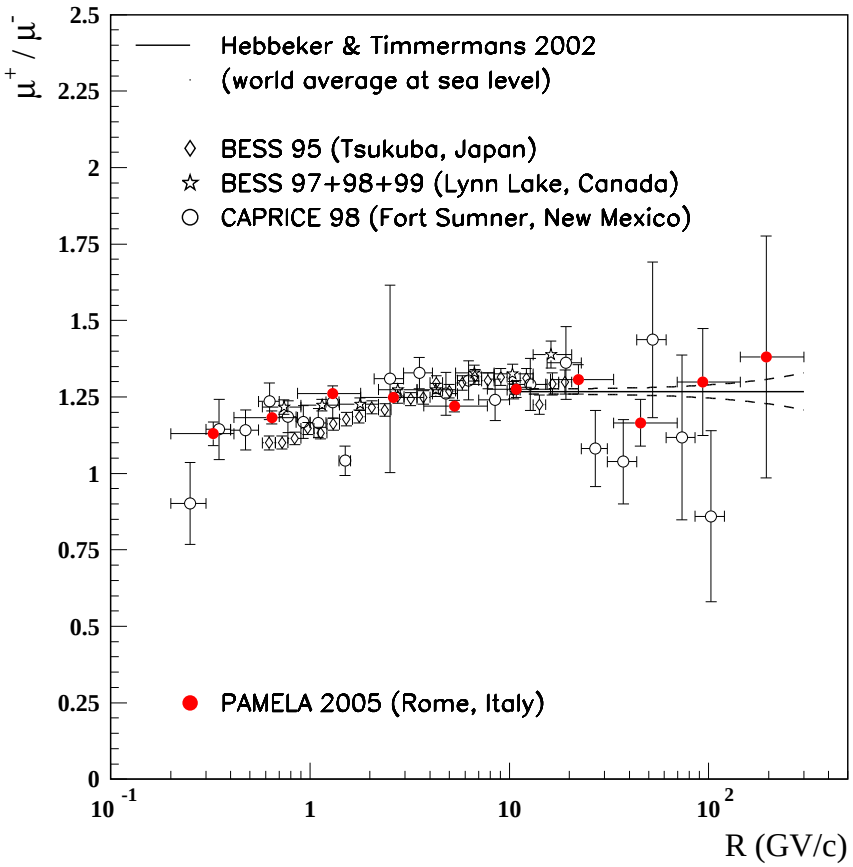


Figure 5.2: *Muon charge ratio at ground level. Filled circles represent PAMELA measurements, while other recent experimental results are reported as open symbols (References are BESS 95 and BESS 97+98+99 [76], CAPRICE 98 [77]). The line shows a world average at sea level as computed in Ref. [78].*

cut on the $\chi^2$ of the fit is performed to exclude the tracks which have not been well reconstructed. The chosen threshold is not constant but it depends on rigidity, in order to account for possible larger values of $\chi^2$ due to the effect of multiple scattering in case of low energy particles. The chi-square as a function of particle rigidity is shown in Fig. 5.1 as well as the applied cut.

The total number of particles which has been analyzed is 479060. The events that survive the selections are 90879, which correspond to about 19%. Positive and negative muons are separated on the basis of the sign of deflection, and their ratio as a function of rigidity is calculated. In general the efficiencies in the detection of particles at various energies should be taken into account when calculating the spectrum. Likewise, different selection efficiencies result from the cuts which have been applied in order to select the muon sample. When computing the ratio of the measured rigidity distributions these effects cancel out.

The muon charge ratio as measured at ground level by PAMELA in the rigidity range $0.3 \div 200$ GV/$c$ is shown in Fig. 5.2, where it is compared with a collection of other recent experimental results from BESS [76] and CAPRICE [77], and with a world average at sea level [78]. This quantity for high values of rigidity can give important indications of the possible presence of systematical effects on the deflection measurement. In fact if an offset is present, this is mostly evident by looking at the high rigidity region (which corresponds to low values of deflection: see the discussion reported in Sec. 4.4, and in particular Fig. 4.18). From Fig. 5.2 it can be seen that the ratio is in good agreement with the world average and with BESS and CAPRICE data within the reported statistical uncertainties on all the investigated range.

# Conclusion

In this work, an analysis of the first cosmic-ray data detected at ground level by the PAMELA experiment in 2005 has been presented.

The different steps of the data-reduction procedure of the magnetic spectrometer have been described in detail. After decompressing data, the signals generated on the silicon microstrip detectors of the tracking system are analyzed and the charge releases due to the passage of particles are identified. Impact-point coordinates are calculated by means of reconstruction procedures based on the application of the non-linear $\eta$ algorithm and on extensions of this technique, which allow to obtain a spatial resolution ranging from less than 3 to about 8 $\mu$m in the bending direction of particles inside the magnetic field, and between 8 and 14 $\mu$m on the perpendicular direction. From the measured points on the different planes of the spectrometer, the magnetic deflection of the particles can be calculated. To do this, the trajectory have to be reconstructed, by choosing the correct combination of points in each event to be associated to a track, and fitting them with an appropriate curve in three-dimensional space. The recognition of tracks is done with a method based on the Hough transform, while the fitting is performed by integrating the relativistic equations of motion of the charged particles in the magnetic field. In order to correctly relate the spatial information of the different silicon sensors in a common frame of reference, their mutual positions have to be known. Due to the very high resolution in impact-point reconstruction, an elaborate alignment procedure is needed to find the true configuration of the detectors. The algorithm that has been developed has been applied to test-beam data, and in this way the misalignment corrections for each of the six *towers* which form the spec-

trometer have been calculated. Tracks of cosmic-ray events gathered at ground level have been used as input for a further step of the alignment procedure, which allows to determine the relative positions of the *towers* and the whole-tracker configuration. By means of the correct alignment parameters, the all-particle deflection distribution can be obtained. This information has been combined with an analysis in which the discrimination capabilities of the calorimeter are used to reject electrons, positrons and protons from the muon sample. The muon charge ratio at ground level in the rigidity range $0.3 \div 200$ GV/$c$ has been calculated, and it results to be consistent with previous experimental data of BESS and CAPRICE experiments, and with a computation of the world average ratio: no systematic effect on deflection measurement can be inferred, and this confirms the correctness of the alignment procedure.

A next step of the work on ground-data acquired by PAMELA will be the determination of the detection efficiencies of the instrument and of the selection efficiencies of the analysis procedure, which will allow to calculate the absolute flux of muons at ground level. The satellite which contains the detector is ready to be integrated on the rocket which is going to put it into orbit around the Earth. The alignment procedure which has been developed will be also used to determine the correction parameters for the analysis of cosmic-ray data that will be acquired by the detector during its mission.

# Bibliography


[1] V. F. Hess, Physik. Zeitschr. **12**, 998 (1911).

[2] V. F. Hess, Physik. Zeitschr. **13**, 1084 (1912).

[3] V. F. Hess, Physik. Zeitschr. **14**, 610 (1913).

[4] C. D. Anderson, Phys. Rev. **43**, 491 (1933).

[5] P. A. M. Dirac, Proc. Roy. Soc. **A 117**, 610 (1928).

[6] S. H. Neddermeyer and C. D. Anderson, Phys. Rev. **51**, 884 (1937).

[7] C. M. G. Lattes, H. Muirhead, G. P. S. Occhialini, and C. F. Powell, Nature **159**, 694 (1947).

[8] H. Yukawa, Proc. Phys.-Math. Soc. Japan **17**, 48 (1935).

[9] S. Eidelman et al., Phys. Lett. **B 592**, 1 (2004).

[10] R. A. Millikan and G. H. Cameron, Phys. Rev. **28**, 851 (1926).

[11] M. S. Longair, *High energy astrophysics*, Cambridge University Press, 1981.

[12] J. A. Simpson, Ann. Rev. Nucl. Part. Sci. **33**, 323 (1983).

[13] T. K. Gaisser, *Cosmic rays and particle physics*, Cambridge University Press, 1990.

[14] A. D. Sakharov, JETP Lett. **5**, 24 (1967).

[15] A. Molnar and M. Simon, in *Proceedings XXVII ICRC, Hamburg*, page 1877, 2001.

[16] R. L. Golden et al., Phys. Rev. Lett. **43**, 1196 (1979).

[17] R. L. Golden, B. G. Mauger, S. Nunn and S. Horan, Astroph. Lett. **24**, 75 (1984).

[18] A. Buffington et al., Astroph. Jour. **248**, 1179 (1981).

[19] E. A. Bogomolov et al., in *Proceedings XVI ICRC, Kyoto*, volume 1, page 330, 1979.

[20] E. A. Bogomolov et al., in *Proceedings XX ICRC, Moscow*, volume 2, page 72, 1987.

[21] E. A. Bogomolov et al., in *Proceedings XXI ICRC, Adelaide*, volume 3, page 288, 1990.

[22] E. A. Bogomolov et al., Proc. Rus. Ac. Sc. (phys. ser.) **67**, 447 (2003).

[23] M. H. Salamon et al., Astroph. Jour. **349**, 78 (1990).

[24] R. E. Streitmatter et al., in *Proceedings XXI ICRC, Adelaide*, volume 3, page 277, 1990.

[25] M. Hof et al., Astroph. Jour. **467**, L33 (1996).

[26] J. Mitchell et al., Phys. Rev. Lett. **76**, 3057 (1996).

[27] A. Moiseev et al., Astroph. Jour. **474**, 479 (1997).

[28] M. Boezio et al., Astroph. Jour. **487**, 415 (1997).

[29] S. Orito et al., Phys. Rev. Lett. **84**, 1078 (2000).

[30] M. Boezio et al., Astroph. Jour. **561**, 787 (2001).

[31] A. S. Beach et al., Phys. Rev. Lett. **87**, 271101 (2001).

[32] Y. Asaoka et al., Phys. Rev. Lett. **88**, 051101 (2002).

[33] I. V. Moskalenko and A. W. Strong, Astroph. Jour. **493**, 694 (1998).

[34] J. L. Fanselow et al., Astroph. Jour. **158**, 771 (1969).

[35] J. K. Daugherty et al., Astroph. Jour. **198**, 493 (1975).

[36] A. Buffington et al., Astroph. Jour. **199**, 699 (1975).

[37] R. L. Golden et al., Astr. and Astroph. **188**, 145 (1987).

[38] D. Müller and K. Tang, Astroph. Jour. **312**, 183 (1987).

[39] R. L. Golden et al., Astroph. Jour. **436**, 769 (1994).

[40] R. L. Golden et al., Astroph. Jour. Lett. **457**, L103 (1996).

[41] J. M. Clem et al., Astroph. Jour. **464**, 507 (1996).

[42] S. W. Barwick et al., Astroph. Jour. Lett. **482**, L191 (1997).

[43] M. Boezio et al., Astroph. Jour. **532**, 653 (2000).

[44] M. Boezio et al., Adv. in Sp. Res. **27**, 669 (2001).

[45] C. Grimani et al., Astr. and Astroph. **392**, 287 (2002).

[46] M. Sasaki et al., Nucl. Phys. **B 113**, 202 (2002).

[47] V. A. Naumov, arXiv:hep-ph/0201310 (2002).

[48] S. Avdeev et al., Acta Astronautica **50/8**, 511 (2002).

[49] L. Narici et al., Adv. Sp. Res. **31**, 135 (2003).

[50] A. Bakaldin et al., Astroph. Jour. **577**, 513 (2002).

[51] O. Adriani et al., Nucl. Instr. and Meth. **A 511**, 72 (2003).

[52] A. Galante, *Studio delle prestazioni dell'esperimento PAMELA nella misura di antiparticelle ad alte energie*, Tesi di Laurea, Università degli Studi di Firenze, 2003.

[53] M. G. Abele, *Structures of permanent magnets*, John Wiley & Sons, 1993.

[54] A. Peisert, Silicon microstrip detector, in *Instrumentation in High Energy Physics*, ed. Fabio Sauli, World Scientific, 1992.

[55] IDEAS, *The VA1*, web page: `http://www.ideas.no`

[56] M. Boezio et al., Nucl. Instr. and Meth. **A 487**, 407 (2002).

[57] G. Osteria et al., Nucl. Instr. and Meth. **A 535**, 152 (2004).

[58] J. Lund, *A study of the PAMELA anticoincidence system*, Licentiat thesis, Kungl Tekniska Högskolan, Stockholm, 2002.

[59] S. Orsi et al., $35^{th}$ COSPAR Scientific Assembly, Paris (2004), to be published in Adv. Sp. Res.

[60] *CERNLIB*, web page: `http://cern.ch/wwwasd/cernlib`

[61] *ROOT*, web page: `http://root.cern.ch`

[62] M. Boscherini et al., Nucl. Instr. and Meth. **A 514**, 112 (2003).

[63] M. Badi, *Algoritmi di compressione per il rivelatore tracciante dello spettrometro PAMELA*, Tesi di Laurea, Università degli Studi di Firenze, 2001.

[64] S. Straulino et al., *Spatial resolution of double-sided silicon microstrip detectors for the PAMELA apparatus*, to be published on *Nucl. Instr. and Meth.* **A**, preprint available online at the web page: `http://arxiv.org/abs/hep-ex/0510012`

[65] R. Turchetta, Nucl. Instr. and Meth. **A 335**, 44 (1993).

[66] S. Straulino, *Simulation of silicon microstrip detectors for a cosmic ray experiment*, PhD thesis, Università di Bologna, 2003.

[67] G. Landi, Nucl. Instr. and Meth. **A 485**, 698 (2002).

[68] G. Landi, Nucl. Instr. and Meth. **A 554**, 226 (2005).

[69] D. Fedele, *Algoritmo di riconoscimento e ricostruzione delle tracce nell'esperimento PAMELA*, Tesi di Laurea, Università degli Studi di Firenze, 2003.

[70] H. Bischof and R. Frühwirth, Nucl. Instr. and Meth. **A 419**, 259 (1998).

[71] National Bureau of Standards, procedure 25.5.20.

[72] R. L. Golden et al., Nucl. Instr. and Meth. **A 306**, 366 (1991).

[73] *GPAMELA*, web page: `http://www.ba.infn.it/~ambriola/gpamela`

[74] F. Giambi, *Calibrazione e allineamento dell'esperimento PAMELA su satellite*, Tesi di Laurea, Università degli Studi di Firenze, 2003.

[75] E. Colavitti, *Misura del rapporto $\mu^+/\mu^-$ dai dati a terra prodotti dall'apparato PAMELA*, Tesi di Laurea, Università di Trieste, 2005.

[76] M. Motoki et al., Astropart. Phys. **19**, 113 (2003).

[77] M. Boezio et al., Phys. Rev. **D 67**, 072003 (2003).

[78] T. Hebbeker and C. Timmermans, Astropart. Phys. **18**, 107 (2002).